PHOTOMETRIC INVESTIGATIONS OF HOT SUBDWARF STARS

Master's Thesis in Physics

submitted for the degree of

Master of Science (M.Sc.)

31.03.2020

by **Jan Friedmann**

(Edited on 08.04.2020: corrections marked in blue)

Dr.-Karl-Remeis Observatory Bamberg
Astronomical Institute of
Friedrich-Alexander-University Erlangen-Nuremberg

Supervisor: Prof. Dr. Ulrich Heber

Contents

List of Figures

Abstract

The Gaia space mission collects during its lifetime data from over a billion stars. The second data release is the basis for approximately 40'000 hot subdwarf candidates collected in a catalog by (Geier et al., 2019). This amount of data opens a new dimension for studying the nature of this type of stars. Subdwarfs are a class of stars in a late stage of evolution and the formation still raises many questions. Even though subdwarfs have been investigated for over 30 years only 924 of 5'613 sources were spectroscopically analysed. Apparently, the methods of spectroscopy are very time costly. However, the reliability on spectroscopically derived atmospheric parameters justifies the usage. In contrast, photometric investigations can be extremely fast with limitations to temperature derivation, reddening and search for binarity. So, the large sample of around 40'000 objects can be characterized with photometric methods very efficiently. Unfortunately, Gaia measures only in three bands (G, G_{BP} and G_{RP}) where the G-band is extremely broad and not proper for the investigation on subdwarfs. The combination with UV to IR bandpasses of other surveys finds a remedy. In particular the GALEX survey for the UV regime, SDSS and SkyMapper for the visual range and 2MASS, UKIDSS and WISE in the infrared region are of major significance. Color-Color diagrams with various combinations of these photometric systems have been tested. The main goal of this work is the characterization of single subdwarfs and binary systems. By interpolating temperatures from the well established SDSS colors (u-g) vs. (g-r) an amount of 2'359 new single hot subdwarf candidates are found. For the binary search a different approach is used, namely a proper selection of color combinations followed by an evaluation of spectral energy distributions (SED). From a small selection of 36 spectroscopically determined single subdwarf B stars roughly 80 % show convincing evidence to be a binary system. Further 14 objects are selected which reside close to the Galactic Disk without being classified in the past. Around 43 % of them show features of a binary system but due to a lack of data a clear characterization is not possible. Further 50 % seem to be binaries containing a subdwarf and a cool main-sequence component.

1 Introduction

To understand the evolutionary state of hot compact stars we first take a look at the Hertzsprung-Russell diagram (HRD). Henry Norris Russell and Ejnar Hertzsprung noticed independantly of each other that there is a correlation beween the spectral type of a star and its absolute visual brightness. With this correlation they found the main-sequence. Nowadays, we know that the physical parameters of a star are its surface temperature and its luminosity. Based on the work of Hertzsprung and Russell this leads to the modern version of a Hertzsprung-Russell diagram (s. Fig. 1). At 1913, where Russell published a paper on the theory of stellar evolution based on Hertzsprungs work, there was almost nothing known about the nature of stars. Even the relation between spectral type and effective temperature was discovered more than a decade later by Cecilia Payne in 1926.

The idea of stellar evolution in the HRD began in 1939 with the identification of energy production in stars by Bethe (1939). The first extensive overview on stellar nucleosynthesis was achieved by Burbidge et al. (1956).

The luminosity L of a star is given by the absolute bolometric magnitude M of star compared to the sun:

$$M = M_{sun} - 2.5 \cdot log_{10}\left(\frac{L}{L_{sun}}\right) \tag{1}$$

If the luminosity and radius of the star are known the effective temperature can be derived by following luminosity-temperature relation:

$$L = 4\pi R^2 \sigma T_{eff}^4 \tag{2}$$

with R as the Radius of the object and σ as the Stefan-Boltzmann-constant. By plotting randomly chosen stars into a HRD they will not be homogeneously distributed but bundled in groups. These groups represent different stages of stellar evolution. As an example, the sun remains at the main sequence and will stay there further 5 billion years until the hydrogen inside the core is depleted. While "climbing" up the red giant branch, helium core burning ignites and results in the so called *helium flash*. At this point heavier elements (from Helium to Carbon and Oxygen) will be produced in the core and the sun moves to the horizontal branch. The horizontal branch is a sequence of reducing mass. Due to the sun's hydrogen shell burning and after exhaustion of Helium in the core enough energy is supplied to wander along the asymptotic giant branch (AGB = phase of shell burning around C/O core) and post-AGB to the white dwarfs. But if a star looses almost its entire envelope (shell mass) before the tip of RGB

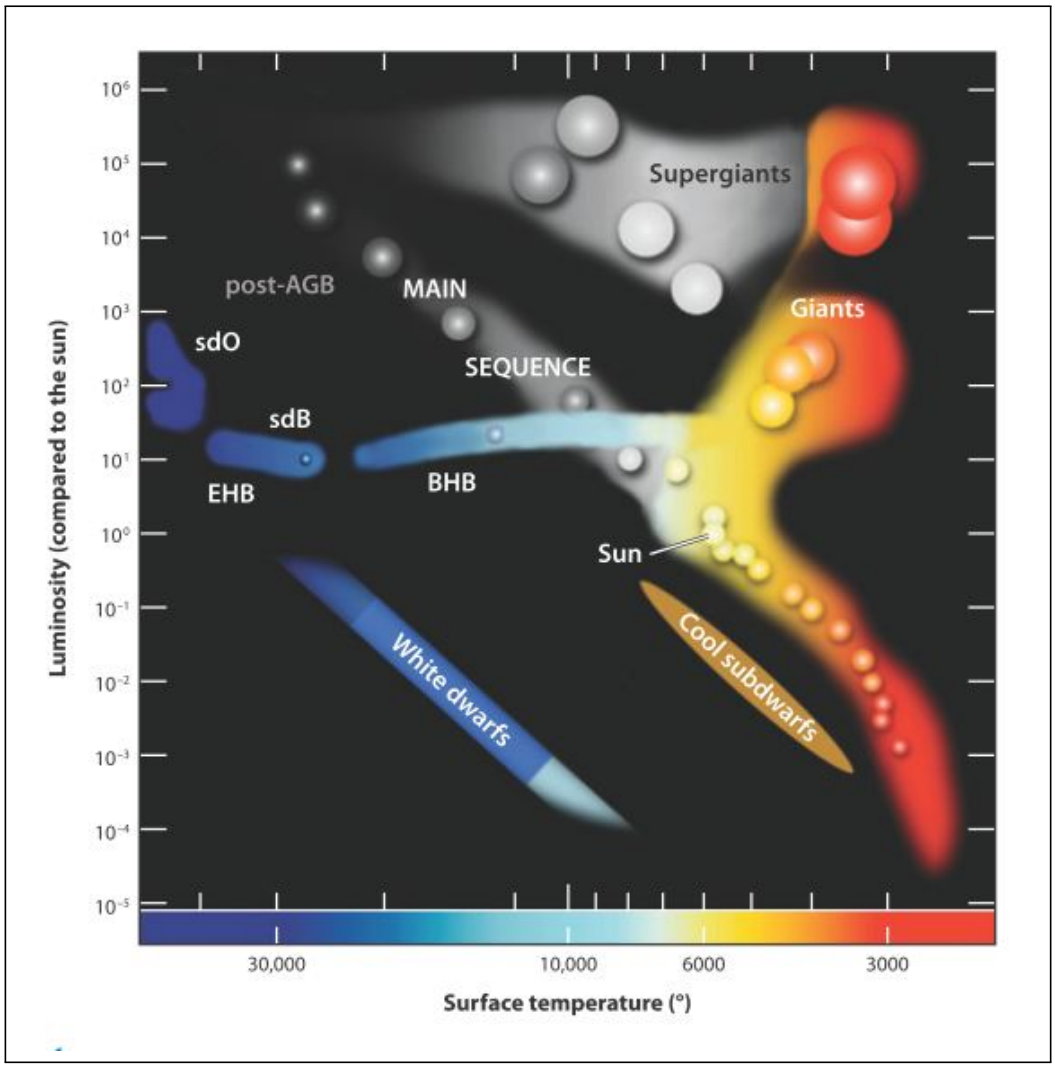

Figure 1: In this Hertzsprung-Russell diagram (HRD) the luminosity is plotted against surface temperature in logarithmic scale. Besides the main sequence other types of stars can be identified which represent different evolutionary states of stars. (Graphic taken from: Heber (2009))

it evolves to the extreme horizontal branch (EHB) to become a subdwarf. Between the horizontal branch and the EHB remains a gap (Newell Gap No. 2) firstly described by Newell in 1973. Up to now there are different plausible explanations as e.g. Soker et al. (2002) which claim that hot horizontal branch stars ($T_{eff} > 20'000K$) begin loosing mass even before the helium flash and have to face a *superwind phase* on the RGB. Hence, the helium burning core can be exposed by a sufficient loss of mass and the star evolves to the subdwarf class before becoming a white dwarf. The ongoing research on hot subdwarfs started over 30 years ago and still the origin is not fully understood yet. With the second data release of the Gaia space mission 40'000 candidates of hot subdwarfs were found, which is a large sample to investigate. Usually, spectroscopic analyses should be done but the effort is huge since the methods are too

time-consuming. Another approach is photometry, which is much more efficient and can be used to characterize a large sample and derive effective temperatures. The next chapter gives an overview on the properties and formation scenarios of hot subdwarfs. Chapter 3 introduces the photometry and photometric systems used or established in different surveys. The spectral energy distribution (SED) is an important tool to identify a binary system and will be described in chapter 4. Both tools will be applied to a sample of hot subdwarf stars (chapter 5) and to a large sample of hot subdwarf candidates (chapter 6). A special focus lies with spectrophotometric binaries. The conclusion builds the final section.

2 Subdwarfs

Subdwarfs are core-helium burning under-luminous stars residing at the hot end of the horizontal branch in the Hertzsprung-Russell diagram (s. sdO and sdB in fig. 1). Therefore those stars are distinct to cool subdwarfs left below the main sequence. Hot subdwarfs are residuals of stars with initial masses between $1-5\,M_{sun}$. Although the formation of hot subdwarfs is not fully understood yet, there are some promising formation scenarios described in the following section.

2.1 Formation scenarios

To understand hot subdwarf formation it is necessary to get an idea how a RGB star is able to loose nearly its entire envelope just before starting core-helium burning. Furthermore, it will be assumed that the driving mechanisms of subdwarf B (sdB) and subdwarf O (sdO) differ because sdBs are mostly found in binary systems whereas sdOs are usually single stars. Common scenarios like *Common-envelope ejection* and *Roche-Lobe Overflow* for subdwarfs in binary systems as well as *white dwarf merger* for single stars will be discussed.

2.1.1 Roche-Potential

The Roche-Potential describes the range around a binary system where surrounding material is still gravitationally bound to each star. Fig. 2 shows the surface of equipotential of the system in two dimensions with three marked spots L1, L2 and L3. On top of that the three dimensional gravitational potential can be seen. L1 to L3 are Lagrangian-Spots on which the attractive forces of both stars cancel each other. Since mass transfer happens over L1 in binary systems, this spot is of special interest. The equipotential surface which belongs to the lowest potential (in this case L1) is called *Roche-lobe*.

2.1.2 Roche-Lobe-Overflow

The Roche-Lobe-Overflow (RLOF) is a stable mass transfer in contrast to *Common-Envelope Ejection (CEE)*. In a binary system consisting of two main sequence stars a RLOF occurs if a mass ratio of $1.2 < \frac{M_1}{M_2} < 1.5$ is given. The more massive companion moves along the red giant branch until its Roche-lobe is filled. As soon as this condition is fulfilled mass transfer via L1 sets in. So, the more massive star does not exceed its

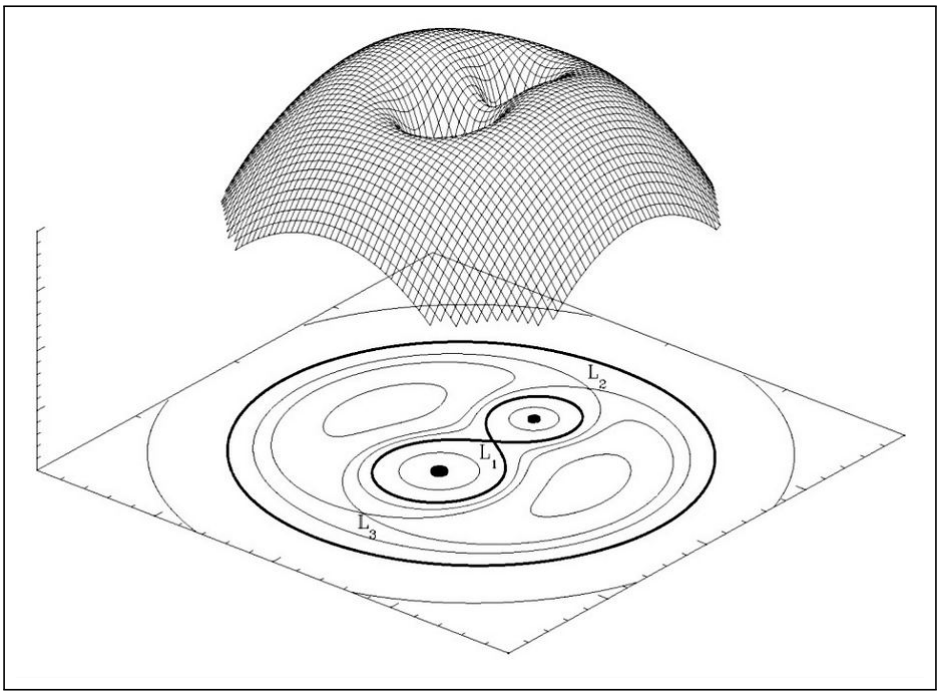

Figure 2: Three dimensional representation of Roche-Potential and its äquipotential. (Figure from: $https://en.wikipedia.org/wiki/Roche_lobe\#/media/File:RochePotential.jpg$, 16.08.2019)

Roche-lobe due to mass accretion of the less massive companion. This process takes place until the red giant lost almost its entire envelope. The former red giant now ignites core-helium burning and finally becomes a hot subdwarf. Mass transfer leads to a widening of the system and in general a hot subdwarf and a cool companion form a binary system with an orbital period of 300 to 1'500 days.

2.1.3 Common-Envelope Ejection

The *Common-Envelope Ejection* sets in under specific conditions of two gravitationally bound stars. According to Han et al. (2002) this happens if the mass ratio exceeds the limit of $q = 1.2..1.5$ mass transfer is so high that the material can not be accreted by the companion and a common envelope around both stars forms. Orbital momentum and energy are transfered to the envelope by friction leading to the ejection of the envelope. The result after this event is a subdwarf B star with companion and an orbital period between 0.1 and 10 days. Fig. 3 shows a summary of above mentioned RLOF+CEE, RLOF and CEE scenarios.

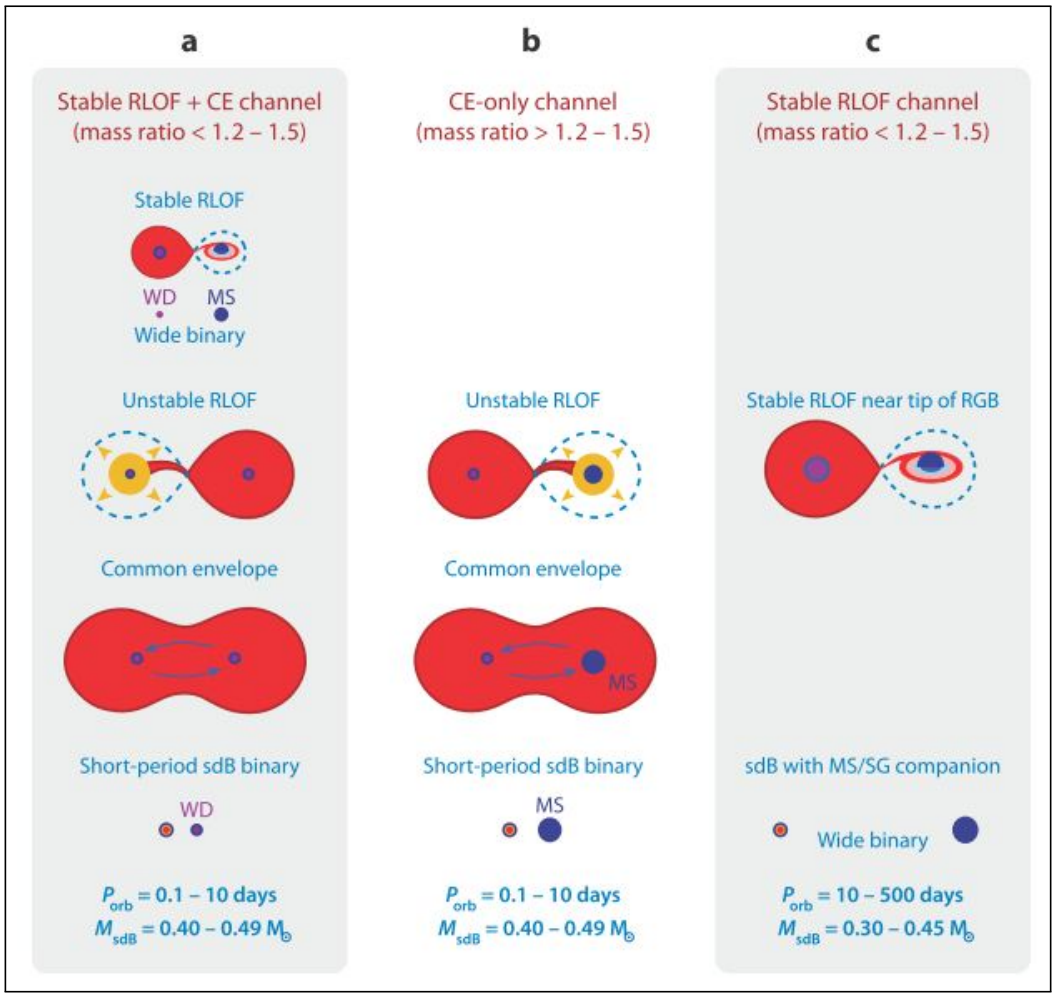

Figure 3: a) A combination of stable RLOF and CEE leads to white dwarf plus companion. If the main sequence stars can not reach the helium flash, a system of sdB and helium white dwarf remains, else a sdB and a C/O white dwarf will form. Typical orbital periods are $P_{orb} = 0.1 - 10[d]$. b) CEE alone leads to a constellation of sdB and main sequence star with periods of $P_{orb} = 0.1 - 10[d]$. c) Stable RLOF alone form a subdwarf plus main sequence or subgiant companion. The orbital periods of such systems are high with $P_{orb} = 10 - 500[d]$, hence the future evolution of both stars will be independant. (Graphic taken from: Heber (2009)

2.1.4 White Dwarf Merger

Another way to form a subdwarf is merging of two helium white dwarfs (*white dwarf merger scenario*). If this binary system is close, then the transfer of energy and angular momentum via gravitational waves is high enough to cause a shrinking of the orbit of both white dwarfs. Below a critical distance the less massive white dwarf overcomes its Roche-limit and a runaway process takes place. The reasons is following mass-radius relation for white dwarfs:

$$R \propto M^{-\frac{1}{3}} \tag{3}$$

As soon as the less massive white dwarf fills its Roche-lobe the Roche lobe overflow (RLOF) sets in and leads to a mass transfer to the heavier WD. Due to the mass loss of the lighter WD its Roche-lobe becomes bigger and more mass will be transferred. This procedure keeps continuing until the less massive white dwarf gets disrupted. The remaining material forms an accretion disk around the heavier companion. If enough mass has been accreted helium core burning occurs and a revival of a WD to a subdwarf takes place. Thus, this scenario provides an explanation for single, unbounded subdwarfs as well as the formation of helium rich subdwarf O stars.

3 Photometry

3.1 Magnitudes

The *apparent magnitude m* is a historically defined value to scale the brightness of star seen by the naked eye. The apparent magnitude is related to the flux via:

$$m = -2.5\, log_{10}(F) + K \tag{4}$$

with F as the flux and K as a constant. K is chosen such that *Vega* has an apparent magnitude $m \approx 0\,[mag]$. The unit $[mag]$ is based on a logarithmic scale and so a difference of 5 magnitudes corresponds to a difference in brightness of a factor of 100. More specific, the ratio of brightness is given by $100^{\Delta m/5}$, where Δm denotes the difference of two magnitudes. The smaller magnitude belongs to the brighter object due to the definition:

$$m_1 - m_2 = -2.5\, log_{10}\left(\frac{F_1}{F_2}\right) \tag{5}$$

where m_1 and m_2 are apparent magnitudes of two stars and F_1 and F_2 the corresponding fluxes. The sun has an apparent magnitude of m = -26.83, whereas the faintest objects are roughly at m $\approx$ 30. (Carroll & Ostlie, 2007) Since the magnitudes correspond to a logarithmic scale the sun appears to be 10^{23} times brighter than the faintest objects in the sky. The apparent magnitude is usually measured in some filters with a specific bandwidth. By integrating the flux over the whole electromagnetic spectrum we receive the apparent bolometric magnitude. The difference between the apparent bolometric magnitude and the apparent magnitude is called bolometric correction. A more comparable value was introduced later with the *absolute magnitude M* where the stars brightness at a distance of 10 pc is calculated. The distance modulus gives the relation between the apparent and absolute magnitude:

$$m - M = 5\, log_{10}\left(\frac{d}{10pc}\right) \tag{6}$$

with d as the actual distance to the star. Furthermore, the absolute magnitude M is related to the luminosity L of a star by:

$$M = M_{sun} - 2.5\, log_{10}\left(\frac{L}{L_{sun}}\right) \tag{7}$$

with M_{sun} as the absolute magnitude of the sun and L_{sun} as the luminosity of the sun. But equation (7) is only valid for the absolute bolometric magnitude which is the

absolute magnitude integrated over the whole electromagnetic spectrum. We can not measure the absolute bolometric magnitude directly but the flux in different filters and make a bolometric correction which can be calculated with synthetic spectra.

3.2 Color Index and Color-Color diagram

The brightness (i.e. the radiant flux) is measured in different wavelength regimes (filters) and can be compared. The so called *Color index* is the difference between two magnitudes in different filters. This value is then independent of the stars distance as equation (6) shows and can be used to derive temperatures. If one imagines arbitrary narrow filters f_1 at 400 nm and f_2 at 700 nm (which marks the range where the spectrum is visible for the naked eye) the Color index $c_1 = f_1 - f_2$ give information about the temperature of the object. For a 7'000 K source the color index c_1 would be more negative as for the sun (5'777 K) and for the 4'000 K source the color index would be even positive (s. Fig. 4).

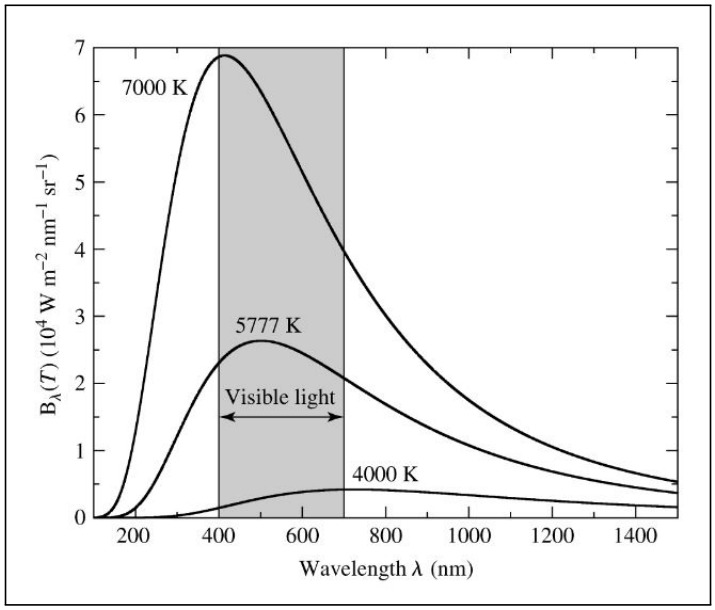

Figure 4: Blackbody spectrum of three different source with 4'000 K, 5'777 K (sun) and 7'000 K. The grey area displays the electromagnetic range visible for the human eye from around 400 nm up to 700 nm. (Graphic taken from: Carroll & Ostlie (2007))

In the UBV-system (ultraviolet, blue, visual) filters are set such that the center frequency of the detector lies in the ultraviolet ($\approx$ 365 nm), in the blue ($\approx$ 440 nm) and visual ($\approx$ 550 nm) range each having an effective bandwidth. The color indices can be then build like U-B, B-V or U-V which means the apparent magnitudes in the blue wavelength range is subtracted from the ultraviolet magnitude and so on. Hotter stars

(e.g. $T_{eff} \approx$ 50'000 K) will have a lower value for U-B than cooler stars (e.g. $T_{eff} \approx$ 5'000 K) because the emission in the ultraviolet is much higher. By plotting two color indexes on x- and y-axis we create a *Color-Color diagram*.

If stars were blackbodies, we would see a straight line in these diagrams formed by all spectral classes. Since this is not the case one can see deviations from a blackbody depending on the spectral class (i.e. temperature) and the wavelength. So, main-sequence O- and B-stars show a slight deviation because hydrogen is almost fully ionized and hence the Balmer jump vanishes. Main-sequence A-stars in contrast show a relative big Balmer jump caused by neutral hydrogen leading to a huge deviation from a blackbody, respectively. For early-type main-sequence stars the difference between blackbody and a star can be explained by the H^- opacity (s. Fig. 5).

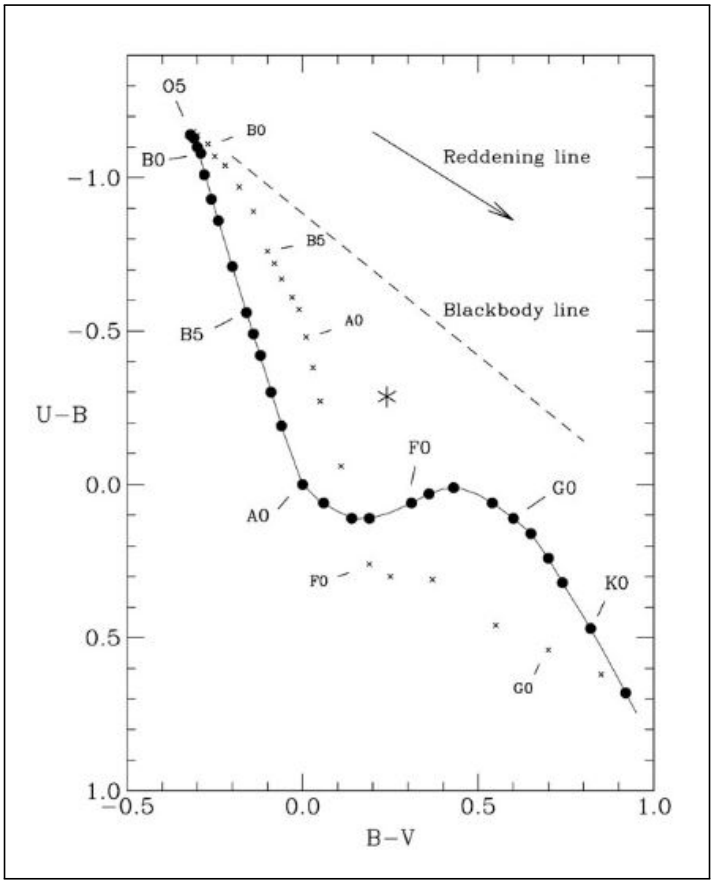

Figure 5: Color-Color diagram with Color indexes (U-B) and (B-V) in Johnson photometric system. The dashed line represents a blackbody whereas the filled dots are main-sequence stars and the crosses indicate supergiants. The reddening vector gives the direction in the diagram to which an object is shifted if influenced by reddening effects. (Graphic taken from: Milone & Sterken (2011))

In this way, depending on the purpose broader or narrower filters are used to gather information about the stars or systems properties. That's why some surveys use pre-

defined photometric systems, like the Strömgren system, whereas other ones define a system by themselves, like SDSS does. In the following photometric systems used in the analysis of this work are described.

3.3 Photometric systems

3.3.1 Ultraviolet

Ultraviolet fluxes are taken from the Galaxy Evolution Explorer (GALEX) which is a NASA Explorer Mission launched in Spring 2003 to reside in a 690 km circular orbit. Besides a deep imaging survey of 100 square degrees and a medium imaging survey of 1000 square degrees, an all-sky imaging survey is included. The main goal of GALEX is the study of UV properties of stars with a redshift range $0 < z < 2$. The two bands (s. Fig. 6) near-UV (1750 - 2800 $\mathring{A}$) and far-UV (1350 - 1750 $\mathring{A}$) with 4.5 - 6 arcsecond resolution (Martin & GALEX Team, 2005) are used to cover the UV range of photometry including the ultraviolet absorption bump at $\approx$ 2200 $\mathring{A}$.

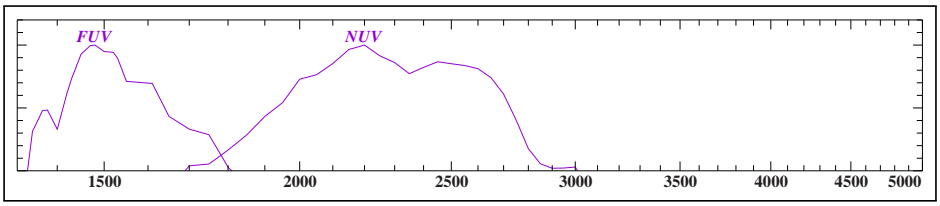

Figure 6: Relative spectral response function of GALEX FUV and NUV passbands. The x-axis is given in [$\mathring{A}$]. The y-axis is in arbitrary units.

3.3.2 Visual

In the visual range of the electromagnetic spectrum photometric data is gathered in narrow bands as well as wide bands (s. Fig. 7). Narrow bands give information about specific features within a small (narrow) wavelength range such as the Balmer discontinuity, Paschen continuum or line blanketing due to its sensitivity to surface gravity, stellar temperature or metallicity. But to receive reliable data high precision photometry has to be done with errors less than 0.01 mag. Broadband filters in contrast cover a wider region, can provide e.g. temperatures with 6 times greater sensitivity in Johnson (V-K) band than Strömgren (b-y) and fainter objects can be reached in a given time (Bessell, 2005). But certain features (like the Balmer jump) can not be investigated. So, it depends on the purpose if narrow bands (like Strömgren filters), broad bands (like Johnson passbands) or a combination of them should be used. In the following

the passbands for each photometric system are given with the effective wavelength λ_{eff} and the widths of the corresponding bands. The effective wavelength is defined as:

$$\lambda_{eff} = \frac{\int \cdot\lambda \cdot f_\lambda R(\lambda) d\lambda}{\int \cdot f_\lambda R(\lambda) d\lambda} \tag{8}$$

with f_λ as the source flux and $R(\lambda)$ as the response function of the filter. Therefore, the effective wavelength provides information about which photons have the most influence on a particular measurement. But λ_{eff} is not measurable directly since it depends on the flux distribution f_λ which is dependant on the temperature.

Johnson-Cousins The Johnson photometric system was introduced by Johnson & Morgan (1953) containing three bands in the ultraviolet (U-band), blue (B-band) and visual (V-band) wavelength range. To obtain more information like about the Balmer discontinuity of late-type stars two more bands were defined. The colors B-V and U-B are chosen to be zero for mainsequence stars of class A0 in the Morgan-Keenan system. Bingham & Cousins (1974) and later Cousins (1978) extended and improved the UBV-system by adding two filters in the red (R-band) and infrared (I-band). Nowadays, the resulted photometric system is known as Johnson-Cousins system with wide UBVRI-bands. The wavelengths and widths are given in table 1.

Band	$\lambda_{eff}[\mathring{A}]$	Width $[\mathring{A}]$
U	3663	650
B	4361	890
V	5448	840
R	6407	1580
I	7980	1540

Table 1: UBVRI filter in Johnson-Cousins. Commonly used colors are: $(U-B)$, $(B-V)$ and $(R-I)$.

Strömgren The Strömgren photometric system provides narrow band magnitudes and was historically introduced as a method of spectral classification of F stars. The strength of the H_β-line was measured in three filters (Strömgren, 1956) at 4700 $\mathring{A}$, 5000 $\mathring{A}$ and 4861 $\mathring{A}$ by setting an index as follows:

$$l = 2.5\,\{\frac{1}{2}\,[log\ I(4700) + log\ I(5000)] - log\ I(4861)\} + const. \tag{9}$$

with l as the index and $I(\lambda)$ as the intensity for a specific wavelength. This index was used to investigate metallic line stars and was later adjusted to the metallicity index $m_1 = (v-b)-(b-y)$. Moreover, a classification index was introduced to evaluate the Balmer discontinuity in three further filters:

$$c = 2.5\,\{2\,log\,I(4030) - log\,I(3559) - log\,I(4500)\} + const. \tag{10}$$

with c (or nowadays $c_1 = (u-v)-(v-b)$) as the Balmer discontinuity index. Later, the Strömgren system was optimized for B, A and F stars and the bands are now defined as listed in table 2.

Band	$\lambda_{eff}[\mathring{A}]$	Width $[\mathring{A}]$
u	3520	314
v	4100	170
b	4688	185
y	5480	226
β_{wide}	4890	150
β_{narrow}	4860	30

Table 2: uvby filter in Strömgren. Commonly used colors are: $(u-b)$, $m_1 = (v-b)-(b-y)$, $c_1 = (u-v)-(v-b)$ and $(b-y)$.

SDSS The Sloan digital sky survey (SDSS) uses a wide-band CCD system in the range of 3000 to 11000 $\mathring{A}$. So, the five passbands spread from the atmospheric ultraviolet cutoff up to the sensitivity limit of silicon CCDs. The corresponding wavelengths are listed in table 3. Compared to Strömgren or SkyMapper, this system uses significantly wider bandpasses which can cause flat-fielding problems with older back-illuminated CCDs (Fukugita et al., 1996). Nevertheless, SDSS provides very reliable data, hence it is widely used among astronomers.

Band	$\lambda_{eff}[\mathring{A}]$	Width $[\mathring{A}]$
u	3500	600
g	4800	1400
r	6250	1400
i	7700	1500
z	9100	1200

Table 3: ugriz filter in SDSS. Commonly used colors are: $(u-g)$, $(g-r)$, $(r-i)$.

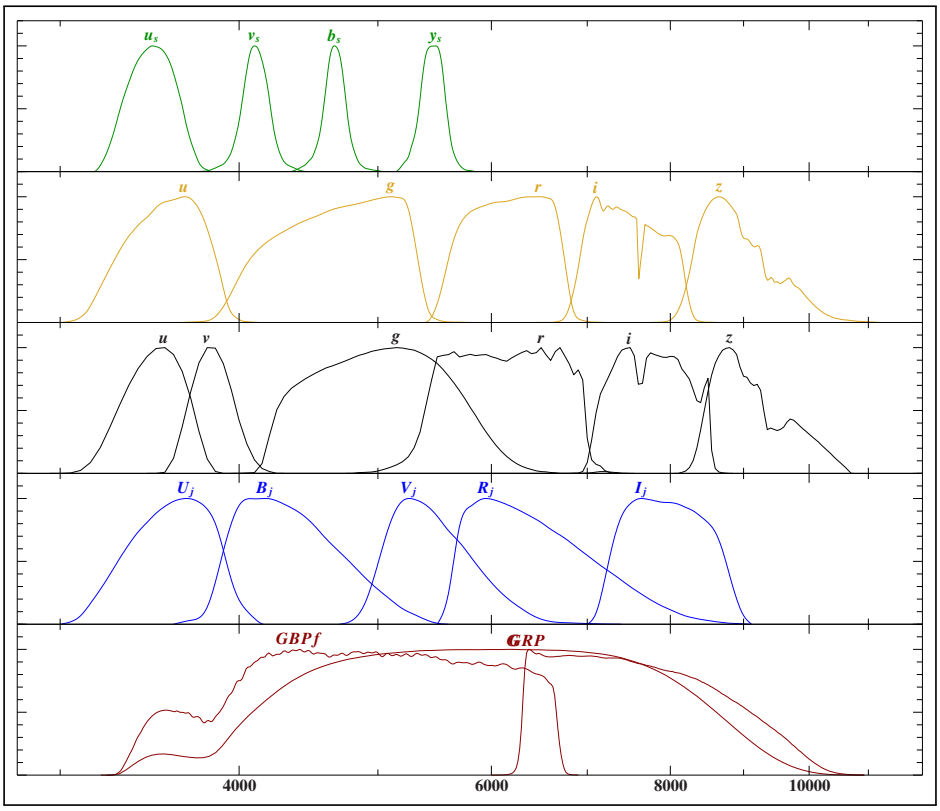

Figure 7: Relative spectral response function of top to bottom (green): Strömgren $uvby$, (yellow): SDSS $ugriz$, (black): SkyMapper $uvgriz$, (blue): Johnson $UBVRI$ and (red): Gaia $G'G'_{BP}G_{RP}$ passbands. The x-axis is given in [$\AA$]. The y-axis is in arbitrary units.

SkyMapper The SkyMapper survey covers 2π steradians of the southern hemisphere and was launched in late 2007. The wide-field survey will run five years with the main goal of performing six colour and multi-epoch photometry of the southern sky. SkyMapper wants to bring light into darkness in the fields of the distribution of objects beyond Neptune, the history of the youngest stars in the solar neighbourhood, high redshift quasi stellar objects (QSO) and many more. The filters were chosen such that the stellar parameters: effective temperature, surface gravity and metallicity can be best discriminated. (Keller et al., 2007) The modified Cassegrain telescope operates in wavelength range of 340 to 1000 nm and provides Strömgren-like (narrow band) and SDSS-like (broad band) filters (s. tab. 4).

Gaia The *Gaia* Mission started collecting scientific data in July 2014 and nominally lasts for 60 month. After 22 month the second intermediate Gaia data release (Gaia DR2) took place and contained broad-band color information for over a billion stars. This multi-band all-sky survey provides colors in G,G_{BP} and G_{RP} bands (s. Fig. Fig. 7) which correspond to a wavelength range between 330 - 1050 nm ($G = 330 - 1050$

Band	$\lambda_{eff}[\AA]$	Width $[\AA]$
u	3250	430
v	3670	310
g	4170	1460
r	5550	1460
i	7030	1400
z	8520	1170

Table 4: uvgriz filter in SkyMapper

nm, $G_{BP} = 330 - 680$ nm and $G_{RP} = 630 - 1050$ nm). For all sources G-band fluxes are reported, whereas just for 80 % mean values of G_{BP} and G_{RP} fluxes are provided. (Collaboration et al., 2018) The apparent brightness of the stars in the survey spans from $13 \leq G \leq 21$ where the bright end of photometric uncertainties is dominated by calibration effects (Evans et al., 2018) and the data for faint stars $G \geq 19$ show strong systematic effects which leads to errors for mean G_{BP} and G_{RP} fluxes at $G = 20$ mag of ≈ 0.2 mag. The amount of objects in the Gaia database will exceed a billion stars and so this survey is the most important source for investigating large samples of stars.

3.3.3 Infrared

The infrared region is covered by different surveys (s. Fig. 8) and therefore a variety of sources are available to gather data.

2MASS The two micron all sky survey (2MASS) has been operated between mid 1997 and early 2001 and collected infrared data covering 99.998 % of the celestial sphere (Skrutskie et al., 2006). Since 2MASS is a ground-based near-infrared survey the choices of passbands were constrained by atmospheric transmission and ambient thermal background. Three different wavelength bands are defined namely J band (1.2 μm), H band (1.6 μm) and K-band (2.16 μm). These bands are comparable with Johnson (1962) J, H and K bands with an adjustment on the K-band such as thermal background and airglow is reduced.

UKIDSS Many times deeper than 2MASS but with lower celestial coverage is the UKIRT Infrared Deep Sky Suvery (UKIDSS). This seven-year survey started in 2005 May and the primary goal to provide an infrared sky catalog as a fundamental resource with high significance (Lawrence et al., 2007). The wavelength range is 0.83 up to

2.37 μm in five filters namely ZYJHK. The corresponding wavelengths are listed in table 5.

Band	$\lambda_{eff}[\mu m]$	Width $[\mu m]$
Z	0.8817	0.093
Y	1.0305	0.102
J	1.2483	0.159
H	1.6313	0.292
K	2.2010	0.351

Table 5: ZYJHK filter in UKIDSS

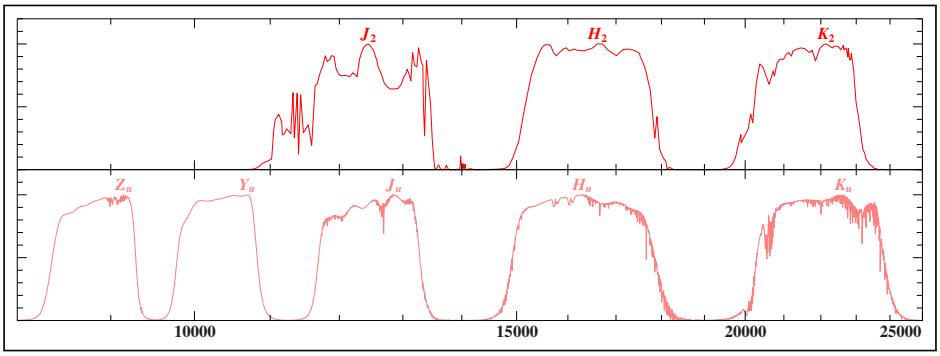

Figure 8: Relative spectral response function for (top): 2MASS JHK and (bottom): UKIDSS $ZYJHK$ passbands. The x-axis is given in [$\AA$]. The y-axis is in arbitrary units.

WISE The wide-field infrared survey explorer (WISE) is mapping the whole sky and launched in December 2009 as a space mission. In comparison to former surveys in the wavelength range between 3.4 and 22 μm (mid-IR), like the infrared astronomical satellite (IRAS), the sensitivity i.e. in the 12 μm band of WISE is ≈100 times higher (Wright et al., 2010). The wavelengths of the four WISE passbands (s. Fig. 9) are given in table 6. Also, WISE will go a magnitude deeper in W1-band as e.g. 2MASS in its K-band. Therefore, WISE provides high sensitivity in the mid-infrared region.

Band	$\lambda_{eff}[\mu m]$	Width $[arcsec]$
W1	3.4	6.1
W2	4.6	6.4
W3	12	6.5
W4	22	12.0

Table 6: W1-W4 filter in WISE

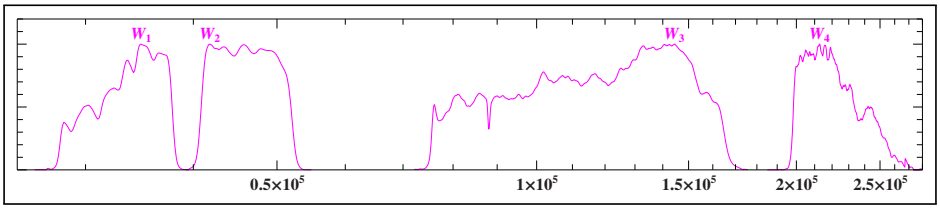

Figure 9: Relative spectral response function for WISE $W1 - W4$ passbands. The x-axis is given in [$\AA$]. The y-axis is in arbitrary units.

4 Spectral energy distribution

The spectral energy distribution (SED) offers the possibility to identify a late-type companion in a binary system containing a hot subdwarf due to an expected infrared excess. However, the assumption of a cool companion should then be supported by further signs since the excess can also be caused e.g. by free-free emission from a stellar wind or hot dust surrounding the star (Thejll et al., 1995). Later synthetic and constructed observational SEDs will be compared in the analysis section to see if there is greater flux in the infrared region. Figure 10 shows the contribution of a subdwarf and a main-sequence star to the SED in a binary system. As one can see in this figure, the subdwarf dominates the flux in the UV-region whereas main-sequence companions henpecks the IR-region.

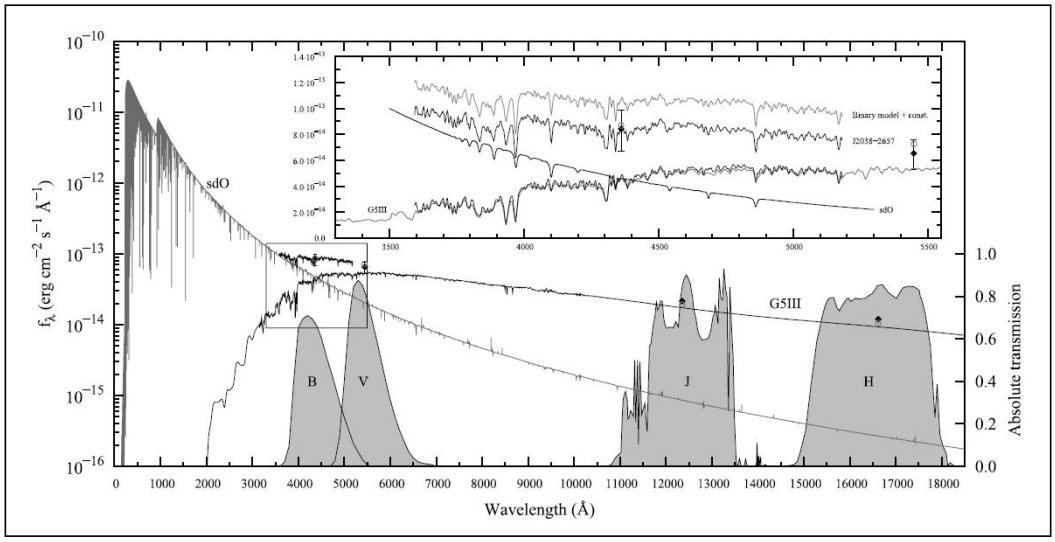

Figure 10: The spectral energy distribution consists of two stars. The subdwarf (grey) and the G5III main-sequence star (black). The region around the intersection of both is zoomed into the mini-image (top-right). The filter B, V, J and H show the contribution of both stars to the synthetic photometry. (Graphic taken from: Németh et al. (2012)

To model a magnitude mag_x has to be calculated for a specific bandpass x:

$$mag_x = -2.5log\left(\frac{\int_0^\infty r_x(\lambda)f(\lambda)\lambda d\lambda}{\int_0^\infty r_x(\lambda)f^{ref}(\lambda)\lambda d\lambda}\right) + mag_x^{ref} \tag{11}$$

with $f(\lambda)$ as the stellar flux on earth, $f^{ref}(\lambda)$ the flux of a reference star, $r_x(\lambda)$ as the transmission function of the filter and mag_x as the magnitude to set the zero point of the magnitude. $f(\lambda)$ can be expressed by the angular diameter of the star Θ and the

modelled flux at the stellar surface $F(\lambda)$:

$$f(\lambda) = \frac{\Theta^2 F(\lambda)}{4} \tag{12}$$

Furthermore, interstellar extinction has to be considered by adding a reddening factor $10^{-0.4A(\lambda)}$. The extinction at a specific wavelength $A(\lambda)$ is taken from Fitzpatrick (1998) who found the relation $R_V = A(V)/E(B-V) = 3.1$ for stars significantly above the Galactic plane. To put it all together we end up with: [1]

$$mag_x = -2.5log\left(\frac{\Theta^2 \int_0^\infty r_x(\lambda) 10^{-0.4A(\lambda)} F(\lambda)\lambda d\lambda}{4\int_0^\infty r_x(\lambda) f^{ref}(\lambda)\lambda d\lambda}\right) + mag_x^{ref} \tag{13}$$

In this way we construct synthetic SEDs to be compared to the observed distribution of magnitudes in different photometric systems and wavelength regimes (UV to mid-IR). Dr. Andreas Irrgang (Dr. Karl Remeis-Observatory) created an ISIS-program to fit SEDs by using different model grids. For identifying a late-type companion a non-LTE stellar atmosphere computer code called PHOENIX (Hauschildt & Baron, 1999) was used. The model taken for subdwarf B stars is the ATLAS12 code which is a computer program for calculationg model stellar atmospheres originally designed by Kurucz (1970). Photometric data is collected by querying databases of a variety of surveys and catalogues via SQL/ADQL. With the right ascension, declination and a search radius data is collected in tables. The search radius is restricted in all queries to 0.001 degree or 3.6 arcsec, respectively. The catalogs implemented in Dr. Irrgangs scripts are:

- $II/335/galex_ais$: Revised catalog of GALEX UV sources (Bianchi et al., 2017)
- $I/311/hip2$: Hipparcos, the New Reduction (van Leeuwen, 2007)
- $I/259/tyc2$: The Tycho-2 Catalogue (Hog et al., 2000)
- $I/345/gaia2$: Gaia DR2 (Collaboration et al., 2018)
- $II/168/ubvmeans$: Homogeneous Means in the UBV System ("`https://vizier.u-strasbg.fr/viz-bin/VizieR-2`)
- $II/237/colors$: Stellar Photometry in Johnson's 11-color system (Ducati, 2002)
- $II/7A/catalog$: UBVRIJKLMNH Photoelectric Catalogue (Morel & Magnenat, 1978)

[1] (Heber et al., 2017)

- $J/AJ/133/2502/phot$: UBVRI Standard Stars (Landolt, 2007)
- $J/ApJS/123/639/ubv$: UBV photometry of metal-weak candidates (Norris et al., 1999)
- $II/169/main$: Observations in the Geneva Photometric System 4 (Rufener, 1999)
- $II/215/catalog$: uvby-beta Catalogue (Hauck & Mermilliod, 1997)
- $J/A+A/580/A23/catalog$: Stroemgren-Crawford uvbyβ photometry catalog (Paunzen, 2015)
- $J/AJ/119/241/table2$: Catalog of MCT objects in the south Galactic cap region (Lamontagne et al., 2000)
- $J/MNRAS/287/867/table1$: Edinburgh-Cape Blue Object Survey. Zone 1. (Kilkenny et al., 1997)
- $J/MNRAS/431/240/table3$: Hot objects in zone 2 of the Edinburgh-Cape survey (O'Donoghue et al., 2013)
- $J/MNRAS/453/1879/table2$: Hot objects in Zone 3 of the EC survey (Kilkenny et al., 2015)
- $J/MNRAS/453/1879/table3$: Cool objects in Zone 3 of the EC survey (Kilkenny et al., 2015)
- $J/MNRAS/459/4343/table3$:Hot objects in Zones 4-6 of the EC survey (Kilkenny et al., 2016)
- $II/262/batc$: BATC Data Release One - BATC DR1 ("`https://vizier.u-strasbg.fr/viz-bin/VizieR-2`)
- $V/147/sdss12$: The SDSS Photometric Catalogue, Release 12 (Alam et al., 2015)
- $II/349/ps1$: The Pan-STARRS release 1 (PS1) Survey - DR1 (Chambers et al., 2016)
- $II/347/kids_d r3$: KiDS-ESO-DR3 multi-band source catalog (de Jong et al., 2017)
- $II/350/vstatlas$: VLT Survey Telescope ATLAS (Shanks et al., 2015)
- $II/336/apass9$: AAVSO Photometric All Sky Survey (APASS) DR9 (Henden et al., 2015)

- $II/246/out$: 2MASS All-Sky Catalog of Point Sources (Cutri et al., 2003)
- $II/316/gps6$: UKIDSS-DR6 Galactic Plane Survey (Lucas et al., 2008)
- $II/319/las9$: UKIDSS-DR9 Large Area Survey (Lawrence et al., 2007)
- $II/319/gcs9$: UKIDSS-DR9 Galactic Clusters Survey (Lawrence et al., 2007)
- $II/319/dxs9$: UKIDSS-DR9 Deep Extragalactic Survey (Lawrence et al., 2007)
- $II/328/allwise$: AllWISE Data Release (Cutri & et al., 2014)
- $Skymapper\_DR1.1$ ("`http://skymapper.anu.edu.au/`")
- VHS_DR6: VISTA Hemisphere Survey DR6 ("`http://horus.roe.ac.uk/vsa/index.html`")
- $VIKING\_DR4$: VISTA Kilo-Degree Infrared Galaxy Survey DR4 ("`http://horus.roe.ac.uk/vsa/index.html`")
- VMC_DR4: VISTA Magellanic Cloud Survey DR4 ("`http://horus.roe.ac.uk/vsa/index.html`")
- VVV_DR4: VISTA Variables in Via Lactea DR4 ("`http://horus.roe.ac.uk/vsa/index.html`")
- $VIDEO\_DR5$: VISTA Deep Extragalactic Observations DR5 ("`http://horus.roe.ac.uk/vsa/index.html`")
- $VI/110/inescat$: Final Merged Log of IUE Observations ("`https://vizier.u-strasbg.fr/viz-bin/VizieR-2`)

The bunch of catalogs covers the wavelength range from far-UV (GALEX) up to mid-infrared (WISE).

5 Investigation

The Gaia space mission collects photometric data from over a billion objects in three bands (G, G_{BP} and G_{RP}). This is a huge database opening the possibility to study large sets of stars. But it is also a very challenging task as spectroscopic analyses are time-consuming and the enormous amount of data can not be handled effectively. So, only roughly a fifth of the 5'613 objects in the first catalog of Geier et al. (2017) have atmospheric parameter provided. In contrast, photometry offers the opportunity to characterize stars in a much faster way even though it is mainly limited to effective temperature, reddening and binarity. In the following the different possibilities to characterize stars by just using photometry will be pointed out.

5.1 Reddening vector

By assuming an interstellar extinction parameter of $R_V = 3.1$ for all measurements, the reddening vector is constructed by comparing the unreddened magnitude and the reddened magnitude. The color excess $E_{B-V} = (B-V)_{obs} - (B-V)_{intr}$ is set to 0.1 in each diagram. This value was chosen to restrict the length of the reddening vector in the diagrams for a better overall visibility. Since no Gaia parallaxes or otherwise determined distances are used the reddening vector is just an indication for the direction where the length can be arbitrarily chosen. All reddening vectors are calculated for an effective temperature of $T_{eff} = 25'000$ K and gravity of $log(g) = 5.4$. Those parameters were arbitrarily chosen since reddening vectors slope only negligibly varies for every grid location (s. Figures 11 and 12).

For further analyses the reddening vector is used to derive temperatures by linear interpolation. A reddening free index is defined as $Q = y - m * x$ with y as the color on y-axis, x as the color on x-axis and m as the slope of the reddening vector.

5.2 Temperature derivation

If a color-color diagram is plotted (s. Fig. 13) one can see the temperature gradient to bluer colors with higher temperatures. Furthermore, an sdB model grid between $15'000 < T_{eff} < 55'000$ K and $4.6 < log(g) < 6.2$ is plotted. By considering the reddening vector most of the stars are represented well by the model since a movement of the objects along the reddening vector hits in most cases at least one T_{eff} - $log(g)$ track. These stars get a reddening free index Q and will be linearly interpolated to

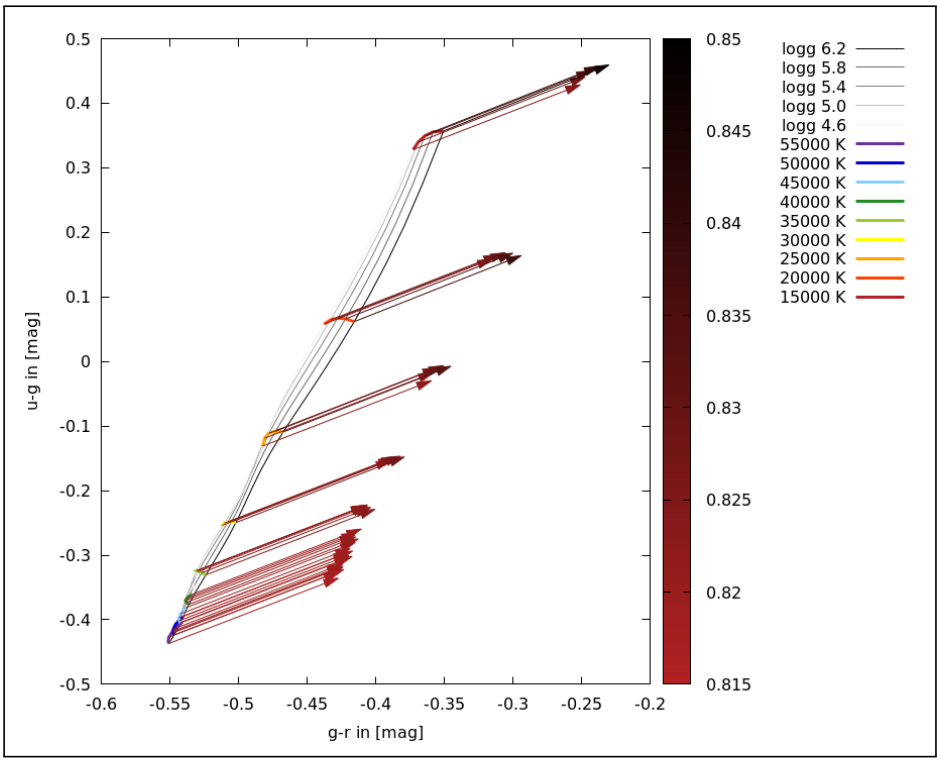

Figure 11: (u-g) vs. (g-r) in SDSS system: For every location in the grid ($15'000 < T_{eff} < 55'000$ K and $4.6 < log(g) < 6.2$ dex) the reddening vector is shown with the properties $E(B-V) = 0.1$ and $R_V = 3.1$. The color palette indicates the slope of the vectors. Only slight changes are observed.

receive a temperature to compare with spectroscopically determined ones.

The result from the one-dimensional linear interpolation fit quite well to temperatures received from spectroscopy for 25'000 K to 35'000 K. (s. Fig. 14). Since this color combination is not very sensitive to log(g) the distribution is quite equal for any value of log(g) (s. Fig. 15). For lower temperatures an underestimation compared to spectroscopically determined temperatures occur whereas for higher temperatures (over 35'000 K) the interpolated values are overrated. The general trend is visible for any color-color combination and therefore a linear fit can be done to correct this trend. The fit parameter of the linear fits (function: $f(x) = mx + t$) in both plots are:

- log(g) = 4.6: $m = -2.04 \pm 0.18$; $t = 67.65 \pm 5.81$
- log(g) = 5.4: $m = -1.83 \pm 0.17$; $t = 61.14 \pm 5.54$

For higher temperatures the errors get bigger since the degeneracy of the grid points become smaller and smaller.

To support spectroscopically derived temperatures the linear interpolation based on

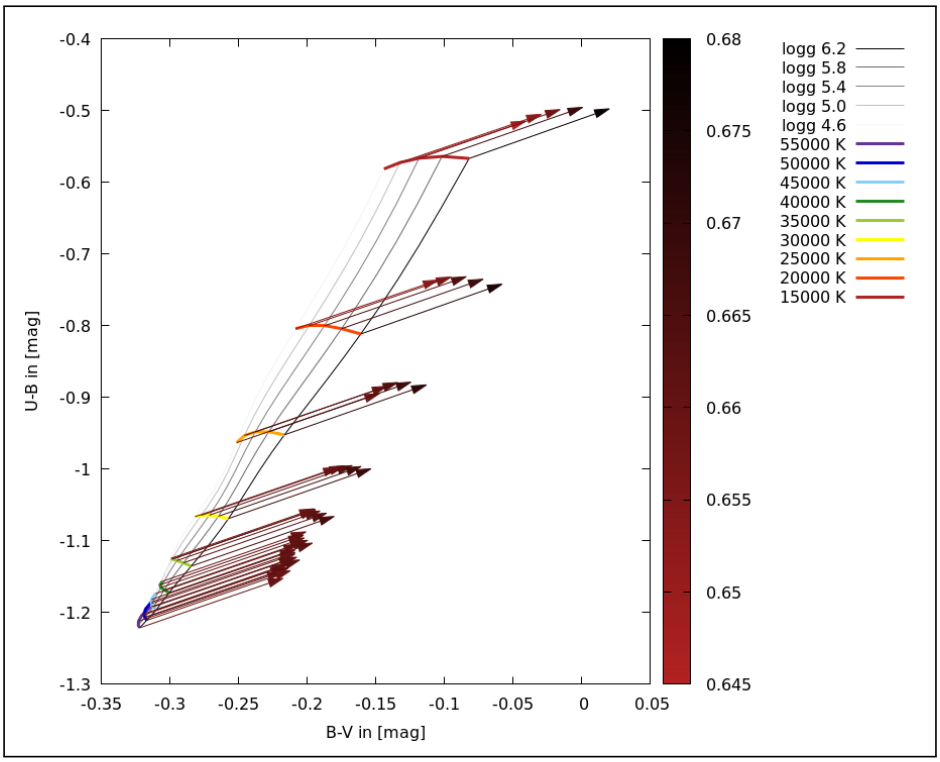

Figure 12: (U-B) vs. (B-V) in Johnson system: For every location in the grid ($15'000 < T_{eff} < 55'000$ K and $4.6 < log(g) < 6.2$ dex) the reddening vector is shown with the properties $E(B-V) = 0.1$ and $R_V = 3.1$. The color palette indicates the slope of the vectors. Only slight changes are observed.

reddening free indexes is acceptable in a range between 25'000 to 35'000 K by considering the bandpass combinations given in table 8.

5.3 Evaluation of color combinations

To evaluate which Color-Color diagrams or more specific which color combinations are appropriate to find binary systems, more than a hundred combinations were tested. The restriction to errors below 0.05 mag for every bandpass reduces the amount of stars with GALEX FUV and NUV filters significantly. The remaining stars are widely spread over the diagram (s. Fig. 16) so that it is not possible to distinguish the "bulge" (i.e. sdB's) from outliers (e.g. binaries) hence combinations with FUV and NUV filters are not suitable for a binary search.

Some combinations show this separation but the reddening vector is directed in a way that one can shift those stars upon the grid (s. Fig. 17). This should be avoided since we do not know the distances to the stars.

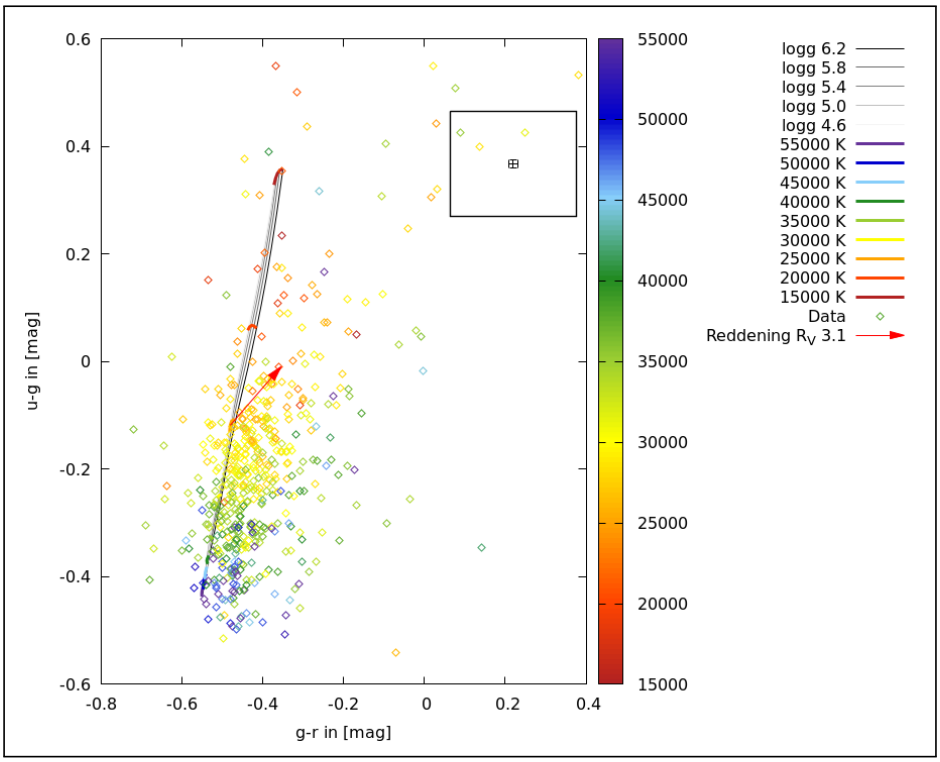

Figure 13: Color-Color diagram with Color indexes (u-g) and (g-r) from SDSS photometric data where the spectroscopic class "sdB" is provided and the atmospheric parameters effective temperature and log(g) are given. The reddening vector is based on an color excess $E(B-V)$ of 0.1 and interstellar reddening R_V of 3.1.

A careful consideration of the amount of stars available in a Color-Color combination, the direction of the reddening vector and a visible distinction of the "bulge" and the outliers leads to an exclusion of the combinations in table 7.

The remaining color-color and magnitude-color combinations are promising to identify binary systems. The combinations are given in table 8 and show that mainly broadband visual filters with JHK-bandpasses are used.

By plotting e.g. Gaia filters ($G_{BP} - G_{RP}$) against (J-K) UKIDSS (see Fig. 18) we see important criteria needed to find binary systems:

- The reddening vector lies in the direction of most stars
- Stars are mostly bundled in one region
- Outliers are clearly visible

A further example reveals some similarities between these combinations (s. Fig. 19). Instead of Gaia filters, the Johnson broadbands B and V are used and plotted versus

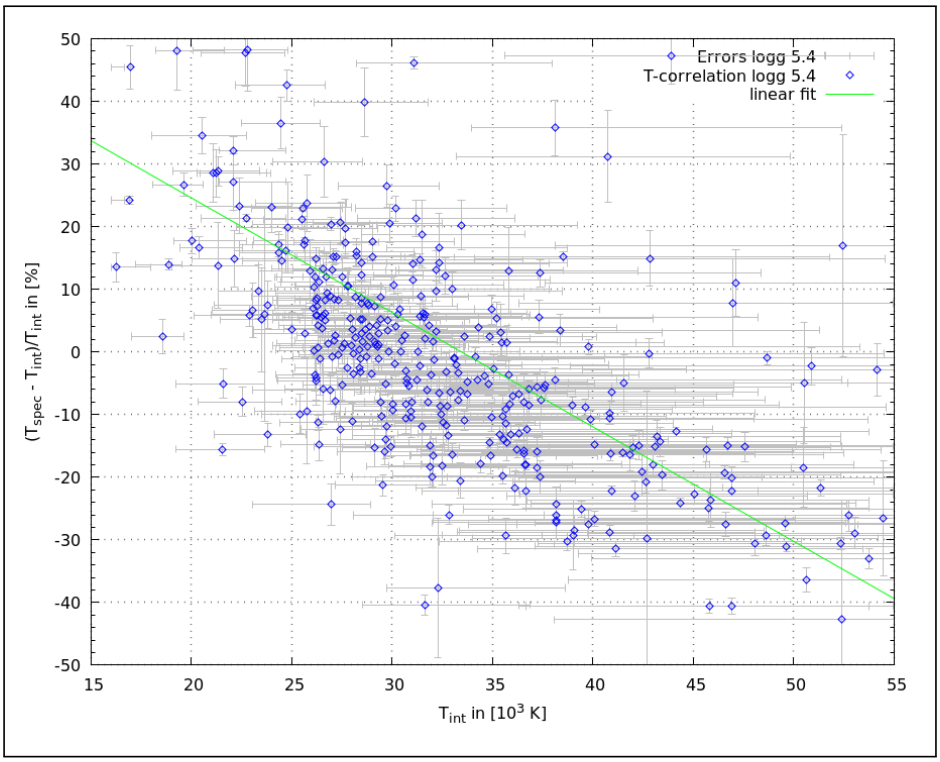

Figure 14: For Log(g)=5.4: The y-axis shows the difference between effective temperatures derived by spectroscopy (T_{spec}) and interpolation (T_{int}) in [%]. In light-grey the errorbars are visible. This derivation made use of (u-g) vs. (g-r) from SDSS. (Image replaced)

2MASS (J-K). Here one can also easily distinguish between the expected sdB single stars and the outliers.

5.4 Data sources

The basis for the photometric investigations in this work are the catalogs provided by Geier et al. (2017, 2019). The first catalog from Geier et al. (2017) contains 5'613 hot subdwarfs which is an extended version of the subdwarf database by Østensen (2006) with roughly 2'300 entries. Just small subsets of the first catalog have spectroscopically determined atmospheric parameters. These objects serve as a reference later. After identifying interesting objects via Color-Color diagrams spectral energy distributions will be constructed. The second catalog published by Geier et al. (2019) is a subset of the Gaia mission Data Release 2 (Collaboration et al. (2018)). With selection criteria such as restricting the absolute magnitudes, filtering by reduced proper motion, cutting out the Large Magellanic Cloud (LMC) and Small Magellanic Cloud (SMC) and more, this catalog contains now 39'800 hot compact objects from which 8'760 objects are selected via absolute magnitudes and 31'040 objects by reduced proper motions.

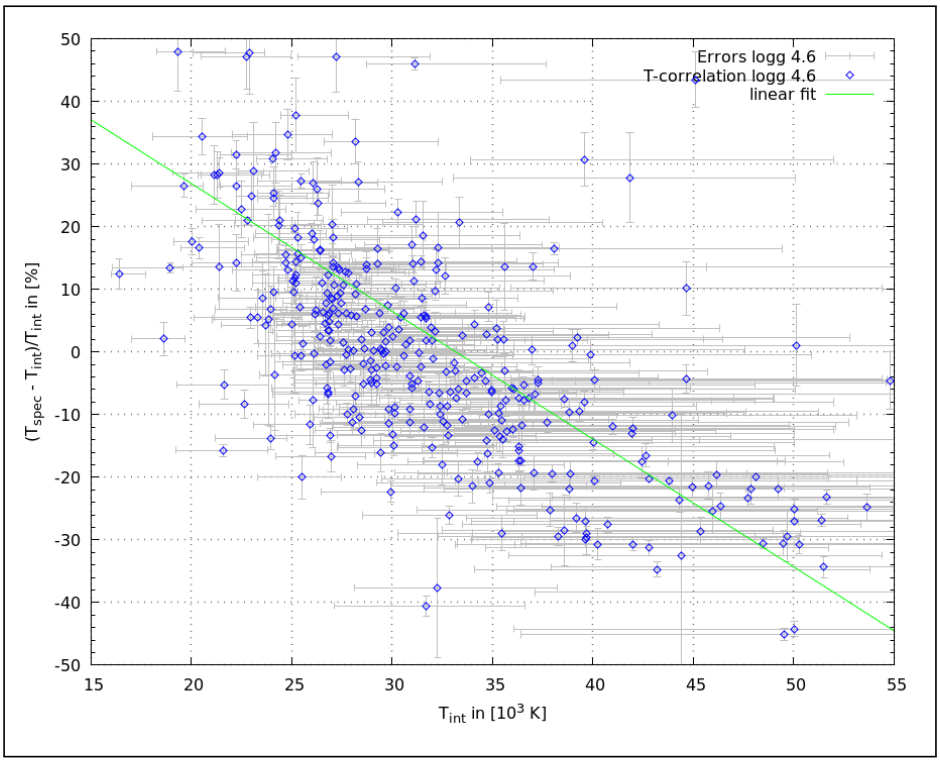

Figure 15: For Log(g)=4.6: The y-axis shows the difference between effective temperatures derived by spectroscopy (T_{spec}) and interpolation (T_{int}) in [%]. In light-grey the errorbars are visible. This derivation made use of (u-g) vs. (g-r) from SDSS. (Image replaced)

The methods derived from the small sample (subset of catalog I) are used as a reference to remove outliers in the big sample (catalog II), such as white dwarfs, and to identify composite systems. For the whole investigation following basic constraints are set:

- $13 < m_{bp} < 18$ mag
- $0 < m_{err} < 0.05$ mag

with m_{bp} as the magnitude of an arbitrary bandpass and m_{err} the corresponding error.

5.5 Small sample

The small sample contains 5'613 unique sources and is provided by Geier et al. (2017). This catalog is accessible only via ftp to cdsarc.u-strasbg.fr (130.79.128.5) or via the website `http://cdsarc.u-strasbg.fr/viz-bin/qcat?J/A+A/600/A50`. The sources are spectroscopically specified as subdwarf B stars (roughly 50% of all objects), sdOB,

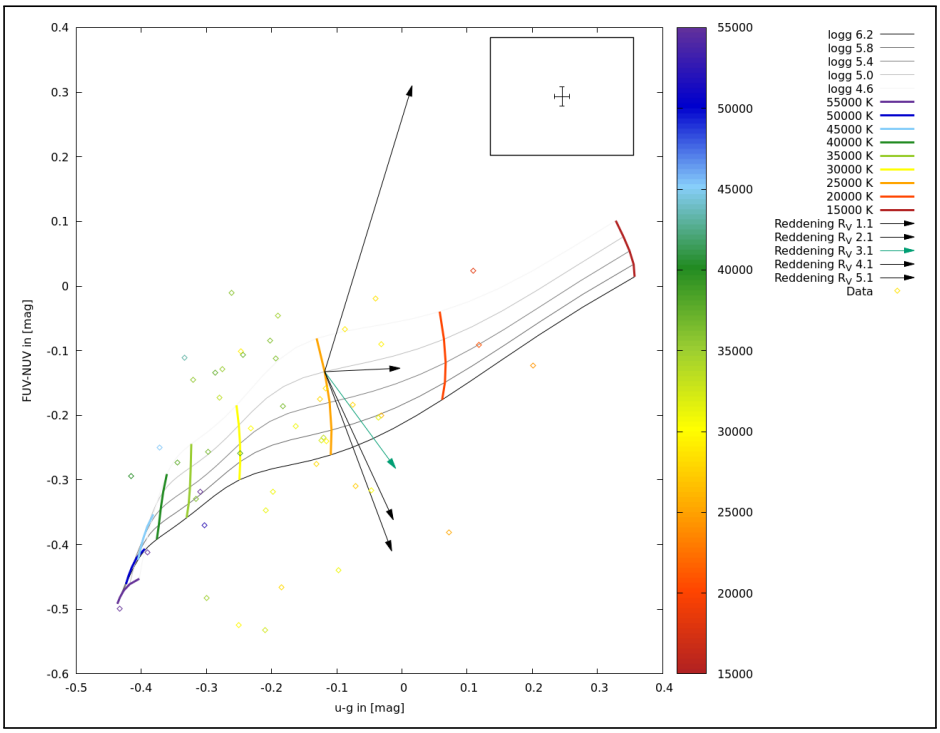

Figure 16: Color-Color diagram with Color indexes (FUV-NUV) from GALEX and (u-g) from SDSS photometric data where the spectroscopic class "sdB" is provided and the atmospheric parameters effective temperature and log(g) are given. The reddening vectors (black) correspond to $R_V \in 1.1, 2.1, 4.1, 5.1$ and the reddening vector (green) is based on $R_V = 3.1$. The color excess is for all vectors $E(B-V) = 0.1$.

sdO, He-sdB/sdOB/sdO, binaries of subdwarf plus main-sequence star and approximately 10% unclassified. But only 16 % of all objects have also atmospheric parameters provided. In Fig. 20 the coordinates of all objects in this catalog can be seen.

The coverage is a representation of the underlying surveys and therefore the northern hemisphere is quite crowded at relatively high Galactic latitudes. In the following, a subset of all objects shown in Fig. 20 is defined and evaluated. By setting constraints for each color-color diagram e.g. $J-K > 0.3$ just 62 entries remained overall. The distinct set (double entries removed) reduced the sample to 36 stars which are analysed in the following. For all 36 candidates SEDs have been constructed as single stars as well as binary systems. The data out of these fits will be further supported by the interstellar extinction which was calculated via NASA/IPAC Extragalactic Database (NED) coordinate and extinction calculator. The results (s. table 9) show a good agreement for most stars between the calculated extinction and the extinction received from the spectral energy distributions. Taking all this sign into account a flag value was defined with:

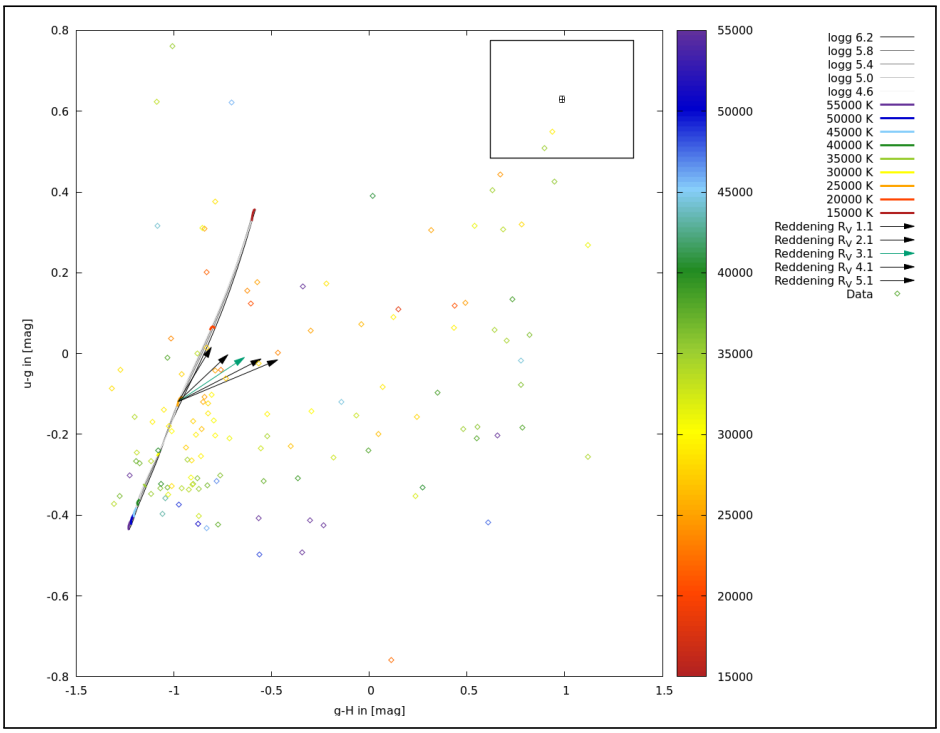

Figure 17: Color-Color diagram with Color indexes (u-g) from SDSS and (g-H) from SDSS and 2MASS survey where the spectroscopic class "sdB" is provided and the atmospheric parameters effective temperature and log(g) are given. The reddening vectors (black) correspond to $R_V \in 1.1, 2.1, 4.1, 5.1$ and the reddening vector (green) is based on $R_V = 3.1$. The color excess is for all vectors $E(B-V) = 0.1$.

- **1**: likely a binary system,
- **0**: not enough data to evaluate,
- **-1**: unlikely a binary system.

All objects with a flag value of 1 in table 9 have an infrared excess in common which indicates a cool companion. In addition, most of them show an elongated GALEX image on `http://aladin.u-strasbg.fr/AladinLite/` and the color excess values from different sources are in good agreement.

In the following some of the important features of a binary system will be pointed out with some examples (BD+293070, EC11031-1348, EC12546-1540, GALEX J17278+1644). Similar argumentation is applied on all other with flag 1 marked stars in table 9. Subsequently, cases with flag 0 will be discussed (HS2206+2847, PG0111+177, PG1629+081, PG2317+046, SDSSJ105700.58+593015.34) and finally it will be clarified how probable single stars got into this sample (OGLE BUL-SC16 335, PG1336-018, PG1558-007).

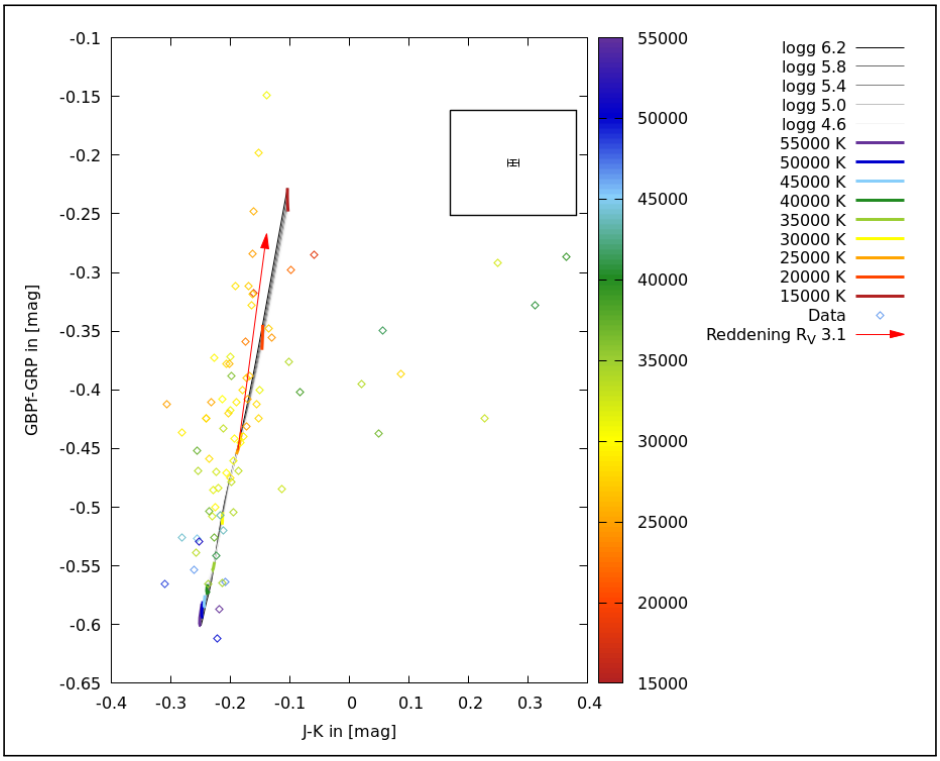

Figure 18: Color-Color diagram with Color indexes (G_{BP}-G_{RP}) from Gaia and (J-K) from UKIDSS photometric data where the spectroscopic class "sdB" is provided and the atmospheric parameters effective temperature and log(g) are given. The reddening vector is based on an color excess $E(B-V)$ of 0.1 and interstellar reddening R_V of 3.1.

Bandpass 1	Bandpass 2	Bandpass 3	Bandpass 4	Bandpass 1	Bandpass 2	Bandpass 3	Bandpass 4
B Johnson	V Johnson	GBPf Gaia	-	FUV GALEX	NUV GALEX	B Johnson	-
B Johnson	V Johnson	GBPf Gaia	GRP Gaia	FUV GALEX	NUV GALEX	B Johnson	V Johnson
B Johnson	V Johnson	H UKIDSS	-	FUV GALEX	NUV GALEX	GBPf Gaia	-
B Johnson	V Johnson	H UKIDSS	K UKIDSS	FUV GALEX	NUV GALEX	GBPf Gaia	-
B Johnson	V Johnson	J 2MASS	-	FUV GALEX	NUV GALEX	GBPf Gaia	GRP Gaia
B Johnson	V Johnson	J UKIDSS	-	FUV GALEX	NUV GALEX	H 2MASS	-
B Johnson	V Johnson	J UKIDSS	H UKIDSS	FUV GALEX	NUV GALEX	H 2MASS	K 2MASS
B Johnson	V Johnson	J UKIDSS	K UKIDSS	FUV GALEX	NUV GALEX	H UKIDSS	-
B Johnson	V Johnson	r SDSS	-	FUV GALEX	NUV GALEX	H UKIDSS	K UKIDSS
B Johnson	V Johnson	r SDSS	i SDSS	FUV GALEX	NUV GALEX	J 2MASS	-
B Johnson	V Johnson	r SkyMapper	-	FUV GALEX	NUV GALEX	J 2MASS	H 2MASS
B Johnson	V Johnson	r SkyMapper	i SkyMapper	FUV GALEX	NUV GALEX	J 2MASS	K 2MASS
B Johnson	V Johnson	u SDSS	-	FUV GALEX	NUV GALEX	J UKIDSS	-
B Johnson	V Johnson	u SDSS	g SDSS	FUV GALEX	NUV GALEX	J UKIDSS	H UKIDSS
B Johnson	V Johnson	u Stroemgren	-	FUV GALEX	NUV GALEX	J UKIDSS	K UKIDSS
B Johnson	V Johnson	u Stroemgren	v Stroemgren	FUV GALEX	NUV GALEX	r SDSS	-
B Johnson	V Johnson	v Stroemgren	-	FUV GALEX	NUV GALEX	r SDSS	i SDSS
B Johnson	V Johnson	v Stroemgren	b Stroemgren	FUV GALEX	NUV GALEX	r SkyMapper	-
B Johnson	V Johnson	W1 WISE	W2 WISE	FUV GALEX	NUV GALEX	r SkyMapper	i SkyMapper
GBPf Gaia	GRP Gaia	H 2MASS	K 2MASS	FUV GALEX	NUV GALEX	u SDSS	-
GBPf Gaia	GRP Gaia	H UKIDSS	-	FUV GALEX	NUV GALEX	u SDSS	g SDSS
GBPf Gaia	GRP Gaia	J UKIDSS	-	FUV GALEX	NUV GALEX	u Stroemgren	-
GBPf Gaia	GRP Gaia	r SDSS	-	FUV GALEX	NUV GALEX	u Stroemgren	v Stroemgren
GBPf Gaia	GRP Gaia	r SDSS	i SDSS	FUV GALEX	NUV GALEX	v Stroemgren	-
GBPf Gaia	GRP Gaia	r SkyMapper	-	FUV GALEX	NUV GALEX	v Stroemgren	b Stroemgren
GBPf Gaia	GRP Gaia	r SkyMapper	i SkyMapper	FUV GALEX	NUV GALEX	W1 WISE	-
GBPf Gaia	GRP Gaia	u SDSS	-	FUV GALEX	NUV GALEX	W1 WISE	W2 WISE
GBPf Gaia	GRP Gaia	u SDSS	g SDSS	NUV GALEX	J 2MASS	H 2MASS	-
GBPf Gaia	GRP Gaia	W1 WISE	W2 WISE	NUV GALEX	J 2MASS	H 2MASS	K 2MASS
u Stroemgren	v Stroemgren	b Stroemgren	-	NUV GALEX	J UKIDSS	H UKIDSS	-
u Stroemgren	v Stroemgren	b Stroemgren	y Stroemgren	NUV GALEX	J UKIDSS	H UKIDSS	K UKIDSS
u Stroemgren	v Stroemgren	GBPf Gaia	-	NUV GALEX	U Johnson	B Johnson	-
u Stroemgren	v Stroemgren	GBPf Gaia	GRP Gaia	NUV GALEX	U Johnson	B Johnson	V Johnson
u Stroemgren	v Stroemgren	H 2MASS	-	NUV GALEX	u SDSS	r SDSS	-
u Stroemgren	v Stroemgren	H 2MASS	K 2MASS	NUV GALEX	u SkyMapper	v SkyMapper	-
u Stroemgren	v Stroemgren	H UKIDSS	-	NUV GALEX	u SkyMapper	v SkyMapper	g SkyMapper
u Stroemgren	v Stroemgren	H UKIDSS	K UKIDSS	NUV GALEX	u Stroemgren	v Stroemgren	-
u Stroemgren	v Stroemgren	J 2MASS	-	NUV GALEX	u Stroemgren	v Stroemgren	-
u Stroemgren	v Stroemgren	J 2MASS	H 2MASS	NUV GALEX	u Stroemgren	v Stroemgren	b Stroemgren
u Stroemgren	v Stroemgren	J 2MASS	K 2MASS	u SDSS	g SDSS	H 2MASS	-
u Stroemgren	v Stroemgren	J UKIDSS	-	u SDSS	g SDSS	H 2MASS	K 2MASS
u Stroemgren	v Stroemgren	J UKIDSS	H UKIDSS	u SDSS	g SDSS	H UKIDSS	-
u Stroemgren	v Stroemgren	J UKIDSS	K UKIDSS	u SDSS	g SDSS	H UKIDSS	K UKIDSS
u Stroemgren	v Stroemgren	r SDSS	-	u SDSS	g SDSS	J 2MASS	-
u Stroemgren	v Stroemgren	r SDSS	i SDSS	u SDSS	g SDSS	J UKIDSS	-
u Stroemgren	v Stroemgren	r SkyMapper	-	u SDSS	g SDSS	J UKIDSS	H UKIDSS
u Stroemgren	v Stroemgren	r SkyMapper	i SkyMapper	u SDSS	g SDSS	J UKIDSS	K UKIDSS
u Stroemgren	v Stroemgren	u SDSS	-	u SDSS	g SDSS	r SDSS	-
u Stroemgren	v Stroemgren	u SDSS	g SDSS	u SDSS	g SDSS	r SDSS	i SDSS
u Stroemgren	v Stroemgren	W1 WISE	-	u SDSS	g SDSS	r SkyMapper	-
u Stroemgren	v Stroemgren	W1 WISE	W2 WISE	u SDSS	g SDSS	r SkyMapper	i SkyMapper
u SkyMapper	v SkyMapper	H 2MASS	-	u SDSS	g SDSS	u SkyMapper	-
u SkyMapper	v SkyMapper	H 2MASS	K 2MASS	u SDSS	g SDSS	u SkyMapper	v SkyMapper
u SkyMapper	v SkyMapper	H UKIDSS	-	u SDSS	g SDSS	W1 WISE	-
u SkyMapper	v SkyMapper	H UKIDSS	K UKIDSS	u SDSS	g SDSS	W1 WISE	W2 WISE
u SkyMapper	v SkyMapper	J 2MASS	-				
u SkyMapper	v SkyMapper	J 2MASS	H 2MASS				
u SkyMapper	v SkyMapper	J 2MASS	K 2MASS				
u SkyMapper	v SkyMapper	J UKIDSS	-				
u SkyMapper	v SkyMapper	J UKIDSS	H UKIDSS				
u SkyMapper	v SkyMapper	J UKIDSS	K UKIDSS				
u SkyMapper	v SkyMapper	W1 WISE	-				
u SkyMapper	v SkyMapper	W1 WISE	W2 WISE				

Table 7: Bandpasses which are not appropriate to search binaries. The colors are usually c_1 = (Bandpass 1 - Bandpass 2) and c_2 = (Bandpass 3 - Bandpass 4). In the case of Bandpass 4 = "-", the colors are c_1 = (Bandpass 1 - Bandpass 2) and c_2 = (Bandpass 2 - Bandpass 3).

Bandpass 1	Bandpass 2	Bandpass 3	Bandpass 4
G_{BP} Gaia	G_{RP} Gaia	J UKIDSS	H UKIDSS
G_{BP} Gaia	G_{RP} Gaia	J UKIDSS	K UKIDSS
G_{BP} Gaia	G_{RP} Gaia	J 2MASS	K 2MASS
G_{BP} Gaia	G_{RP} Gaia	J 2MASS	H 2MASS
G_{BP} Gaia	G_{RP} Gaia	H UKIDSS	K UKIDSS
G_{BP} Gaia	G_{RP} Gaia	H 2MASS	-
B Johnson	V Johnson	W1 WISE	-
B Johnson	V Johnson	J 2MASS	H 2MASS
B Johnson	V Johnson	H 2MASS	-
G_{BP} Gaia	G_{RP} Gaia	W1 WISE	-

Table 8: Bandpasses used to search unseen companions. The colors are usually c_1 = (Bandpass 1 - Bandpass 2) and c_2 = (Bandpass 3 - Bandpass 4). In the case of Bandpass 4 = "-", the colors are c_1 = (Bandpass 1 - Bandpass 2) and c_2 = (Bandpass 2 - Bandpass 3).

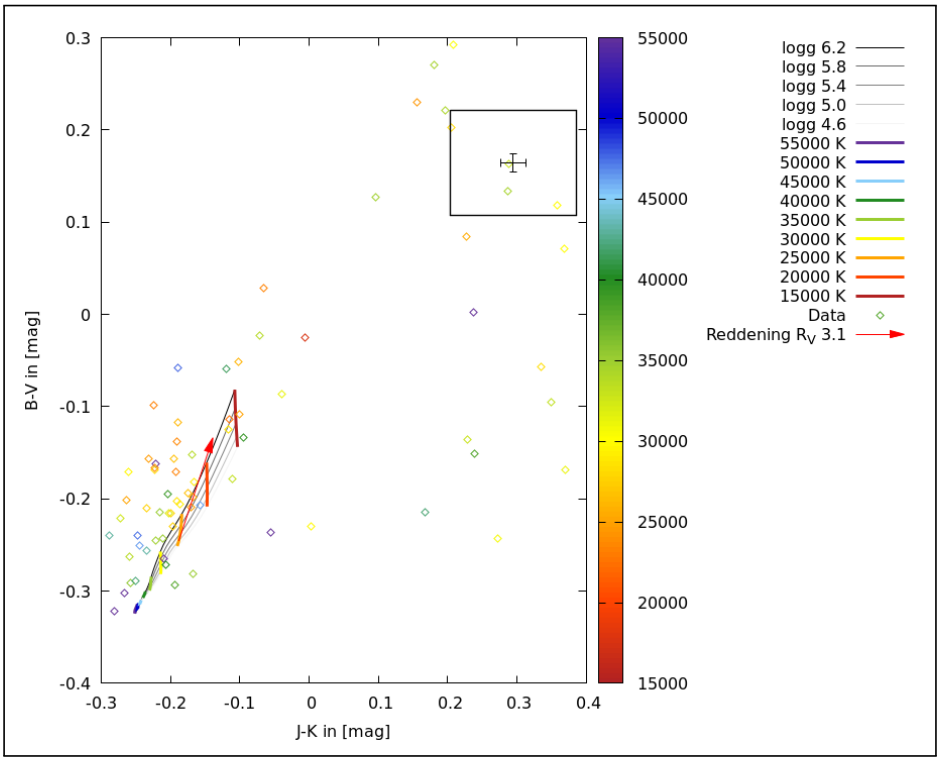

Figure 19: Color-Color diagram with Color indexes (B-V) from Johnson system and (J-K) from 2MASS photometric data where the spectroscopic class "sdB" is provided and the atmospheric parameters effective temperature and log(g) are given. The reddening vector is based on an color excess $E(B-V)$ of 0.1 and interstellar reddening R_V of 3.1.

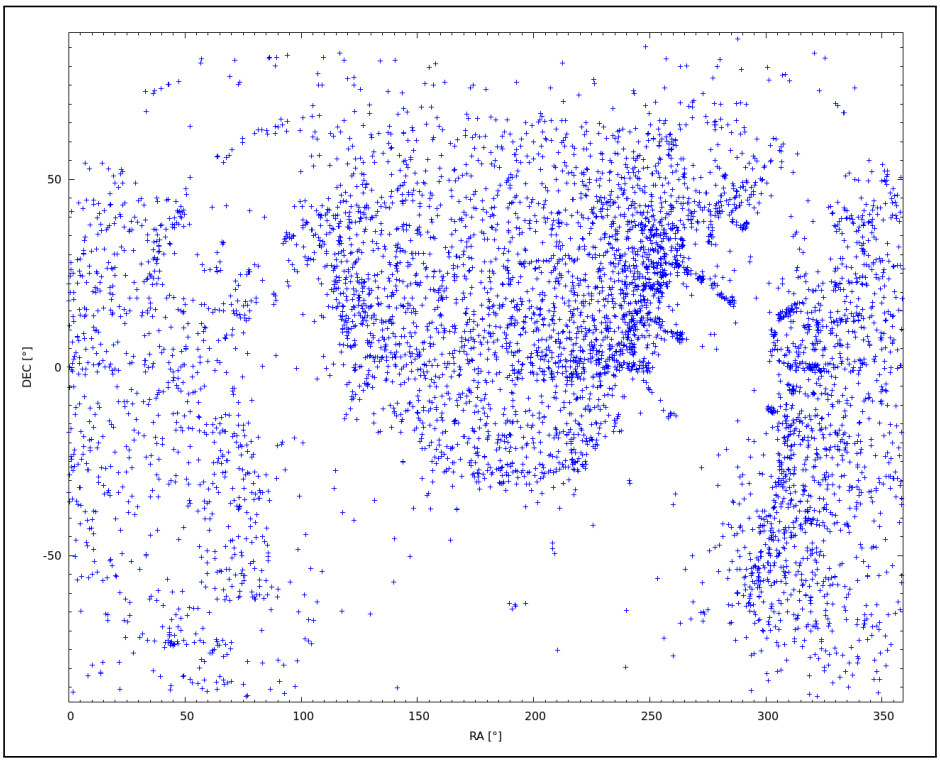

Figure 20: Coordinates of all 5613 stars (small sample). The empty band represents the Galactic disk.

Identifier	$E(B-V)^{[1]}$	$E(B-V)^{[2]}$	E(B-V) SED	Flag	SpClass (SIMBAD)	Source SpClass
BD+293070	0.0465	0.0565	0.019	1	sdOB+F/G	(Berger & Fringant, 1980)
EC11031-1348	0.0397	0.0474	0.057	1	sdB+GV	(Vennes et al., 2011)
EC12546-1540	0.0568	0.0690	0	1	sdB+G0	(Lisker et al., 2005)
EC13527-1827	0.0794	0.0968	0.061	1	sdB+G3	(Lisker et al., 2005)
GALEXJ02103+0830	0.0500	0.0610	0	1	sdB+F2IV	(Németh et al., 2012)
GALEXJ05073-2802	0.0139	0.0168	0.08	1	-	-
GALEXJ08259+1307	0.0306	0.0371	0	1	sdB	(Németh et al., 2012)
GALEXJ10179+5516	0.0090	0.0106	0.09	1	sdB+F5V	(Németh et al., 2012)
GALEXJ13564-4934	0.1794	0.2158	0.07	1	sdB	(Vennes et al., 2011)
GALEXJ16190+4831	0.0097	0.0123	0.172	1	sdB+F0V	(Németh et al., 2012)
GALEXJ17278+1644	0.0732	0.0903	0	1	sdB	(Németh et al., 2012)
GALEXJ20209-2250	0.0597	0.0710	0.018	1	sdB+G0V	(Németh et al., 2012)
GALEXJ20222+0152	0.1526	0.1826	0	1	sdB+F6V	(Németh et al., 2012)
GALEXJ21005+1452	0.0829	0.0994	0.03	1	sdB+F5.5IV-V	(Németh et al., 2012)
GALEXJ022454.87+010938.81	0.0319	0.0377	0.04	1	sdB+F4V	(Németh et al., 2012)
GALEXJ065736.93-732449.60	0.1161	0.1432	0.395	1	sdB	(Vennes et al., 2011)
GALEXJ175340.57-500741.80	0.1548	0.1852	0.05	1	sdB+F7V	(Németh et al., 2012)
GALEXJ203850.22-265747.16	0.0668	0.0842	0.55	1	sdO+G3.5III	(Németh et al., 2012)
GALEXJ211230.92-152410.37	0.0823	0.1052	0.23	1	-	-
GALEXJ214022.87-371414.05	0.0281	0.0342	0.18	1	sdB+F6V	(Németh et al., 2012)
HS2206+2847	0.0787	0.0958	0	0	sdB	(Edelmann et al., 2003)
OGLE BUL-SC16 335	1.1877	1.4355	1.02	0	sdB+dM	(Barlow et al., 2013)
PG0111+177	0.0500	0.0590	0.05	0	D	(Green et al., 1986)
PG1258+012	0.0223	0.0265	0	1	sdOHe	(Stroeer et al., 2007)
PG1336-018	0.0410	0.0458	0.02	-1	sdB1VIIHe1	(Drilling et al., 2013)
PG1558-007	0.1603	0.1942	0.139	-1	sdB3VIIHe3	(Drilling et al., 2013)
PG1559+076	0.0416	0.0510	0	1	sdO	(Green et al., 1986)
PG1623+386	0.0081	0.0094	0	1	sdB	(Wegner & Dupuis, 1993)
PG1629+081	0.0674	0.0803	0	0	sdOB+K5V	(Barlow et al., 2012)
PG2223+171	0.0545	0.0661	0	1	sdBO	(Green et al., 1986)
PG2317+046	0.0552	0.0681	0.05	0	sdO8VIIHe1	(Drilling et al., 2013)
SDSSJ105700.58+593015.34	0.0090	0.0110	0	0	sdB	(Kepler et al., 2016)
SDSSJ121514.66+284522.55	0.0194	0.0223	0	1	sdB	(Kepler et al., 2016)
SDSSJ152705.03+110843.9	0.0319	0.0390	0	1	sdOB	(Geier et al., 2011)
SDSSJ154923.48+163023.80	0.0352	0.0403	0	1	D+M	(Kepler et al., 2015)
SDSSJ170716.53+275410.4	0.1197	0.1474	0	1	sdB+/?	(Luo et al., 2016)

Table 9: Reddening values for 36 stars sample. The color excess E(B-V) is provided by two external sources ([1]=Schlafly & Finkbeiner (2011); [2]=Schlegel et al. (1998)) and by the SED fit. The flag value: (1)=likely binary system, (0)=not enough data to evaluate, (-1)=unlikely binary system.

BD+293070 BD+293070 shows a strong infrared excess and the color excess E(B-V) is in good agreement with the values provided by NED. With a temperature derived from the binary SED of the first component of $T_{eff} = 25600^{+5700}_{-2300}$ K and the second component $T_{eff} = 6400^{+250}_{-140}$ K this system could be sdB or sdOB star with a late type F-star or early type G-star companion which is also claimed by Berger & Fringant (1980). BD+293070 is roughly 0.8 magnitudes brighter in infrared H-filter (2MASS) and 0.9 magnitude in W1 (WISE) than in the visual V-band (Johnson). Unfortunately no UKIDSS data are available for this star but in combination with the constructed SED the assumption that we face a binary system is pretty convincing.

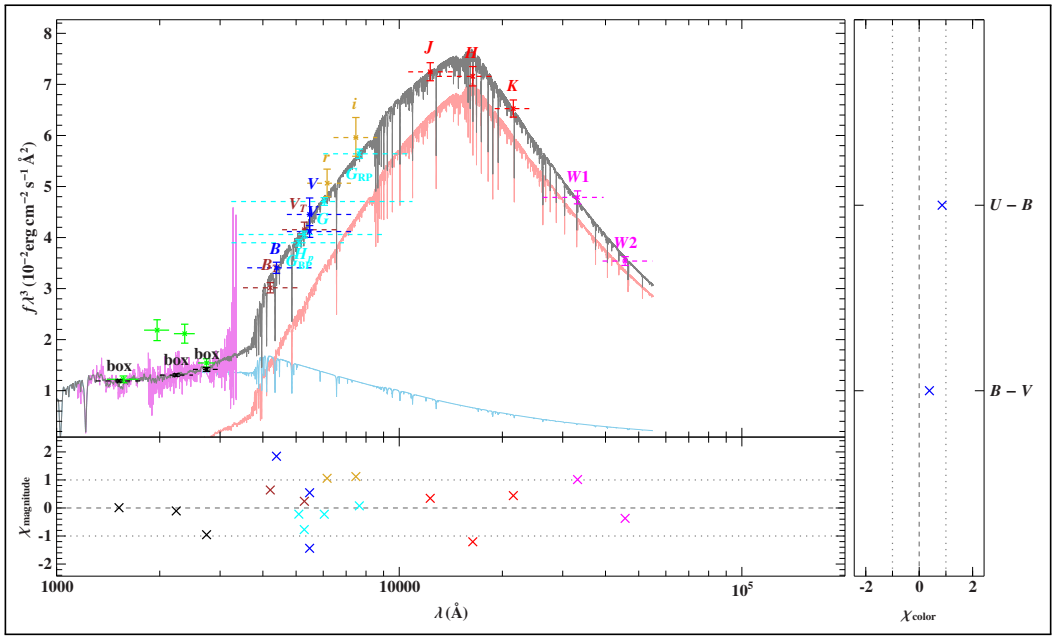

Figure 21: BD+293070; Top: Spectral Energy Distribution grey: combined, light-blue: subdwarf B, red: Cool companion. Bottom: Deviation of the photometric data from the actual SED in $[mag]$. The x-axis is the wavelength given in $[\AA]$.

EC11031-1348 EC11031-1348 seems to be a binary system containing a sdB and a mid- to late type F stars a a companion. The temperature of both stars are $T_{eff} = 28500^{+2000}_{-3200}$ K for the subdwarf and $T_{eff} = 6650^{+40}_{-120}$ K for the main-sequence star. The color excess determined from the SED is approximately is in the range the reddening map predicts. The slight deviation to the result of Vennes et al. (2011) who got a sdB plus a GV star out of spectroscopic analysis could be caused by the GALEX filter which does not fit perfectly in this SED.

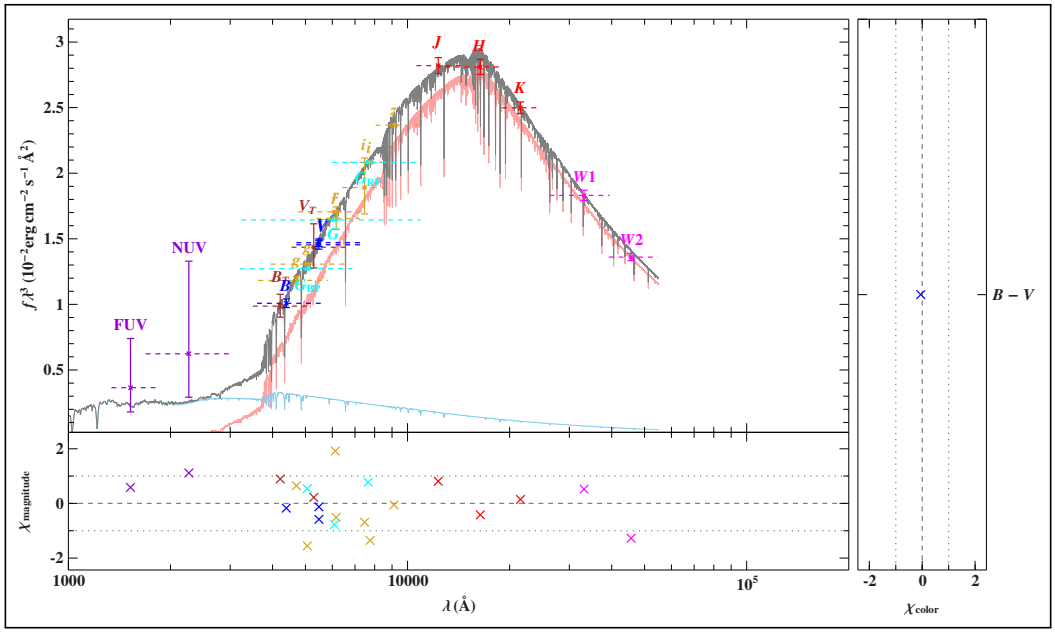

Figure 22: EC11031-1348; Top: Spectral Energy Distribution grey: combined, light-blue: subdwarf B, red: Cool companion. Bottom: Deviation of the photometric data from the actual SED in $[mag]$. The x-axis is the wavelength given in $[\AA]$.

EC12546-1540 EC12546-1540 is a nice example where data from far-UV up to mid-IR are available. Narrow u- and v-filter (SkyMapper) provide information about the Balmer continuum whereas infrared filter from VISTA fit very well to the SED. The given 2MASS filters are not too reliable since the deviation (including errors) is higher than one σ. But this star was chosen with respect to Johnson V-magnitude and WISE W1-magnitude. The result is a binary system with a sdB ($T_{eff} = 27200^{+1500}_{-1000}$ K) and a K4 to K6 star ($T_{eff} = 4340^{+190}_{-180}$ K) companion. Since the SED gives a color excess E(B-V) of roughly null and the values of Schlafly & Finkbeiner (2011) and Schlegel et al. (1998) are 0.0568 and 0.0690, we see a good agreement in the excess. The surface ratio is $18.5^{+1.7}_{-1.6}$ which is an expected ratio of a cool companion in comparison with a subdwarf.

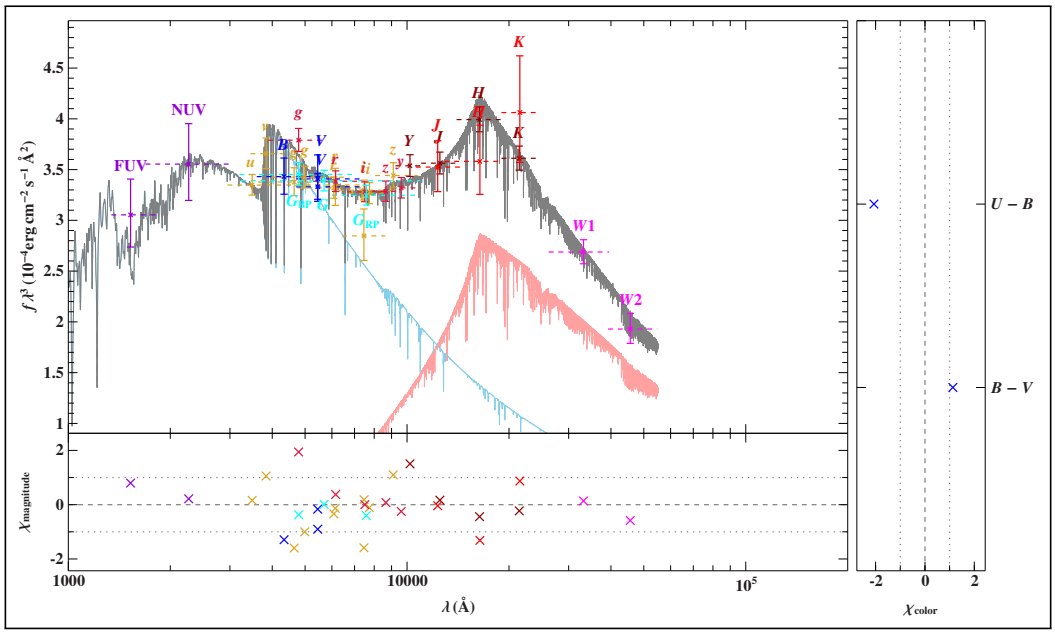

Figure 23: EC12546-1540; Top: Spectral Energy Distribution grey: combined, light-blue: subdwarf B, red: Cool companion. Bottom: Deviation of the photometric data from the actual SED in $[mag]$. The x-axis is the wavelength given in $[Å]$.

GALEX J17278+1644 According to spectroscopic investigations of Németh et al. (2012) GALEX J17278+1644 has no companion. However, the spectral energy distribution reveals a strong infrared excess. The derived temperatures of $T_{eff} = 16400^{+2700}_{-1900}$ K for the subdwarf component and $T_{eff} = 4530^{+200}_{-190}$ K for the companion lead to the assumption that this is a binary system with an early type K-star. Nevertheless, the temperature is too low to be a subdwarf B star. GALEX filter as well as the narrow u- and v-bands to cover the Balmer jump would be important to confirm the temperature of the first component. The color excess fits also quite well to the from NED provided ones. The methods of identifying companions by Németh et al. (2012) are limited to brighter companions with significant contribution and strong lines (like A- or F-stars). Late G- and K-stars are not easy to detect with their method since "the most significant effect on the flux is a slight flattening of the flux in the red part of the spectrum and relatively strong Na D lines" (Németh et al., 2012).

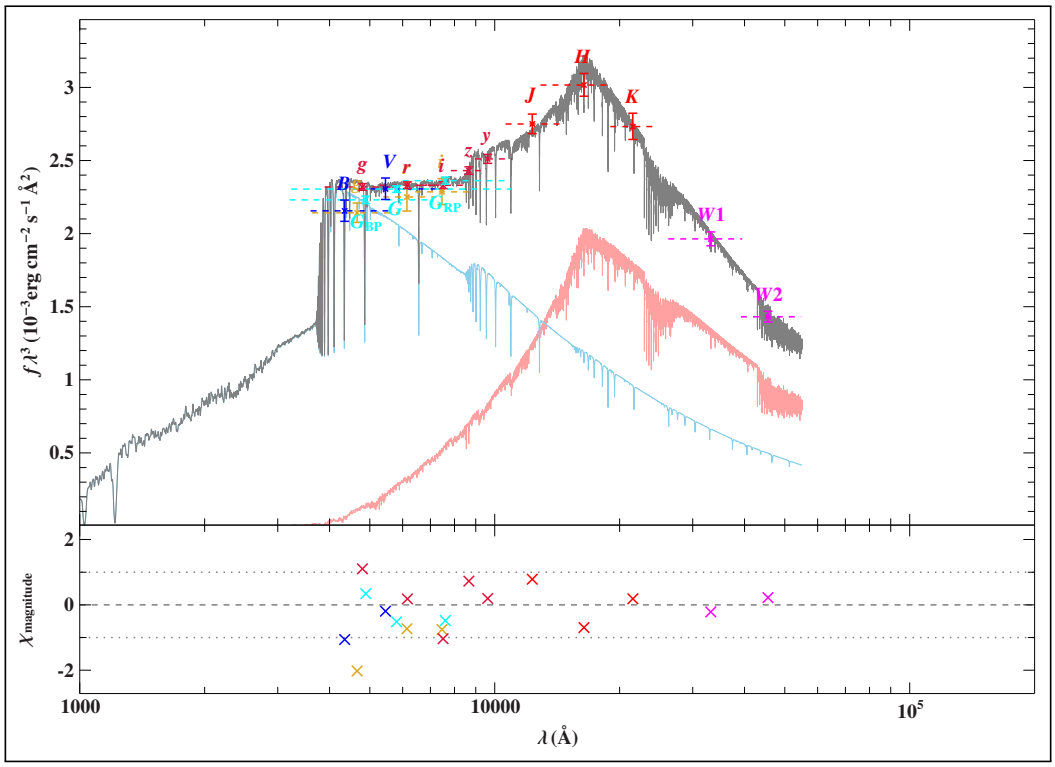

Figure 24: GALEX J17278+1644; Top: Spectral Energy Distribution grey: combined, light-blue: subdwarf B, red: Cool companion. Bottom: Deviation of the photometric data from the actual SED in $[mag]$. The x-axis is the wavelength given in $[\AA]$.

HS2206+2847 HS2206+2847 was classified by Edelmann et al. (2003) as a single subdwaf B star. Photometric data, however, reveal a trend for an infrared excess (s. Fig. 25). But due to a lack of photometric data in the K-band and mid-IR the binary SED gives just a poor assumption on the temperatures both components would have. As a single fit (s. Fig. 26) the H-filter seems to be an outlier and all Gaia filters are

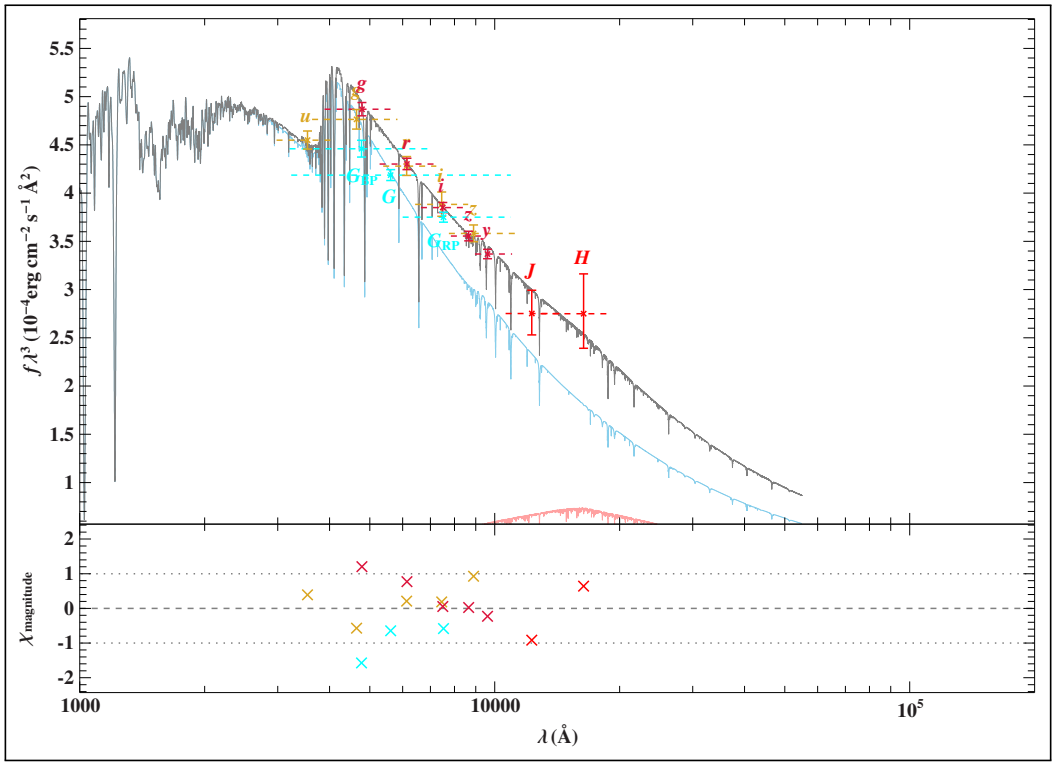

Figure 25: Binary fit: HS2206+2847; Top: Spectral Energy Distribution grey: combined, light-blue: subdwarf B, red: Cool companion. Bottom: Deviation of the photometric data from the actual SED in $[mag]$. The x-axis is the wavelength given in $[Å]$.

at least one σ away from the SED. But the derived temperature is $T_{eff} = 29900^{+2700}_{-2200}$ K which is within the range of a subdwarf B star. Furthermore, the color excess calculated from the SED fit is in agreement with Schlegel et al. (1998) and Schlafly & Finkbeiner (2011). With given data the single star scenario is more likely than a binary system and fits to Edelmann et al. (2003) determination. Unfortunately, the 2MASS K-magnitude is not reliable and WISE data are not available for this source. By taking a look on a 2MASS snapshot of HS2206+2847 (s. Fig. 27) one can see a close infrared source which probably leads to a higher J- and H-band flux as a contamination. So, from stand-alone photometric data it can not be clarified if there is a companion or not but with images in different wavelength regimes a binary system can be excluded.

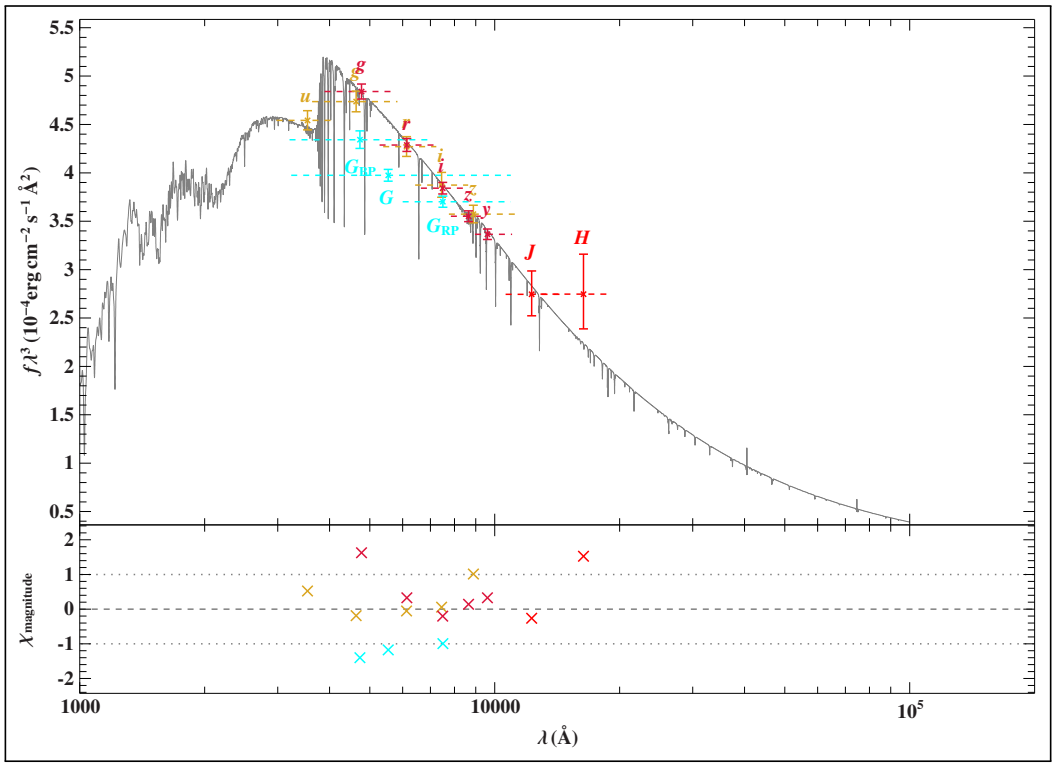

Figure 26: Single fit: HS2206+2847; Top: Spectral Energy Distribution grey: combined, light-blue: subdwarf fit. Bottom: Deviation of the photometric data from the actual SED in $[mag]$. The x-axis is the wavelength given in $[\mathring{A}]$.

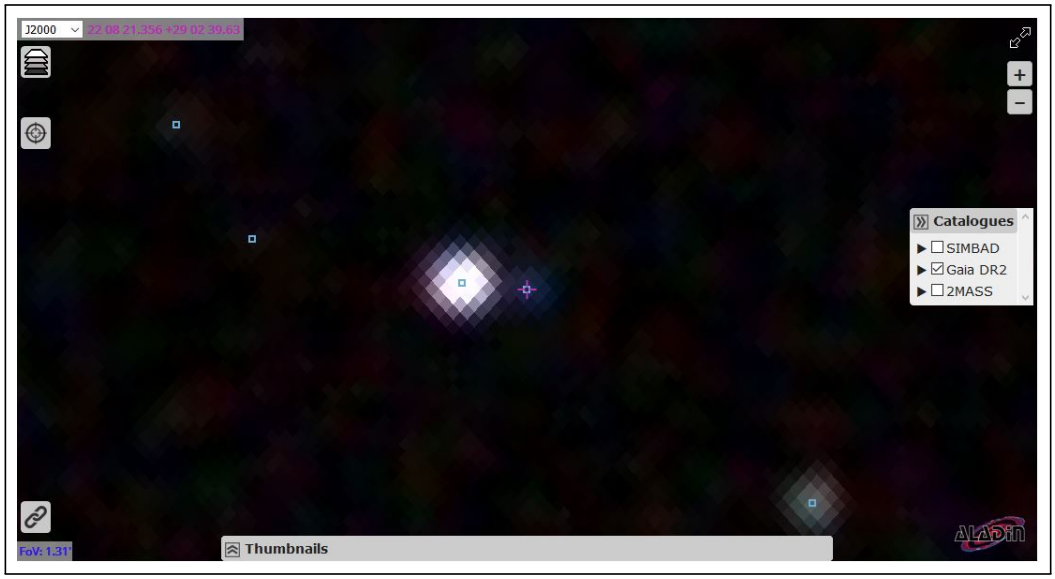

Figure 27: 2MASS image (coordinates: 22 08 21.356 +29 02 39.63) of HS2206+2847 with a field of view (FoV) 1.31 arcminutes. A Gaia sources (blue squares) is very close to our sample star. (Image taken from:`http://aladin.unistra.fr/AladinLite/?target=22%2008%2021.356%2B29%2002%2039.63&fov=0.02&survey=P%2F2MASS%2Fcolor`)

PG0111+177 PG0111+177 shows an excess i.e. in 2MASS J-filter (s. Fig. 28) but data from other surveys in the infrared regime are not available. The photometric data from 2MASS All-Sky Catalog of Point Sources (Skrutskie et al., 2006) offers also values in H- and K-band but without an uncertainty and therefore these filters are not reliable. Passbands from far-UV up to z- and y-band fit in the binary SED as well as in the single stars SED. The structure we see in the infrared could be some molecular bands of a K- or M-star companion or just an artefact due to lack of data.

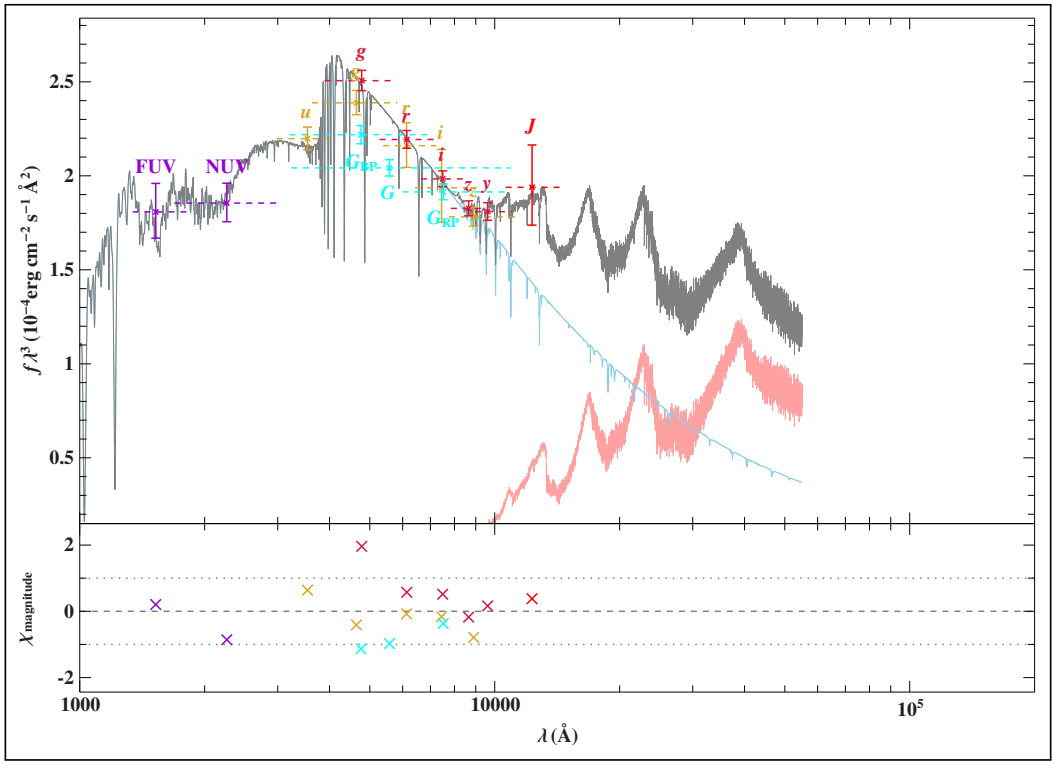

Figure 28: PG0111+177; Top: Spectral Energy Distribution grey: combined, light-blue: subdwarf B, red: Cool companion. Bottom: Deviation of the photometric data from the actual SED in $[mag]$. The x-axis is the wavelength given in $[Å]$.

PG1629+081 In the SED of PG1629+081 (s. Fig. 29) an excess in the infrared can be seen. The shape of the SED in this region does not look like expected by a cool companion even by considering molecular bands of a M-star. With its double peak it seems rather like a disk around the star. Moreover, the surface ratio from the SED fit gives 52^{+48}_{-9} which is way higher than expected from a cool companion. Also, the errors are too high so that the fit runs against the border. A more precise argumentation would be possible if the 2MASS J-band and WISE W1-band were not classified as outlier. So, with given data is not possible to say PG1629+081 is a binary system or a single star but it is more likely a single star.

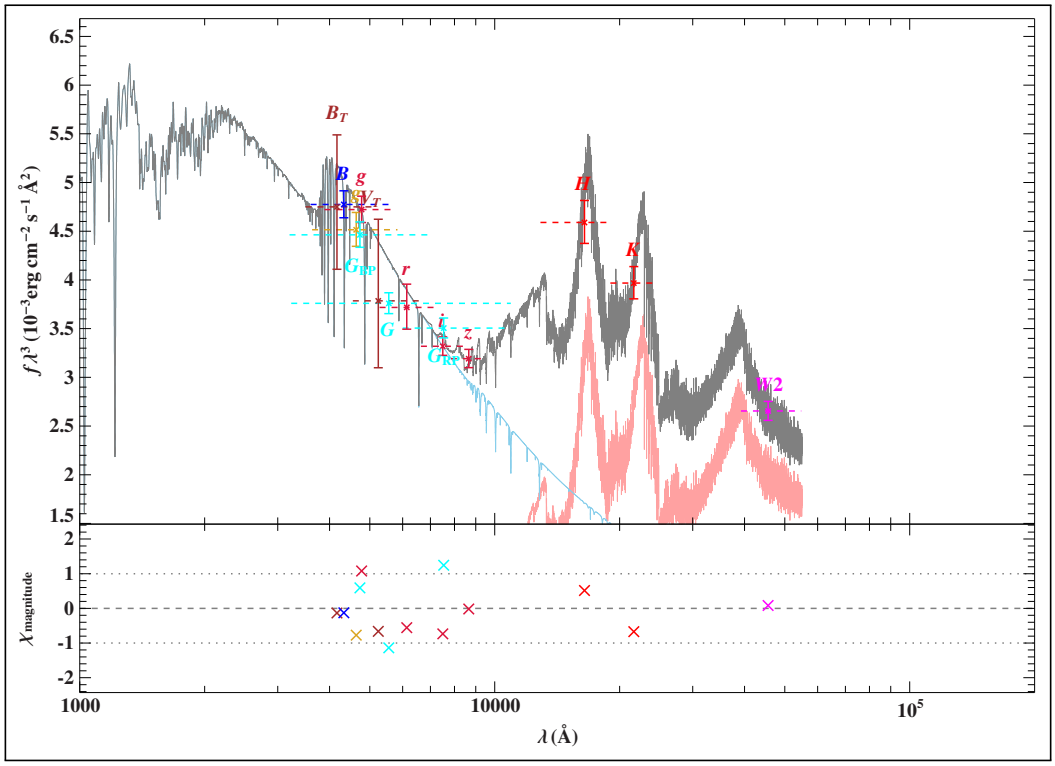

Figure 29: PG1629+081; Top: Spectral Energy Distribution grey: combined, light-blue: subdwarf B, red: Cool companion. Bottom: Deviation of the photometric data from the actual SED in $[mag]$. The x-axis is the wavelength given in $[Å]$.

PG2317+046 This star has some reasonable and convincing parameters received from the SED fit. The extinction parameter compared to the extinction maps is in an acceptable range. The temperature derived from the first component is $T_{eff} = 23000^{+6000}_{-4000}$ K and the second one gives $T_{eff} = 3300^{+840}_{-250}$ K. The surface ratio between both model stars is 13^{+7}_{-4} which is exactly what we expect. The excess in infrared is also given with a structure resulting from a K6 to M6 star. Even though some filters are more than one σ away from the modeled SED and no narrow u- and v-bands are available, the SED (s. Fig. 30) seems to be convincing. But by considering the images on `http://aladin.u-strasbg.fr/AladinLite/` it does not seem to be a binary system. Within a field of view of roughly 1 arcminute there are no sources in the 2MASS infrared band which could influence the central star (s. Fig. 31) and also there is no evidence of a companion. The same situation is given in the SDSS bands (s. Fig. 32) where we see a single source. So, the only possibility for a binary system is that the main-sequence companion is located such that it can not be seen on the images. The conclusion is that with given photometric data it is not possible to determine PG2317+046 as a binary system.

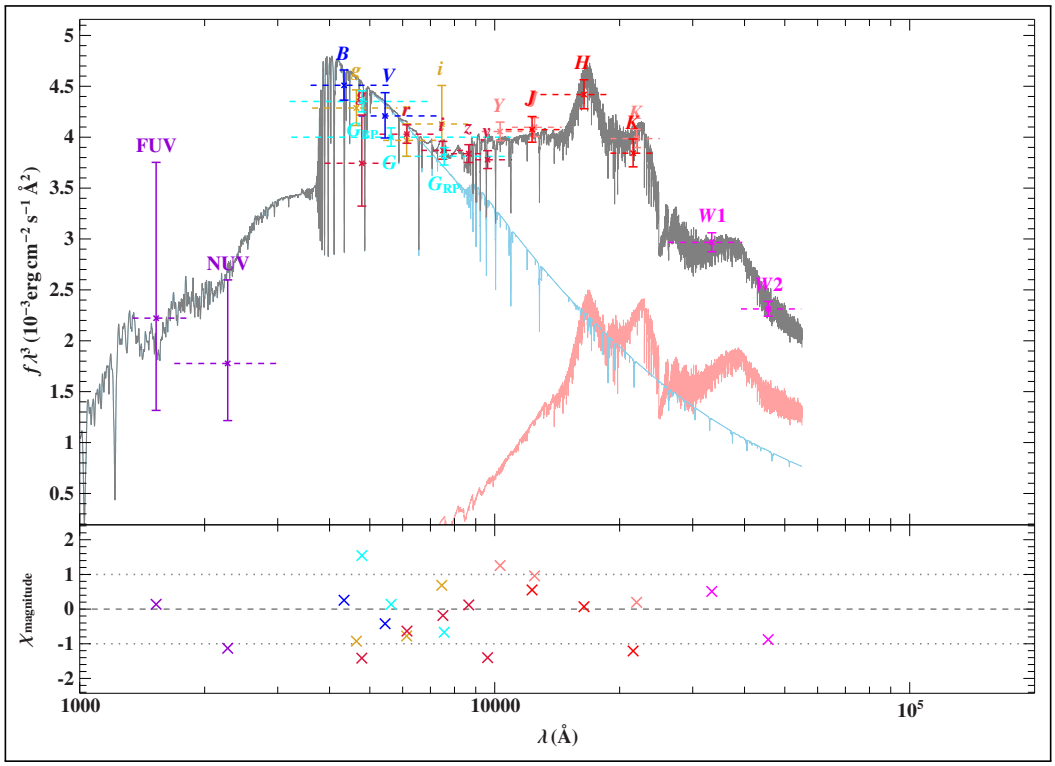

Figure 30: PG2317+046; Top: Spectral Energy Distribution grey: combined, light-blue: subdwarf B, red: Cool companion. Bottom: Deviation of the photometric data from the actual SED in $[mag]$. The x-axis is the wavelength given in $[Å]$.

Figure 31: 2MASS image (coordinates: 23 19 55.351 +04 52 34.66) of PG2317+046 with a field of view (FoV) 1.31 arcminutes. The blue squares represent Gaia sources. (Image taken from:`http://aladin.unistra.fr/AladinLite/?target=23%2019%2055.351%2B04%2052%2034.66&fov=0.02&survey=P%2F2MASS%2Fcolor`)

Figure 32: SDSS DR 9 image (coordinates: 23 19 55.351 +04 52 34.66) of PG2317+046 with a field of view (FoV) 1.31 arcminutes. The blue squares represent Gaia sources. (Image taken from:`http://aladin.unistra.fr/AladinLite/?target=23%2019%2055.351%2B04%2052%2034.66&fov=0.02&survey=P%2FSDSS9%2Fcolor`)

SDSSJ105700.58+593015.34 For this star only one magnitude in the infrared region (UKIDSS K-band) is provided by the VizieR Online Data Catalog: UKIDSS-DR9 LAS, GCS and DXS Surveys (Lawrence et al., 2013). This leads to an excess with a quite low contribution of a hypothetical companion. The values received from the SED fit (s. Fig. 33) give temperatures for the subdwarf component $T_{eff} = 24200^{+2100}_{-900}$ K and the cool star $T_{eff} = 4900 \pm 500$ K. At a first glance the values are reasonable since such binary systems are common . But the surface ratio of $5.5^{+1.3}_{-0.8}$ is too low. The expectation would be roughly $A_{K-star} \approx 12 \cdot A_{subdwarf}$ and even higher for G-type stars. More data in the infrared are necessary to clarify if the K-band magnitude is a contamination or the real value received from the star.

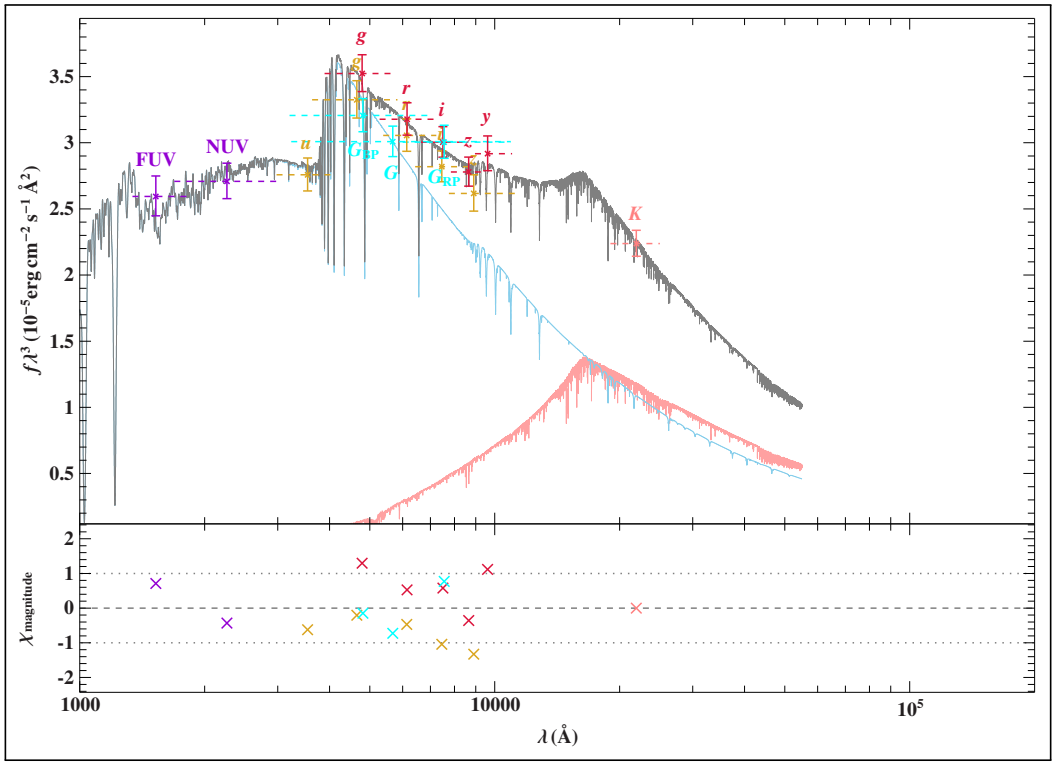

Figure 33: SDSSJ105700.58+593015.34; Top: Spectral Energy Distribution grey: combined, light-blue: subdwarf B, red: Cool companion. Bottom: Deviation of the photometric data from the actual SED in $[mag]$. The x-axis is the wavelength given in $[Å]$.

OGLE BUL-SC16 335 OGLE BUL-SC16 335 is an object within the Optical Gravitational Lensing Experiment (OGLE) (s. Szymański et al. (2000)) which is designed to look at crowded star regions such as the LMC, SMC or the Galactic bulge. So, the name refers to an object in the scan field 16 (SC16) of the bulge (BUL) within the experiment (OGLE). First photometric data of this object were provided in the J-, H- and K-band by Cutri et al. (2003). The SED seems corresponding to a strongly reddened star with an effective temperature of roughly $T_{eff} = 9000$ K in the binary fit (s. Fig. 34) as well as single star SED fit. OGLE BUL-SC16 is a crowded region, hence the contamination of other type of stars is quite high. In this case, the object is probably blended by other sources which explains that every filter in the visual and UV has been classified as outlier and just infrared filters remain. In the infrared the source seems to be clearly distinguishable from other sources (s. Figure 35) whereas in the visual wavelength range more object within some arcseconds can be seen (s. Fig. 36). Due to a lack of resolution in different wavelength regimes and contamination this object can neither be treated as a binary system nor a single star.

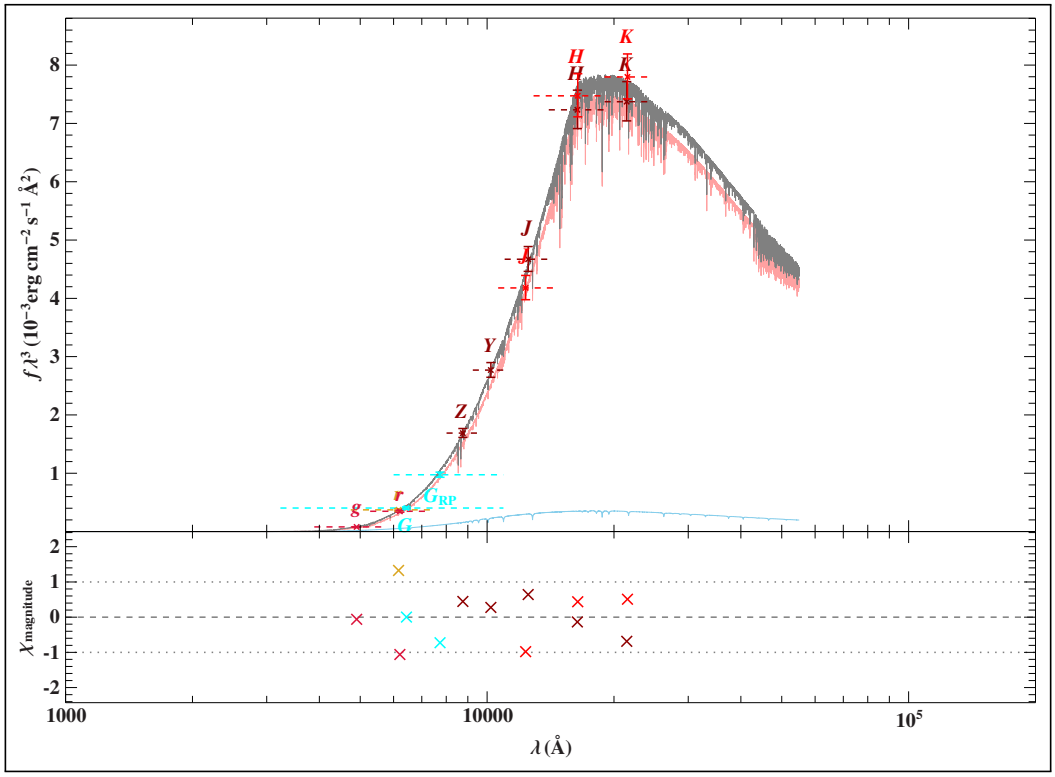

Figure 34: OGLE BUL-SC16 335; Top: Spectral Energy Distribution grey: combined, light-blue: subdwarf B, red: Cool companion. Bottom: Deviation of the photometric data from the actual SED in $[mag]$. The x-axis is the wavelength given in $[Å]$.

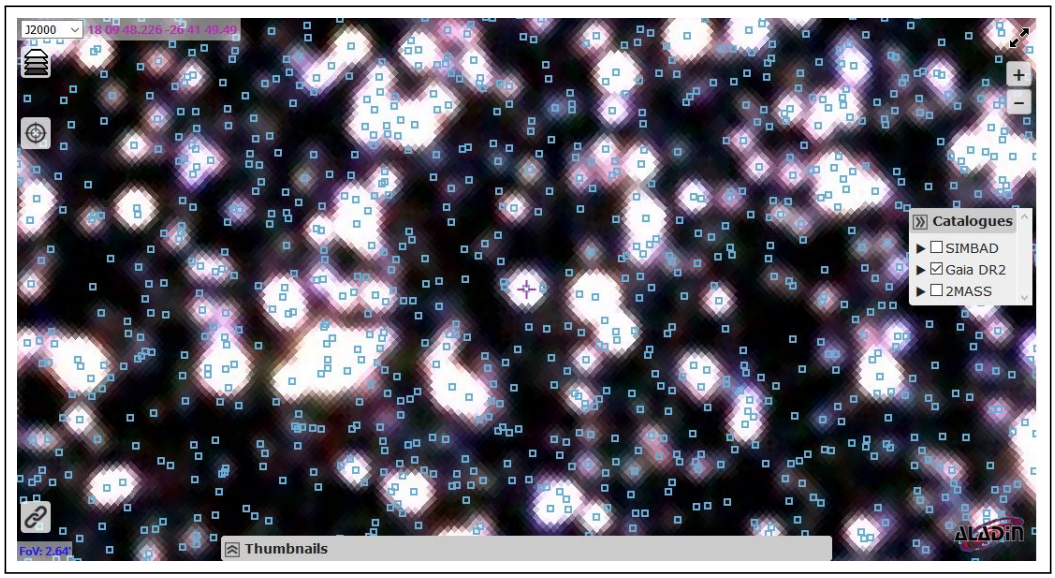

Figure 35: 2MASS image (coordinates: 18 09 48.226 -26 41 49.49) of OGLE BUL-SC16 335 with a field of view (FoV) 2.64 arcminutes. The crowded field is more obvious taking Gaia sources (blue squares) into account. (Image taken from:`http://aladin.unistra.fr/AladinLite/?target=18%2009%2048.226-26%2041%2049.49&fov=0.04&survey=P%2F2MASS%2Fcolor`)

Figure 36: PanSTARRS DR1 image (coordinates: 18 09 48.226 -26 41 49.49) of OGLE BUL-SC16 335 with a field of view (FoV) 2.64 arcminutes. (Image taken from: `http://aladin.unistra.fr/AladinLite/?target=18%2009%2048.226-26%2041%2049.49&fov=0.04&survey=P%2FPanSTARRS%2FDR1%2Fcolor-z-zg-g`)

PG1336-018 PG1336-018 is a single subdwarf star with an effective temperature of $T_{eff} = 31700^{+1800}_{-1500}$ K. According to Drilling et al. (2013) this is a subdwarf B star which is in agreement with the derived temperature from the SED. The object landed in this sample due to a UKIDSS color (J-H) > 0.2. But the algorithm carried out by the SED fit marked the J-filter as an outlier and removed it from the fit. By looking at the 2MASS color (J-H) the value is almost zero and therefore the object didn't appear in combinations with 2MASS colors. So, PG1336-018 is most likely a contamination in the small sample.

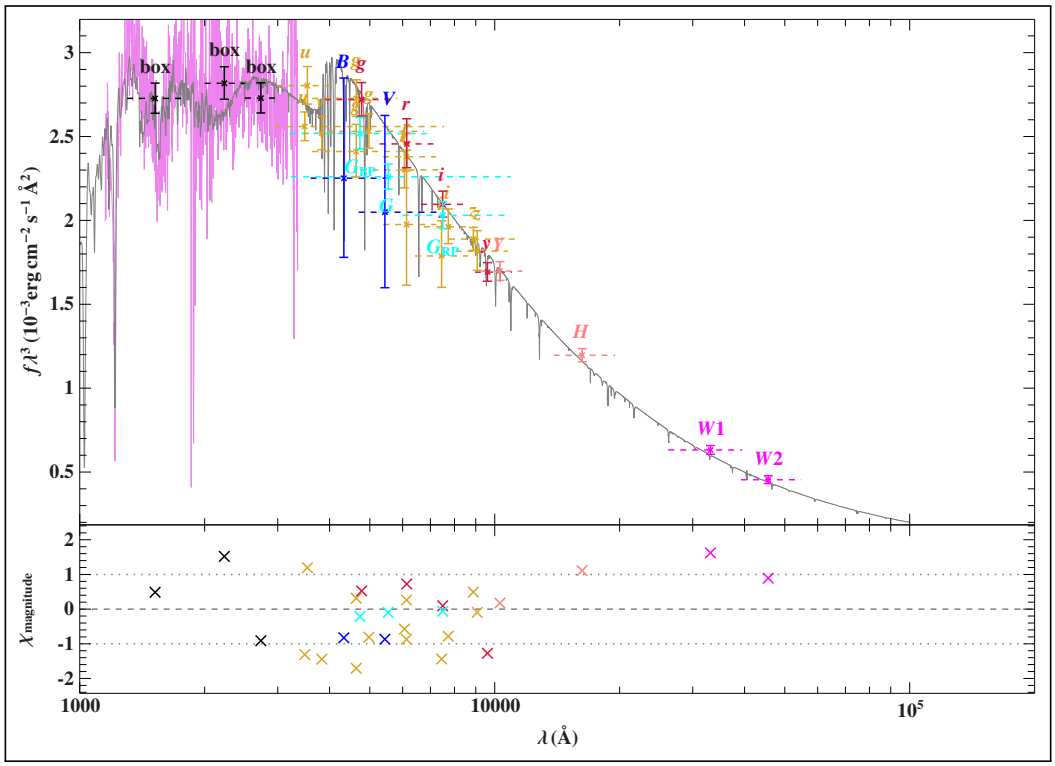

Figure 37: PG1336-018; Top: Spectral Energy Distribution grey: combined, light-blue: subdwarf B. Bottom: Deviation of the photometric data from the actual SED in $[mag]$. The x-axis is the wavelength given in $[\AA]$.

PG1558-007 The binary fit of PG1558-007 shows a system containing two subdwarfs (s. Fig. 38). But like this we can always construct binary systems. Most likely PG1558-007 is not a binary system since there is no indication in the infrared regime and also no special feature which could draw ones attention. The star appeared in the sample since it is much brighter (roughly 1.3 magnitudes) in W1 (WISE) than in the G_{RP} (Gaia red bandpass) which is a reasonable selection within a (G_{BP}-G_{RP}) vs. (G_{RP}-W1) diagram. By applying a single star fit (s. Fig. 39) more convincing results are

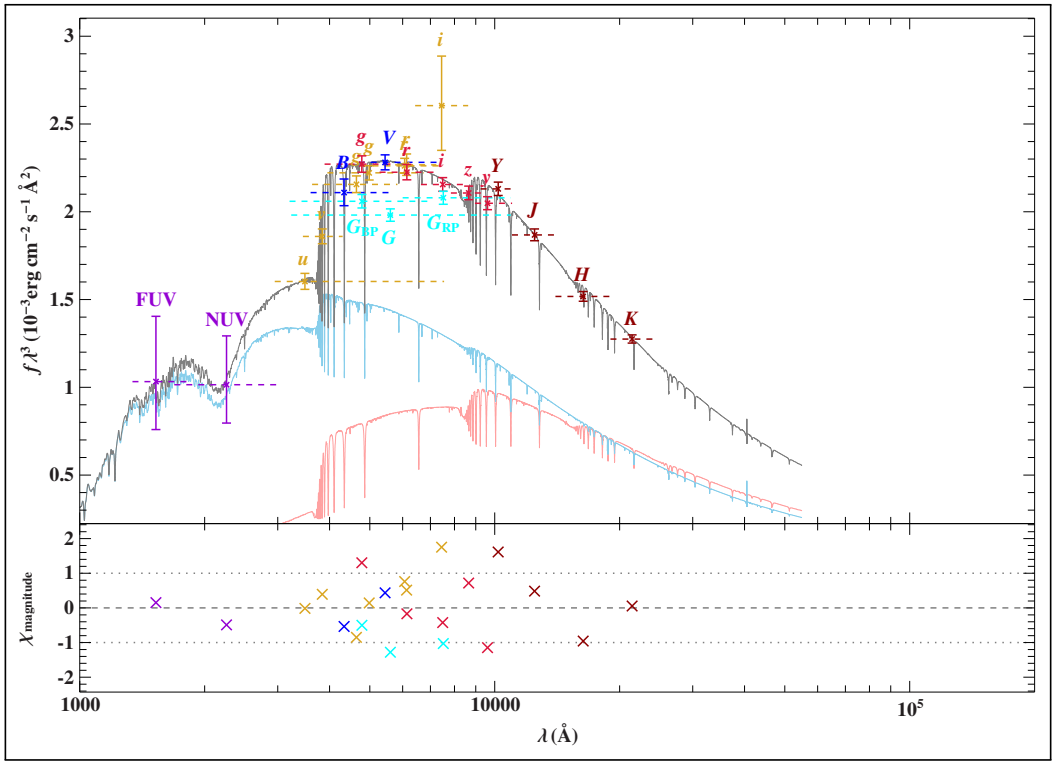

Figure 38: Binary fit: PG1558-007; Top: Spectral Energy Distribution grey: combined, light-blue: subdwarf B, red: Cool companion. Bottom: Deviation of the photometric data from the actual SED in [mag]. The x-axis is the wavelength given in [$\AA$].

given. Data from far-UV up to K-band are available. Filters for the Balmer jump (u-, v-SkyMapper) and for the Paschen jump (z-, y-PS1) fit also well to the fit. The effective temperature is $T_{eff} = 24000^{+1300}_{-1400}$ K with a surface gravity of $log(g) = 5.0^{+0.6}_{-0.4} cms^{-2}$ which imply a subdwarf B star. Drilling et al. (2013) also suggest PG1558-007 to be a subdwarf of type B, hence a single star is more likely.

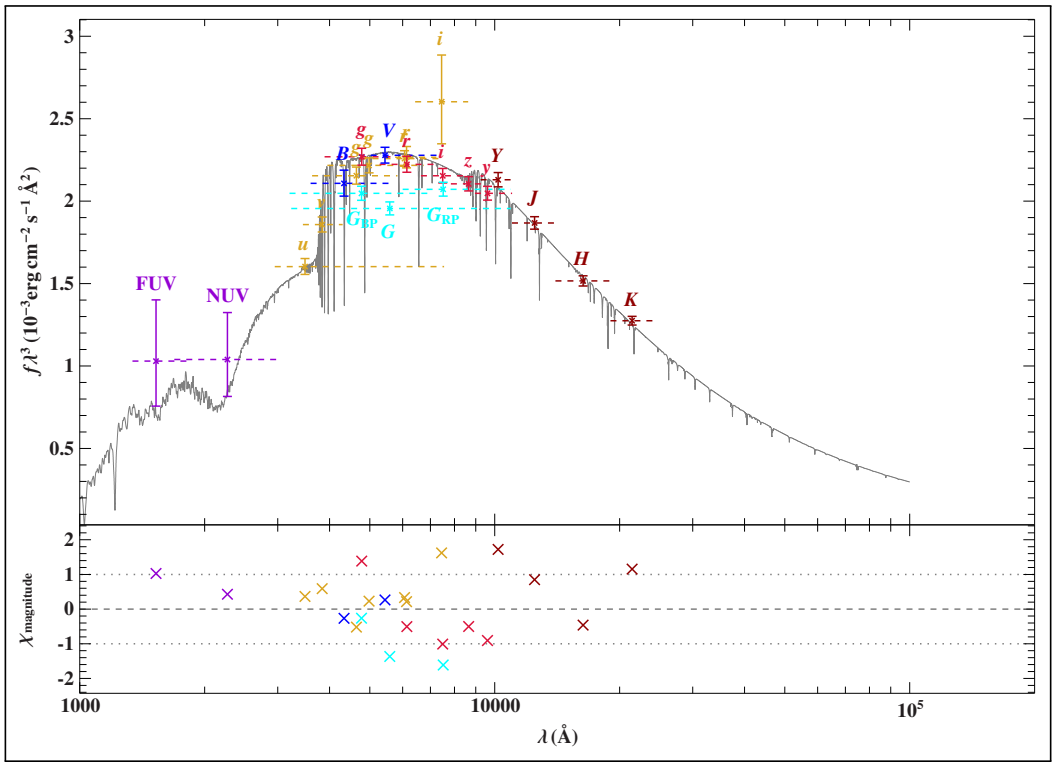

Figure 39: Single fit: PG1558-007; Top: Spectral Energy Distribution grey: combined, light-blue: subdwarf fit. Bottom: Deviation of the photometric data from the actual SED in $[mag]$. The x-axis is the wavelength given in $[\AA]$.

6 Big sample

The Gaia sample of subdwarf candidates (big sample) contains 39'800 sources. This catalog is accessible only via ftp to cdsarc.u-strasbg.fr (130.79.128.5) or via the website `http://cdsarc.u-strasbg.fr/viz-bin/qcat?J/A+A/621/A38`. Only 5'613 have been classified before. Hence, there are about 34'000 candidates to be classified. Gaia photometry is not sufficient due to a lack of color information. Therefore, additional photometry is needed. Many of the new candidates reside close to the Galactic disk, where ground based photometry is rare. The Sloan digital sky survey (SDSS) provides the largest set of additional photometry and covers large parts of the Northern sky. The amount of objects with available ugr-bands is 3'753, which we name the SDSS subsample of the Gaia sample of subdwarf candidates. A Color-Color digram is shown in Fig. 40.

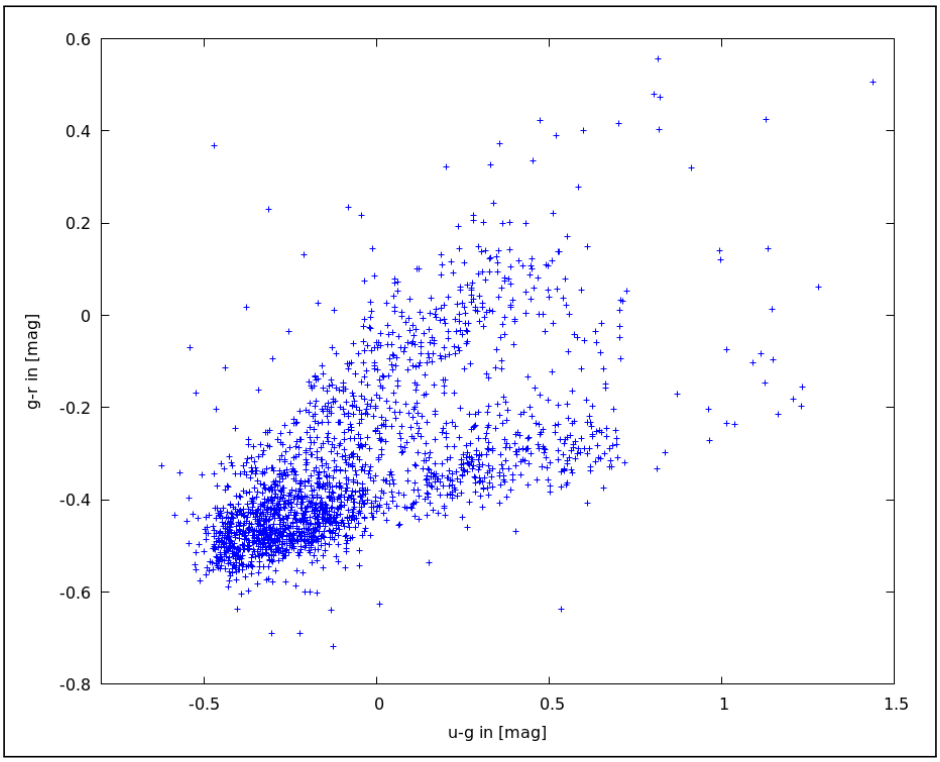

Figure 40: Color-Color diagram with Color indexes (u-g) and (g-r) from SDSS photometric data.

The first aim, described in Sect. 6.1 is the analysis of the SDSS subsample to determine the temperature distribution of single subdwarf stars and the identification of the potential binary population. The latter will suffer from contamination of blue horizontal branch stars of late B-type (HBB), hot post-AGB stars, stars of planetary nebulae and roughly 5% white dwarfs (Geier et al., 2019). Those candidates will not

be investigated further. The second aim, described in Sect. is to study objects close to the Galactic plane, where SDSS does not reach but sufficient photometry is available. For these randomly picked candidates the SED can be matched in detail.

6.1 SDSS subsample

From the whole sample 3'753 sources have magnitudes for the ugr-bands in the SDSS system. By applying a linear interpolation of the reddening free index Q temperatures were derived for 2'359 objects. The received temperatures have been corrected by the parameters of the linear fit in subsection 5.2 figure (14). Almost half of the stars do not hit a T_{eff} - $log(g)$ track by moving them along the reddening vector (s. Fig. 41). From the 2'359 objects only 467 sources have the spectral class "sdB" in the first catalog of Geier et al. (2017). The temperature distribution of the single sdB stars is rather equal to the objects which are not classified as single sdBs (s. Fig. 42). This is reasonable due to the fact that most of the objects do not have any spectral class provided and therefore the main part of these objects is believed to be of type sdB. The remaining 1'394 objects are probably white dwarfs, HBB stars and mainly binary systems of sdB's and cool main-sequence companions.

6.2 Sample close to the Galactic plane

For the binary search photometric data were filtered as in the small sample. The remaining, promising sources were crosschecked with those in the first catalog of Geier et al. (2017) and available sources on SIMBAD (`http://simbad.u-strasbg.fr/simbad/`). Objects with entries in either of these databases were excluded from the sample to investigate. As a last step only objects rather close to the disk were randomly chosen. This led to the remaining 14 objects (s. Fig. 43 (red)). For every object a binary SED fit has been carried out. The color excess E(B-V) was fixed to the mean value of the extinction provided by Schlegel et al. (1998) and Schlafly & Finkbeiner (2011). Effective temperatures and surface ratios for each candidate are listed in table 10. A flag value shows if the candidate is likely a binary system (1), important filter are missing to decide (0) or the object is probably not a compound (-1). In the following, four randomly chosen objects are discussed to point out the procedure.

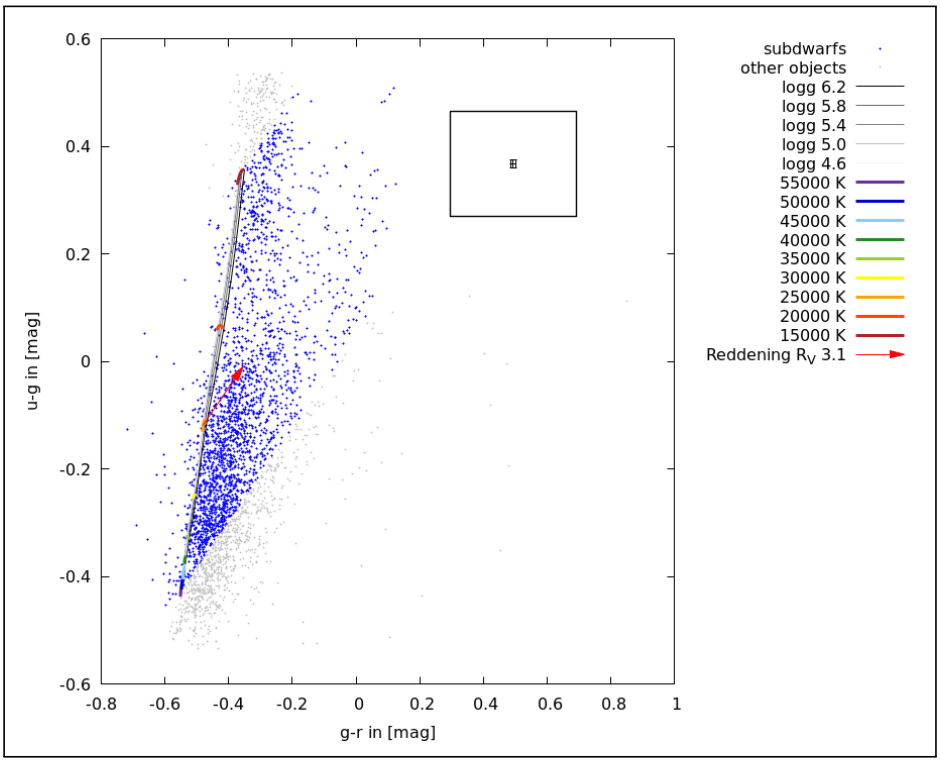

Figure 41: Color-Color diagram with Color indexes (u-g) and (g-r) from SDSS photometric data. Separation between 2'359 single subdwarf candidates (blue) and 1'394 other objects (grey). (Image replaced)

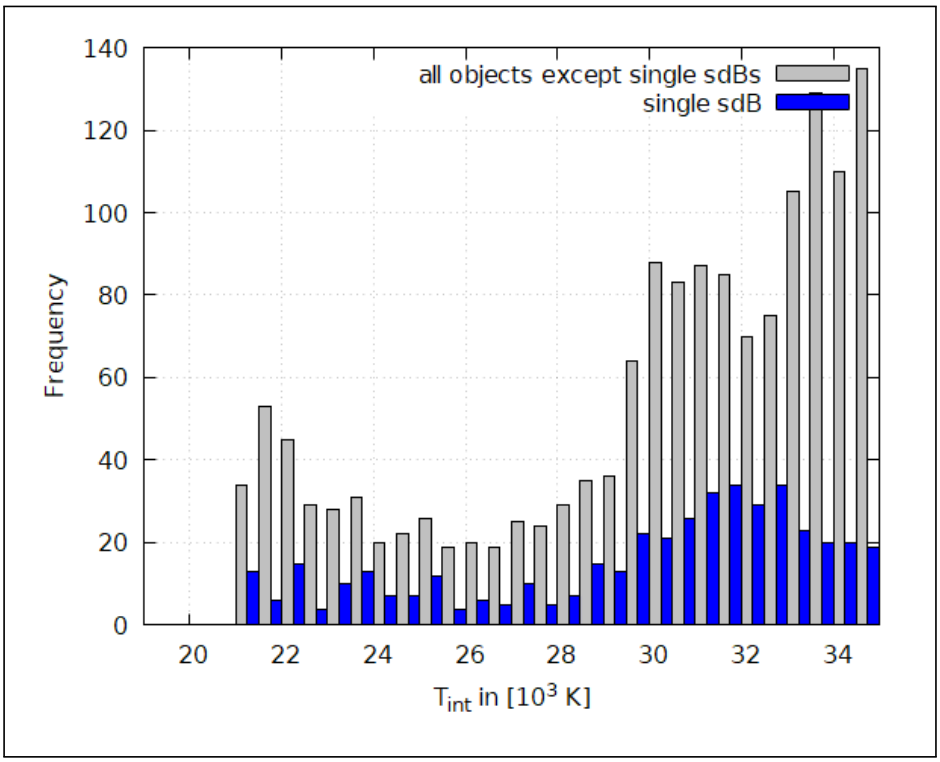

Figure 42: Histogram of subdwarf B stars (blue) and all other objects except of sources with spectroscopic class "sdB" (grey). (Image replaced)

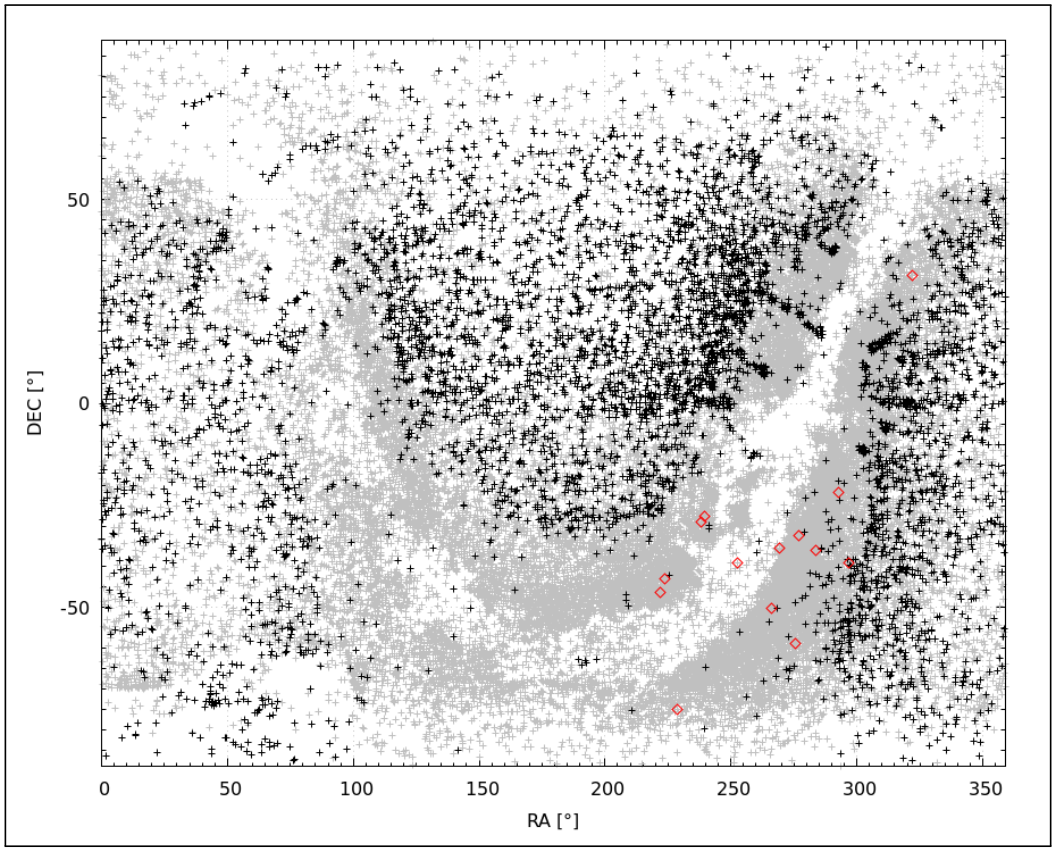

Figure 43: Coordinates of the small sample (black), the big sample (grey) and the selected subset (red). The empty band represents the Galactic disk.

Gaia DR2 1853416896629422464 If searched on SIMBAD via right ascension and declination an object from LAMOST survey is returned. LAMOST J212728.98+311841.1 was already investigated by Luo et al. (2019) which state that this star shows a strong double-lined composite spectrum with MgI triplet lines at 5170 $\AA$ and Calcium II triplet lines at 8650 $\AA$. This is usually an indication of a late type companion. By constructing a SED we see a color excess in the infrared and receive temperatures of $T_{eff} = 28700^{+2900}_{-1700}$ for the subdwarf and $T_{eff} = 4660^{+240}_{-130}$ for the companion. By assuming the presence of the MgI triplet the surface temperature of the cool companion is slightly underrated. But the surface ratio of $17.6^{+5.0}_{-2.2}$ is in the expected range. If we look at the GALEX image (s. Fig. 45) some elongation appears which can indicate a binary system. The 2MASS image (Fig. 46) also show that there is some flux in the infrared. So, there are strong evidences that Gaia DR2 1853416896629422464 is not a single star.

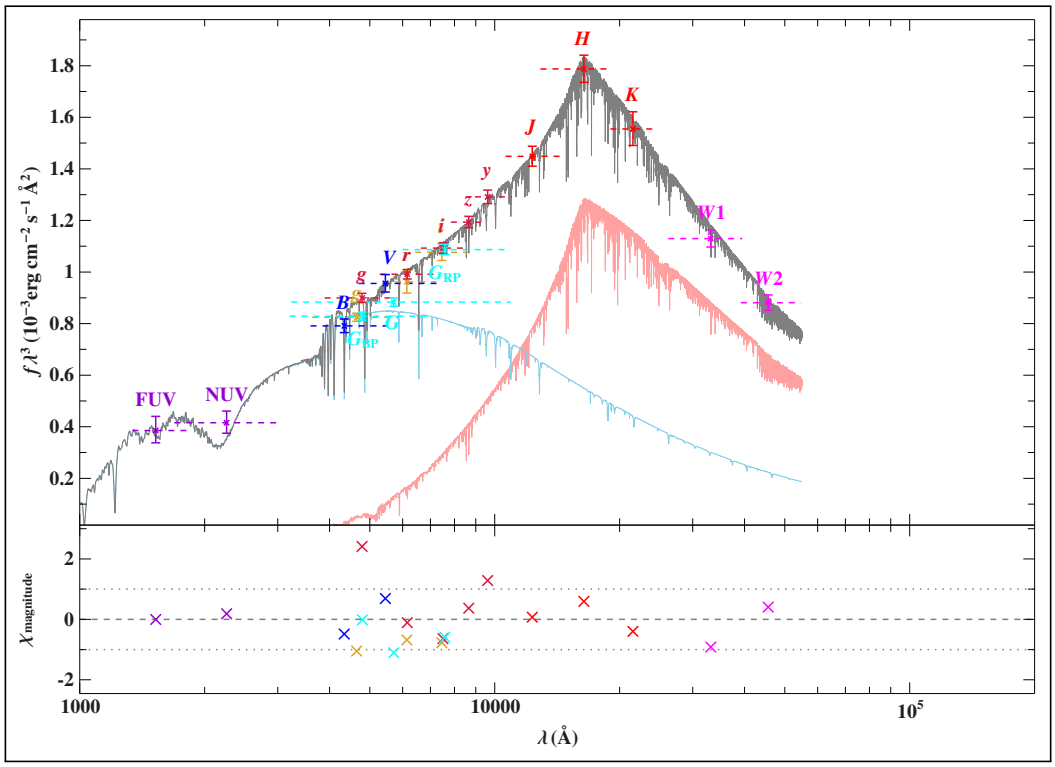

Figure 44: Gaia DR2 1853416896629422464; Top: Spectral Energy Distribution grey: combined, light-blue: subdwarf B, red: Cool companion. Bottom: Deviation of the photometric data from the actual SED in $[mag]$. The x-axis is the wavelength given in $[\AA]$.

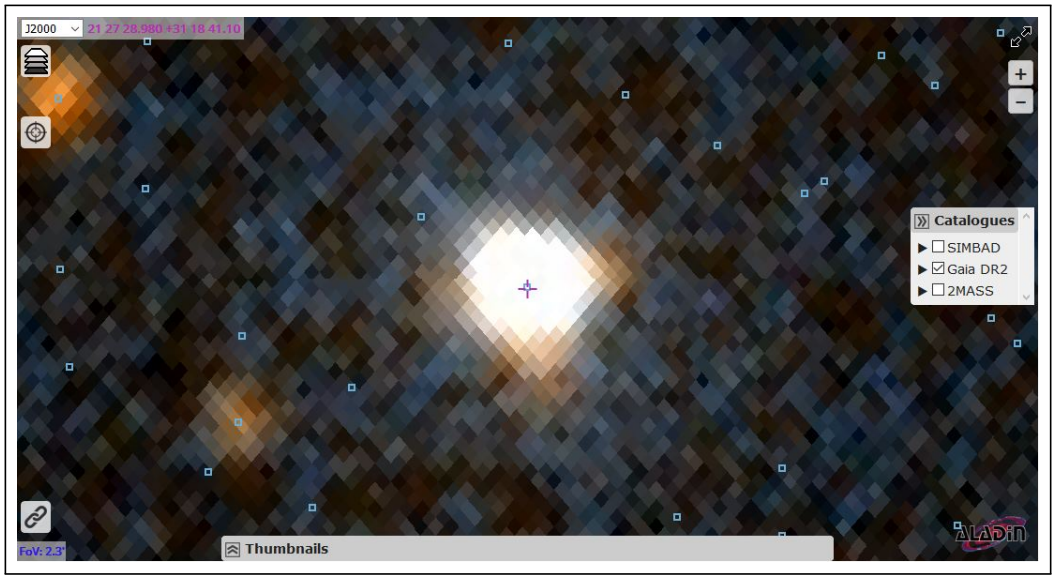

Figure 45: GALEX image (coordinates: 21 27 28.980 +31 18 41.10) of Gaia DR2 1853416896629422464 with a field of view (FoV) 2.3 arcminutes. . (Image taken from:`http://aladin.unistra.fr/AladinLite/?target=21%2027%2028.980%2B31%2018%2041.10&fov=0.04&survey=P%2FGALEXGR6%2FAIS%2Fcolor`)

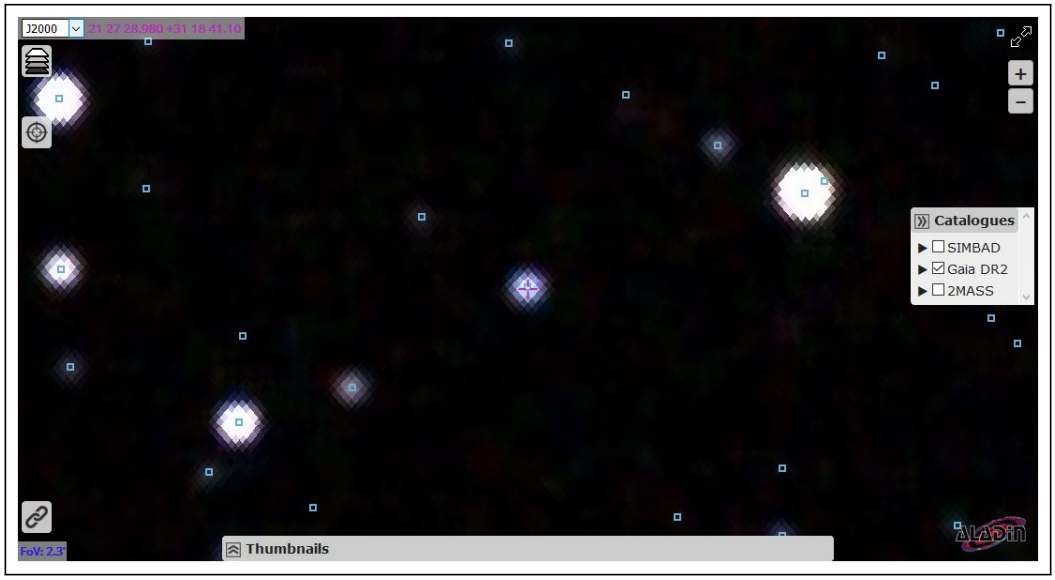

Figure 46: 2MASS image (coordinates: 21 27 28.980 +31 18 41.10) of Gaia DR2 1853416896629422464 with a field of view (FoV) 2.3 arcminutes. . (Image taken from:`http://aladin.unistra.fr/AladinLite/?target=21%2027%2028.980%2B31%2018%2041.10&fov=0.04&survey=P%2F2MASS%2Fcolor`)

Gaia DR2 5970804092555644800 With a right ascension $RA = 252.645243[^\circ]$ and declination $DEC = -38.969347[^\circ]$ this object resides in the Galactic plane. The contamination with other sources in this region relatively high. Although Geier et al. (2019) applied crowded region cleaning by checking the consistency of the Gaia bands with an isolated source and many more constraints it can not be avoided to have some unwanted objects in the sample. The binary SED (s. Fig. 47) shows that a binary containing a subdwarf and a cool companion is rather unlikely. The contribution of the second component is too low to be significant. Moreover, the subdwarf fit is quite poor and the narrow band filters g- and r-SkyMapper as well as the broad band filters B (Johnson), V (Johnson), G (Gaia) and G_{BP} (Gaia) were classified as outliers. This leads to the assumption that the object Gaia DR2 5970804092555644800 is neither a binary system nor a single subdwarf star.

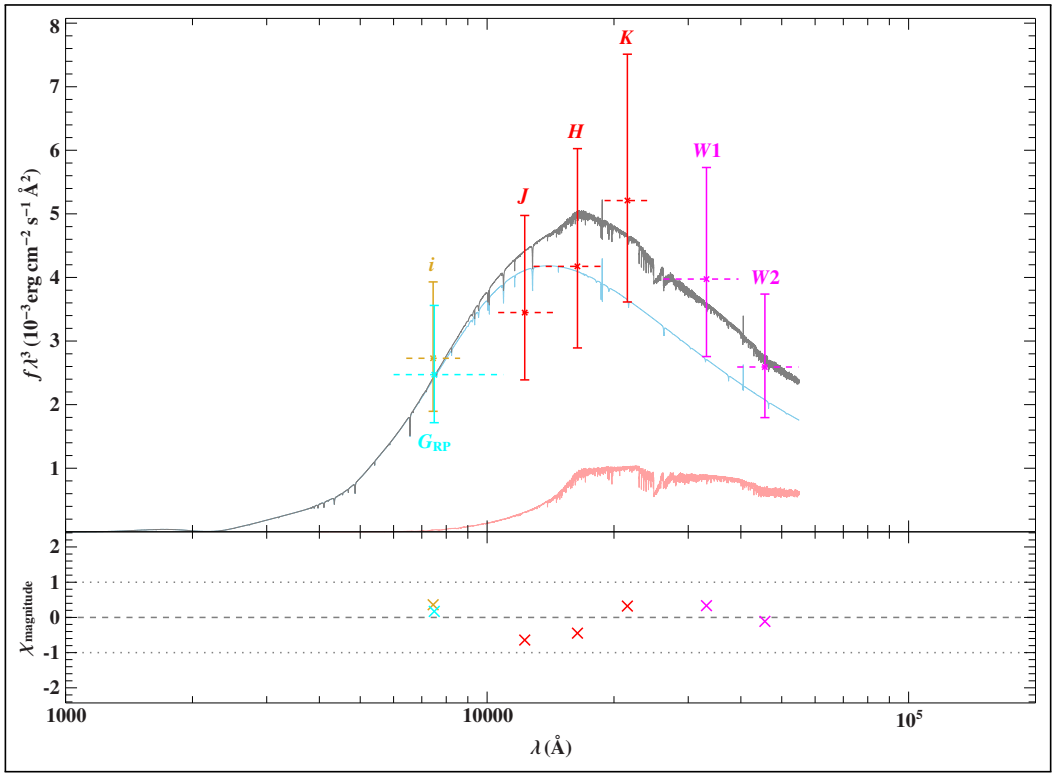

Figure 47: Gaia DR2 5970804092555644800; Top: Spectral Energy Distribution grey: combined, light-blue: subdwarf B, red: Cool companion. Bottom: Deviation of the photometric data from the actual SED in $[mag]$. The x-axis is the wavelength given in $[\AA]$.

Gaia DR2 6043056751129272704 The binary SED of this object is pretty convincing. Narrow band filter around the Balmer jump are provided and every wavelength regime, except of GALEX and WISE bandpasses, is very well covered. A clearly visible infrared excess, a usual color excess $E(B-V)$ and proper derived parameters for the surface ratio and effective temperatures make the binary system assumption plausible. With a temperature of $T_{eff} = 5680^{+220}_{-170}$ K the cooler star could be a late type F- or an early type G-star. The subdwarf component has a surface temperature of $T_{eff} = 30000^{+6000}_{-4000}$ K which is an argument for a sdB or sdOB.

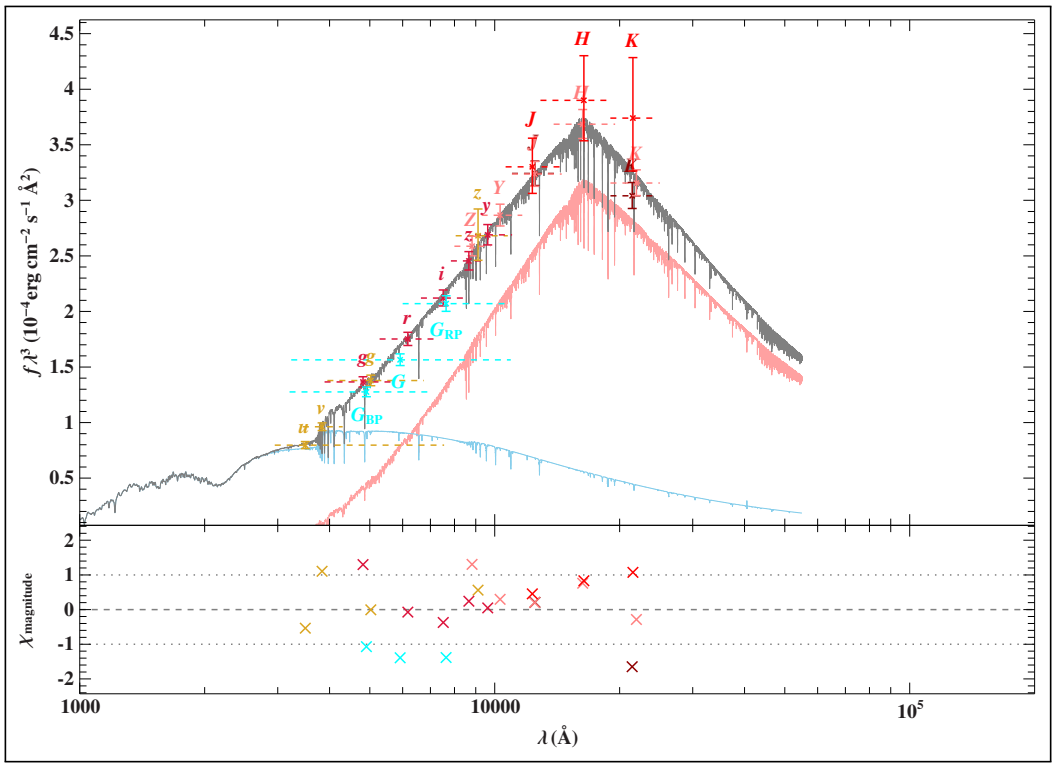

Figure 48: Gaia DR2 6043056751129272704; Top: Spectral Energy Distribution grey: combined, light-blue: subdwarf B, red: Cool companion. Bottom: Deviation of the photometric data from the actual SED in $[mag]$. The x-axis is the wavelength given in $[\AA]$.

Gaia DR2 6772863533995601664 Data from far-UV up to mid-IR are available. The GALEX FUV- and NUV-filter do not match perfectly. Since the mean extinction value from Schlafly & Finkbeiner (2011) and Schlegel et al. (1998) are taken as a fix value in the fit this can cause the deviation. By adjusting the extinction within both values, the derived parameters do not change significantly. The fit gives the temperatures $T_{eff} = 25800^{+1400}_{-1300}$ K for the subdwarf component and $T_{eff} = 5280^{+100}_{-70}$ K for the cool companion. The cool companion out of this fit can be a main-sequence G-star. Due to the radius of a subdwarf B star which thought to be between $0.15 < R_{sun} < 0.25$ and the radius of the G-star with roughly one solar mass the surface ratio (SR) is expected to lay in between $16 < SR < 44$. For this star we receive $SR = 32^{+5}_{-4}$. To sum up, there are many evidences that the Gaia source 6772863533995601664 is a binary system with a subdwarf and a main-sequence component.

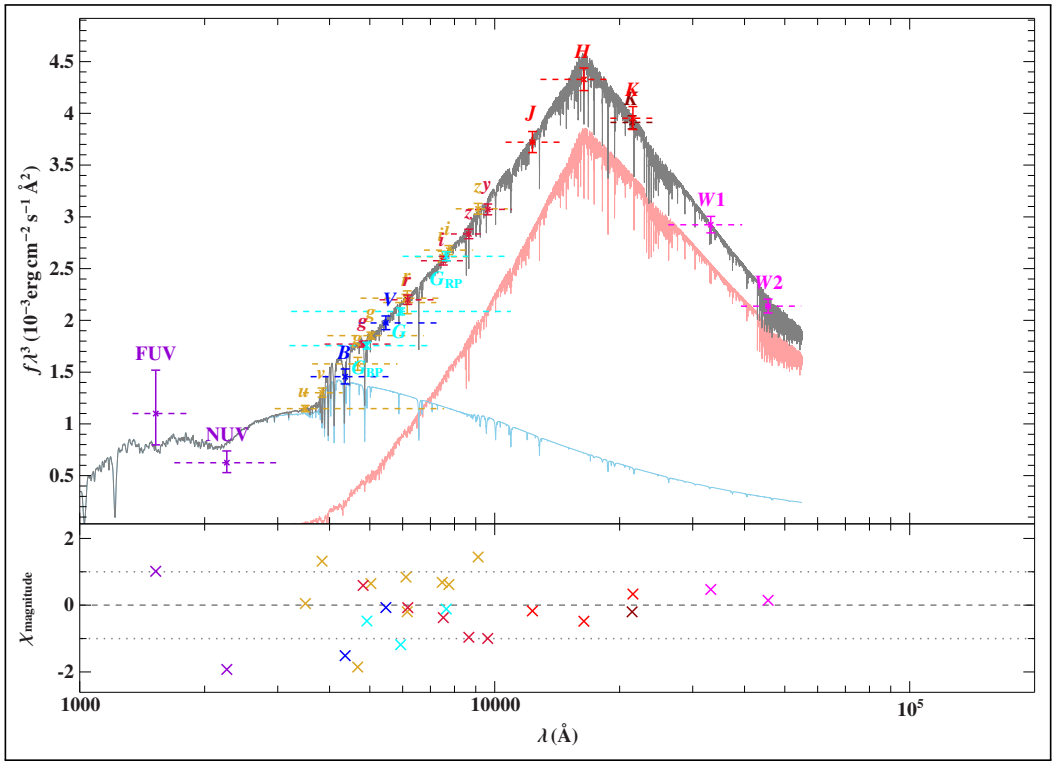

Figure 49: Gaia DR2 6772863533995601664; Top: Spectral Energy Distribution grey: combined, light-blue: subdwarf B, red: Cool companion. Bottom: Deviation of the photometric data from the actual SED in $[mag]$. The x-axis is the wavelength given in $[Å]$.

Identifier	RA [°]	DEC [°]	$E(B-V)^{[1]}$	$E(B-V)^{[2]}$	$E(B-V)^{[3]}$	Surface ratio	T_{eff} comp1 [K]	T_{eff} comp2 [K]	
Gaia DR2 1853416896629422464	321.87077	31.311457	0.1703	0.2071	$(0.0796-0.1680)^{+0.02}_{-0.02}$	$17.6^{+5.0}_{-2.2}$	28700^{+2900}_{-1700}	4660^{+240}_{-130}	1
Gaia DR2 4040547181688100736	269.4582	-35.470877	0.4368	0.5223	-	74^{+23}_{-26}	53000^{+2000}_{-20700}	2900^{+230}_{-130}	0
Gaia DR2 4045227974442377472	277.170766	-32.510409	0.1623	0.1952	-	28^{+15}_{-9}	30000^{+7000}_{-5000}	5370^{+260}_{-270}	1
Gaia DR2 5792639748086292736	228.758032	-74.880678	0.1184	0.1445	-	100^{+0}_{-27}	50200^{+1900}_{-10800}	5070^{+60}_{-50}	0
Gaia DR2 5906348045176103424	221.687424	-46.341726	0.1458	0.1784	-	100^{+0}_{-26}	38500^{+1400}_{-6000}	4750^{+70}_{-60}	0
Gaia DR2 5946601372041301504	266.11089	-50.1077	0.1190	0.1419	-	58^{+15}_{-11}	33400^{+4500}_{-2600}	4840^{+100}_{-110}	1
Gaia DR2 5970804092555644800	252.645243	-38.969347	0.8648	1.0774	-	6^{+48}_{-6}	55000^{+0}_{-41166}	3600^{+11400}_{-1300}	-1
Gaia DR2 6040945070328432768	238.025047	-29.031882	0.1274	0.1519	-	$77.0^{+1.7}_{-8.4}$	55000^{+0}_{-5737}	5750^{+60}_{-60}	0
Gaia DR2 6043056751129272704	239.421106	-27.586131	0.1516	0.1787	-	40^{+20}_{-12}	30000^{+6000}_{-4000}	5680^{+220}_{-170}	1
Gaia DR2 6100701942446586368	223.64173	-43.066083	0.1368	0.1645	-	60^{+5}_{-30}	55000^{+0}_{-26469}	4820^{+120}_{-190}	0
Gaia DR2 6635878236451584000	275.388911	-58.893779	0.0781	0.0945	-	$15.3^{+2.8}_{-2.3}$	21500^{+1700}_{-1600}	4160^{+230}_{-290}	1
Gaia DR2 6691344062581573504	296.811644	-38.977127	0.0755	0.0913	-	$21.0^{+2.7}_{-2.3}$	14900^{+700}_{-600}	4630^{+130}_{-120}	1
Gaia DR2 6731157309913205504	283.71513	-36.074927	0.0868	0.1052	-	100^{+0}_{-38}	32700^{+1300}_{-5000}	5350^{+270}_{-500}	0
Gaia DR2 6772863533995601664	292.755262	-21.691685	0.0813	0.0997	-	32^{+5}_{-4}	25800^{+1400}_{-1300}	5280^{+100}_{-70}	1

Table 10: Reddening values for 14 stars sample. The color excess E(B-V) is provided by two external sources ([1]=Schlafly & Finkbeiner (2011); [2]=Schlegel et al. (1998); [3]=Green (2019)) and by the SED fit. The flag value: (1)=likely binary system, (0)=not enough data to evaluate, (-1)=unlikely binary system.

7 Conclusion

Hot subluminous stars are already in a late evolutionary stage of stellar evolution and create their luminosity by thermonuclear fusion of helium. The formation of subdwarfs is not fully understood yet. But close binary systems are preferred. With spectroscopic investigations these systems can be identified by looking at specific absorption lines. Moreover, spectroscopy provides very reliable atmospheric parameters. But the analysis is time-consuming and therefore only 924 of 5'613 objects in the first catalog of Geier et al. (2017) have atmospheric parameter provided. With photometry the objects can be easily characterized even if it is mainly restricted to effective temperature, reddening and binarity. The Gaia space mission led to a new catalog of hot compact objects (Geier et al., 2019) with roughly 40'000 objects. The contamination with other sources like HBB stars, white dwarfs and many more is probably high, hence this is a huge challenge to characterize these sources. Gaia provides photometric data for every source but a photometric analyses need Color-Color diagrams. Gaia *G*-band is too broad for useful investigations on subdwarfs whereas the blue band G_{BP} and the red band G_{RP} can be used in combination with other colors. Furthermore, the infrared region is not covered by Gaia and so a variety of other photometric systems from UV to IR (GALEX, Johnson, Stroemgren, SDSS, SkyMapper, 2MASS, UKIDSS, ...) can be combined with Gaia filters to get promising results. Unfortunately, the databases of the other systems are not as extensive as Gaia. A priori it is not clear which color combinations are proper. The main goal is the photometric characterization of candidates as single stars as well as binaries. The problem hereby is the reddening vs. binarity. For single stars reddening free indexes are good whereas for binaries Color-Color diagrams with low dependance on the reddening and even better SED fits are suitable. For single stars the colors of SDSS filters (u-g) vs. (g-r) are appropriate since these filters are well calibrated, they are sensitive to temperature and a lot of data for the northern hemisphere are available. The southern counterpart is the survey SkyMapper but it goes not as deep as SDSS yet. For the binary search it is important to have J-, H- and K-bands provided. The problem is that subdwarfs are rather faint in the IR region and most surveys are not sensitive enough to resolve them. That's why the amount of data in IR is relatively low and the importance of spectral energy distributions (SED) comes into account. In this work it has been shown that the one-dimensional linear interpolation might support spectroscopically determined temperatures between 25'000 - 35'000 K but for lower and higher values the errors mainly exceed ± 5'000 K. But since every interpolation shows the same trend the temperatures could be corrected by a linear function. The distribution within the temperature histogram is as expected

for hot subdwarfs. In this way, an amount of 2'359 single hot subdwarf candidates were found. The search for binary systems was based on Color-Color diagrams and SED fits. From over a hundred combinations roughly a dozen remained for the binary search. Broad band filters in the visual wavelength range in combination with infrared and mid-IR passbands suit best due to the easy filtering procedure and reliability. The small sample containing 5'613 objects were firstly filtered upon the spectroscopic class "sdB" with known temperature and surface gravity. After applying a threshold for infrared colors 36 objects were left. Approximately 80 % (28 out of 36) seem to be binary systems, 6 objects have not enough data provided to make a clear statement and 2 out of 36 are most likely not binaries. The high amount of objects with probably two stars is reasonable since the search is designed to find these. Most of the found companions are F- to K-stars, whose high occurence can be explained by the very efficient Roche-lobe overflow. (Girven et al., 2012) The big sample (39'800 objects) has been investigated afterwards. The same filtering as for the small sample was applied. Remaining objects were further selected until only 14 possible binary candidates were left. Most of the sources are close to the Galactic plane which is another challenge in the analysis. Due to this and the different selection criteria compared to Geier et al. (2017) first hot compact object catalog, the contamination of late B-type (HBB), hot post-AGB stars and white dwarfs is higher. From the 14 binary candidates 50 % show strong evidence to be real binary systems containing a subdwarf component and a cool companion. Furter $\approx$ 43 % show features of a binary system but not enough photometric data are available or parameters run against the borders. The remaining object is most likely not a system of a subdwarf and a cool companion. This work has shown that appropriate Color-Color combinations are very promising to identify binary systems with neither knowing the distance to the object nor spectroscopic determined parameters. Gaia will provide photometry in 30 optical channels in a later release and the VISTA Hemisphere Survey (VHS) will deliver infrared photometry for the whole southern sky. This opens the possibility to analyse way more candidates by combining the photometry.

Acknowledgement

General acknowledgement

I would like to pay my special regards to my supervisor Prof. Uli Heber for the chance to write again my thesis at the Remeis-Observatory. I want to thank him also for this interesting topic and all the support even besides thesis relevant issues. I wish to express my deepest gratitude to Prof. Uli Katz whose support in organizational questions made this work possible. I want to thank my colleagues Dr. Andreas Irrgang, Simon Kreuzer, David Schneider and Matti Dorsch for answering all of my questions and technical support during my thesis. I wish to acknowledge the support and great love of my mother, Sven, Ralf, Marc, Nadja and Marjan. They kept me going on and this work would not have been possible without their input. And I want to thank Shikamaru Nara for always reminding me to take my time to think and be patient.

Data usage

UKIDSS This work is based in part on data obtained as part of the UKIRT Infrared Deep Sky Survey.

2MASS This publication makes use of data products from the Two Micron All Sky Survey, which is a joint project of the University of Massachusetts and the Infrared Processing and Analysis Center/California Institute of Technology, funded by the National Aeronautics and Space Administration and the National Science Foundation.

Gaia Based on data products from observations made with ESO Telescopes at the La Silla Paranal Observatory under programme ID 188.B-3002. These data products have been processed by the Cambridge Astronomy Survey Unit (CASU) at the Institute of Astronomy, University of Cambridge, and by the FLAMES/UVES reduction team at INAF/Osservatorio Astrofisico di Arcetri. These data have been obtained from the Gaia-ESO Survey Data Archive, prepared and hosted by the Wide Field Astronomy Unit, Institute for Astronomy, University of Edinburgh, which is funded by the UK Science and Technology Facilities Council.

GALEX Based on observations made with the NASA Galaxy Evolution Explorer. GALEX is operated for NASA by the California Institute of Technology under NASA contract

NAS5-98034.

SDSS I & SDSS II Funding for the SDSS and SDSS-II has been provided by the Alfred P. Sloan Foundation, the Participating Institutions, the National Science Foundation, the U.S. Department of Energy, the National Aeronautics and Space Administration, the Japanese Monbukagakusho, the Max Planck Society, and the Higher Education Funding Council for England. The SDSS Web Site is http://www.sdss.org/. The SDSS is managed by the Astrophysical Research Consortium for the Participating Institutions. The Participating Institutions are the American Museum of Natural History, Astrophysical Institute Potsdam, University of Basel, University of Cambridge, Case Western Reserve University, University of Chicago, Drexel University, Fermilab, the Institute for Advanced Study, the Japan Participation Group, Johns Hopkins University, the Joint Institute for Nuclear Astrophysics, the Kavli Institute for Particle Astrophysics and Cosmology, the Korean Scientist Group, the Chinese Academy of Sciences (LAMOST), Los Alamos National Laboratory, the Max-Planck-Institute for Astronomy (MPIA), the Max-Planck-Institute for Astrophysics (MPA), New Mexico State University, Ohio State University, University of Pittsburgh, University of Portsmouth, Princeton University, the United States Naval Observatory, and the University of Washington.

SDSS III Funding for SDSS-III has been provided by the Alfred P. Sloan Foundation, the Participating Institutions, the National Science Foundation, and the U.S. Department of Energy Office of Science. The SDSS-III web site is http://www.sdss3.org/. SDSS-III is managed by the Astrophysical Research Consortium for the Participating Institutions of the SDSS-III Collaboration including the University of Arizona, the Brazilian Participation Group, Brookhaven National Laboratory, University of Cambridge, Carnegie Mellon University, University of Florida, the French Participation Group, the German Participation Group, Harvard University, the Instituto de Astrofisica de Canarias, the Michigan State/Notre Dame/JINA Participation Group, Johns Hopkins University, Lawrence Berkeley National Laboratory, Max Planck Institute for Astrophysics, Max Planck Institute for Extraterrestrial Physics, New Mexico State University, New York University, Ohio State University, Pennsylvania State University, University of Portsmouth, Princeton University, the Spanish Participation Group, University of Tokyo, University of Utah, Vanderbilt University, University of Virginia, University of Washington, and Yale University.

SDSS IV Funding for the Sloan Digital Sky Survey IV has been provided by the Alfred P. Sloan Foundation, the U.S. Department of Energy Office of Science, and the

Participating Institutions. SDSS-IV acknowledges support and resources from the Center for High-Performance Computing at the University of Utah. The SDSS web site is www.sdss.org. SDSS-IV is managed by the Astrophysical Research Consortium for the Participating Institutions of the SDSS Collaboration including the Brazilian Participation Group, the Carnegie Institution for Science, Carnegie Mellon University, the Chilean Participation Group, the French Participation Group, Harvard-Smithsonian Center for Astrophysics, Instituto de Astrofísica de Canarias, The Johns Hopkins University, Kavli Institute for the Physics and Mathematics of the Universe (IPMU) / University of Tokyo, Lawrence Berkeley National Laboratory, Leibniz Institut für Astrophysik Potsdam (AIP), Max-Planck-Institut für Astronomie (MPIA Heidelberg), Max-Planck-Institut für Astrophysik (MPA Garching), Max-Planck-Institut für Extraterrestrische Physik (MPE), National Astronomical Observatories of China, New Mexico State University, New York University, University of Notre Dame, Observatário Nacional / MCTI, The Ohio State University, Pennsylvania State University, Shanghai Astronomical Observatory, United Kingdom Participation Group, Universidad Nacional Autónoma de México, University of Arizona, University of Colorado Boulder, University of Oxford, University of Portsmouth, University of Utah, University of Virginia, University of Washington, University of Wisconsin, Vanderbilt University, and Yale University.

WISE This publication makes use of data products from the Wide-field Infrared Survey Explorer(Wright et al., 2010), which is a joint project of the University of California, Los Angeles, and the Jet Propulsion Laboratory/California Institute of Technology, funded by the National Aeronautics and Space Administration.

PanSTARRS The Pan-STARRS1 Surveys (PS1) have been made possible through contributions of the Institute for Astronomy, the University of Hawaii, the Pan-STARRS Project Office, the Max-Planck Society and its participating institutes, the Max Planck Institute for Astronomy, Heidelberg and the Max Planck Institute for Extraterrestrial Physics, Garching, The Johns Hopkins University, Durham University, the University of Edinburgh, Queen's University Belfast, the Harvard-Smithsonian Center for Astrophysics, the Las Cumbres Observatory Global Telescope Network Incorporated, the National Central University of Taiwan, the Space Telescope Science Institute, the National Aeronautics and Space Administration under Grant No. NNX08AR22G issued through the Planetary Science Division of the NASA Science Mission Directorate, the National Science Foundation under Grant No. AST-1238877, the University of Maryland, and Eotvos Lorand University (ELTE).

8 Appendix

In the following all binary SED fits are shown. Not all of them show characteristic features to be classified as a compound of two stars.

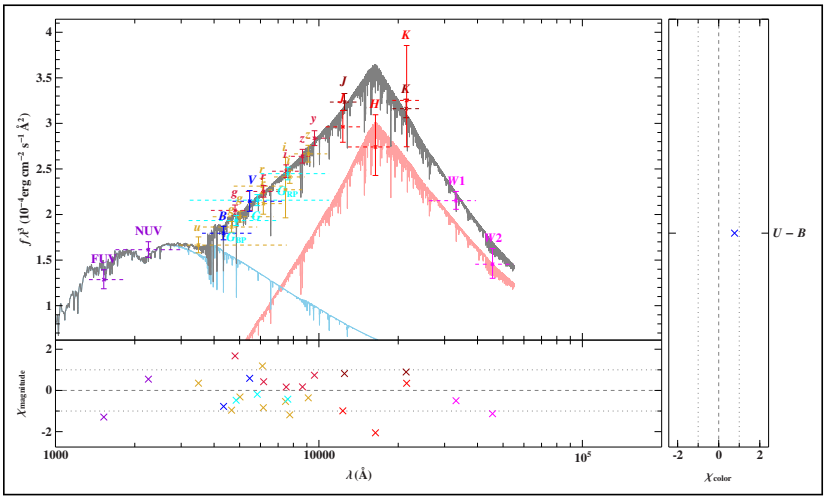

Figure 50: EC13527-1827; Top: Spectral Energy Distribution grey: combined, light-blue: subdwarf B, red: Cool companion. Bottom: Deviation of the photometric data from the actual SED in $[mag]$. The x-axis is the wavelength given in $[\AA]$.

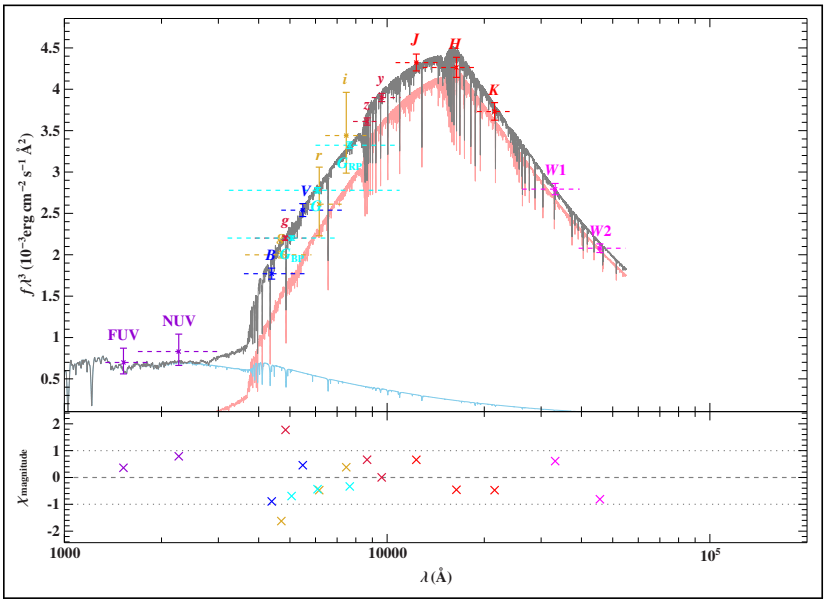

Figure 51: GALEX J02103+0830; Top: Spectral Energy Distribution grey: combined, light-blue: subdwarf B, red: Cool companion. Bottom: Deviation of the photometric data from the actual SED in $[mag]$. The x-axis is the wavelength given in $[\AA]$.

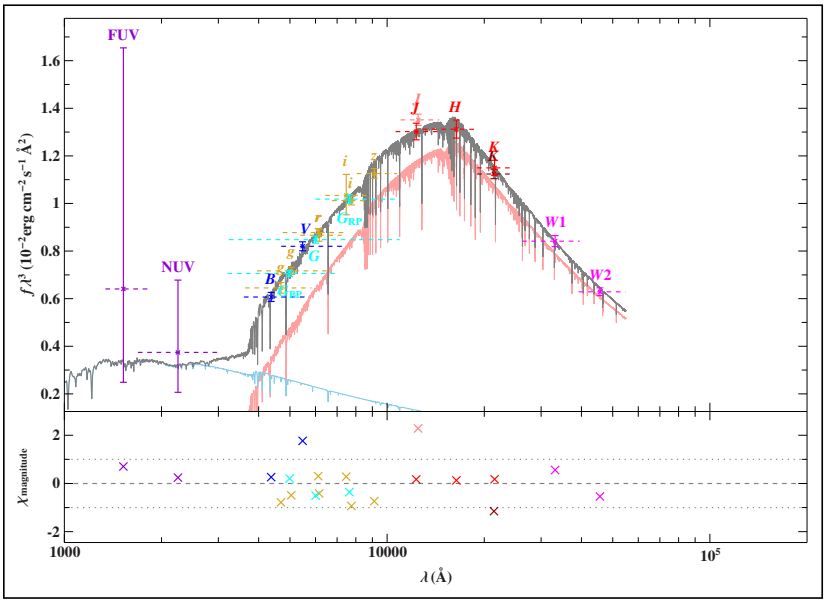

Figure 52: GALEX J022454.87+010938.81; Top: Spectral Energy Distribution grey: combined, light-blue: subdwarf B, red: Cool companion. Bottom: Deviation of the photometric data from the actual SED in $[mag]$. The x-axis is the wavelength given in $[\AA]$.

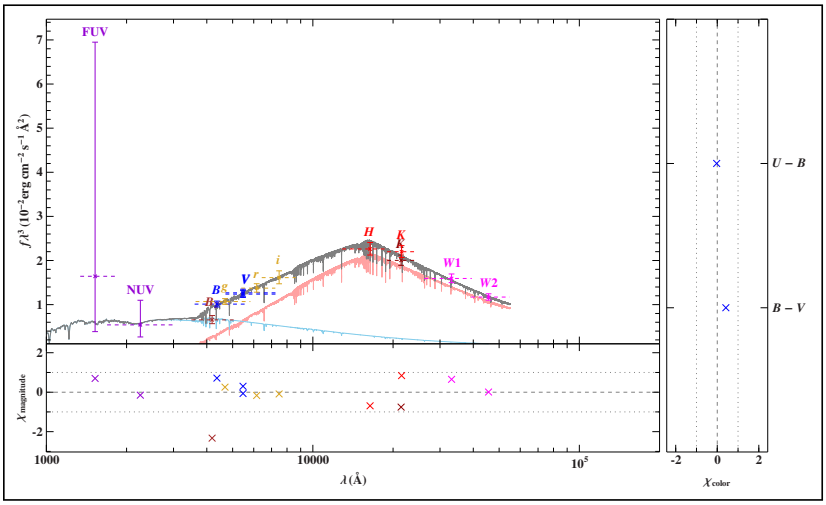

Figure 53: GALEX J05073-2802; Top: Spectral Energy Distribution grey: combined, light-blue: subdwarf B, red: Cool companion. Bottom: Deviation of the photometric data from the actual SED in $[mag]$. The x-axis is the wavelength given in $[\AA]$.

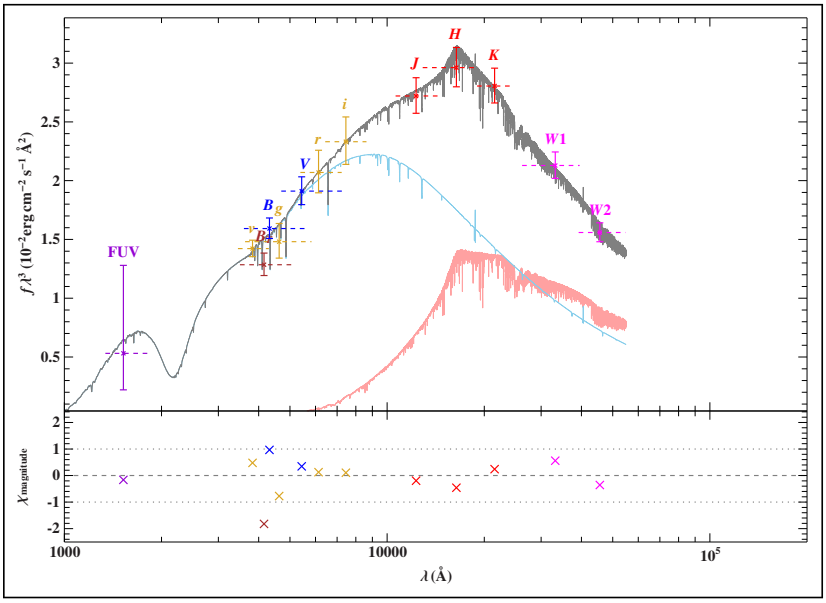

Figure 54: GALEX J065736.93-732449.60; Top: Spectral Energy Distribution grey: combined, light-blue: subdwarf B, red: Cool companion. Bottom: Deviation of the photometric data from the actual SED in $[mag]$. The x-axis is the wavelength given in $[\AA]$.

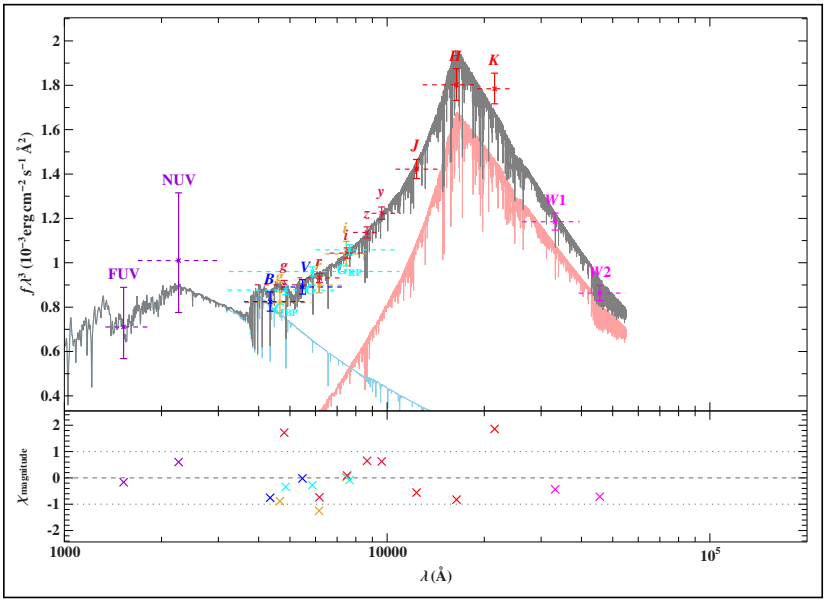

Figure 55: GALEX J08259+1307; Top: Spectral Energy Distribution grey: combined, light-blue: subdwarf B, red: Cool companion. Bottom: Deviation of the photometric data from the actual SED in $[mag]$. The x-axis is the wavelength given in $[\AA]$.

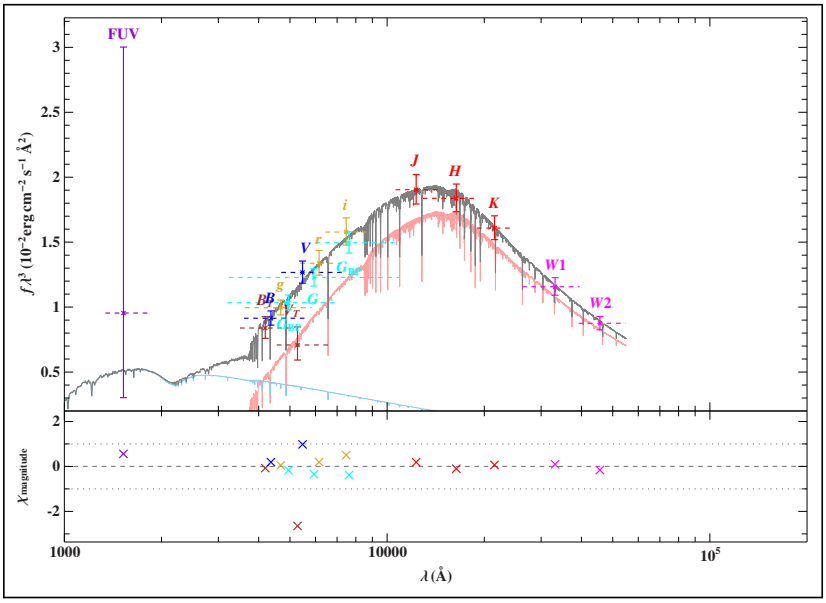

Figure 56: GALEX J10179+5516; Top: Spectral Energy Distribution grey: combined, light-blue: subdwarf B, red: Cool companion. Bottom: Deviation of the photometric data from the actual SED in $[mag]$. The x-axis is the wavelength given in $[\AA]$.

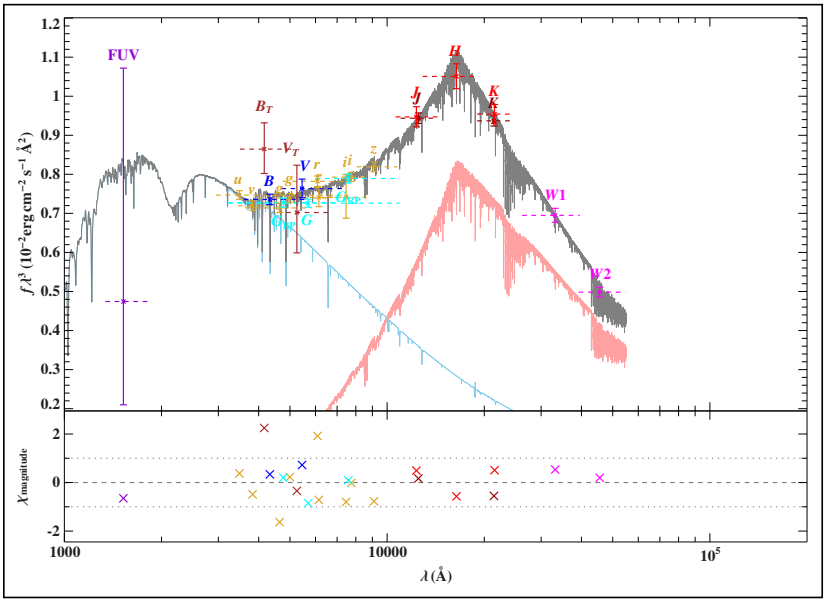

Figure 57: GALEX J13564-4934; Top: Spectral Energy Distribution grey: combined, light-blue: subdwarf B, red: Cool companion. Bottom: Deviation of the photometric data from the actual SED in $[mag]$. The x-axis is the wavelength given in $[\AA]$.

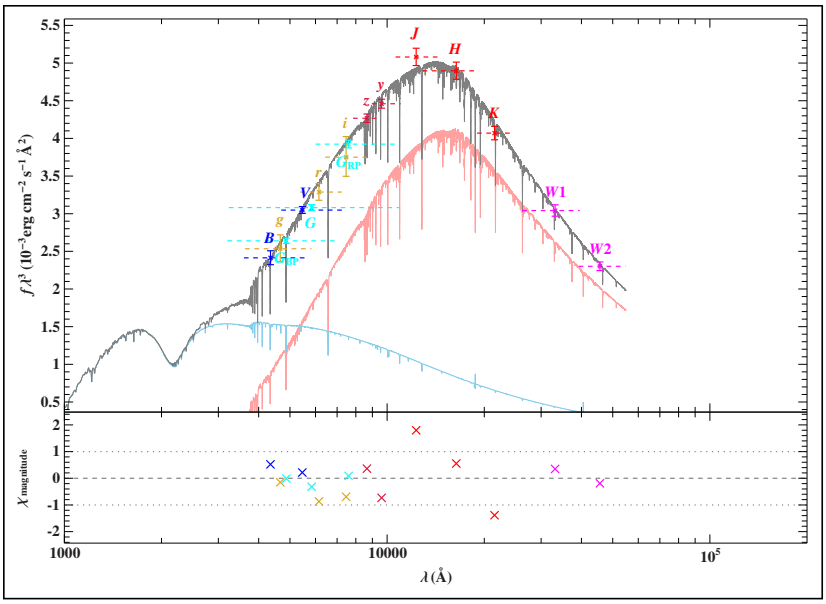

Figure 58: GALEX J16190+4831; Top: Spectral Energy Distribution grey: combined, light-blue: subdwarf B, red: Cool companion. Bottom: Deviation of the photometric data from the actual SED in $[mag]$. The x-axis is the wavelength given in $[\AA]$.

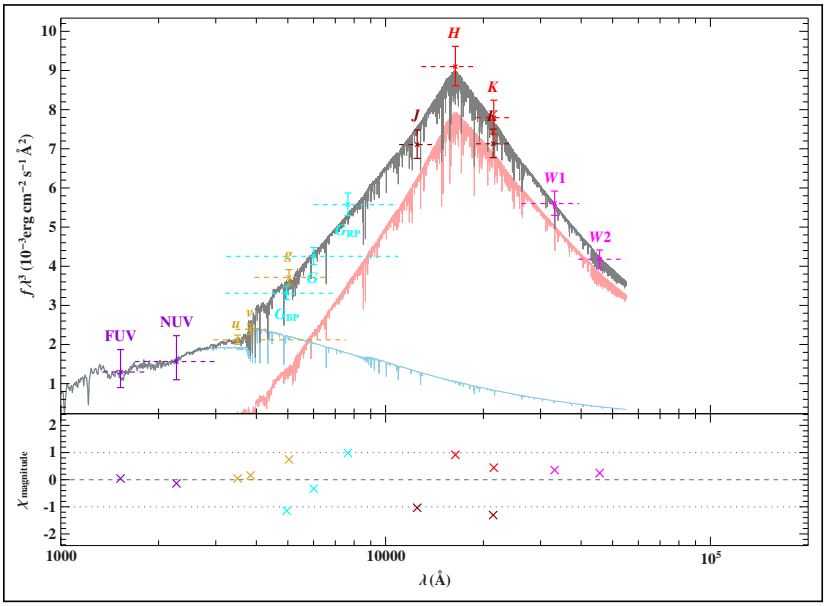

Figure 59: GALEX J175340.57-500741.80; Top: Spectral Energy Distribution grey: combined, light-blue: subdwarf B, red: Cool companion. Bottom: Deviation of the photometric data from the actual SED in $[mag]$. The x-axis is the wavelength given in $[\AA]$.

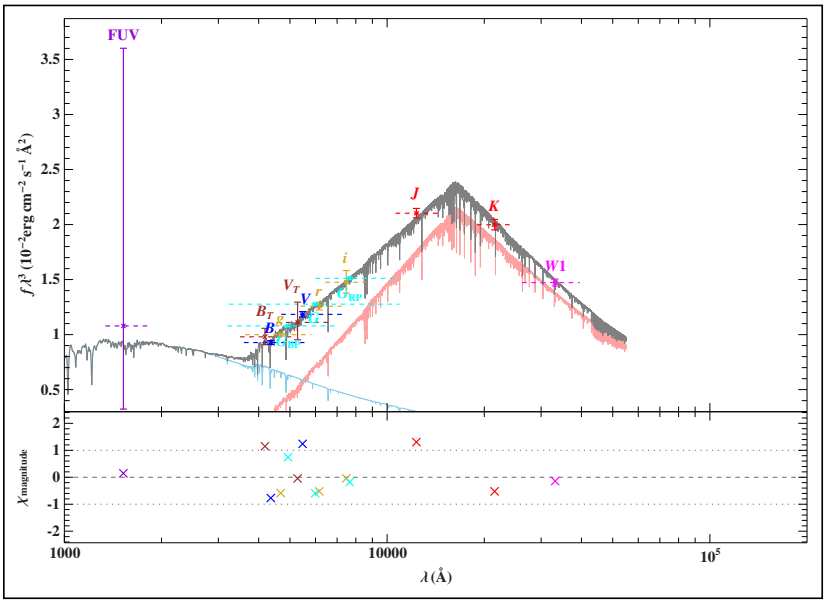

Figure 60: GALEX J20209-2250; Top: Spectral Energy Distribution grey: combined, light-blue: subdwarf B, red: Cool companion. Bottom: Deviation of the photometric data from the actual SED in $[mag]$. The x-axis is the wavelength given in $[\AA]$.

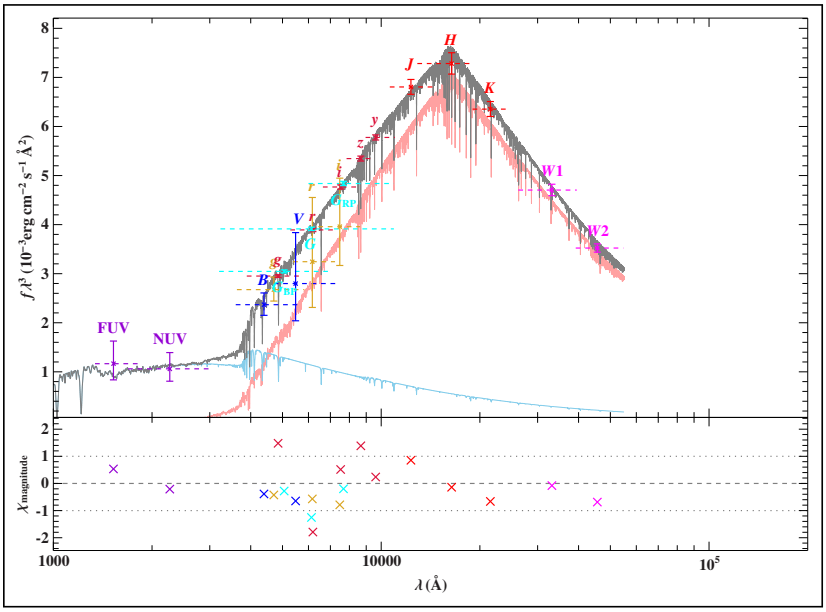

Figure 61: GALEX J20222+0152; Top: Spectral Energy Distribution grey: combined, light-blue: subdwarf B, red: Cool companion. Bottom: Deviation of the photometric data from the actual SED in $[mag]$. The x-axis is the wavelength given in $[\AA]$.

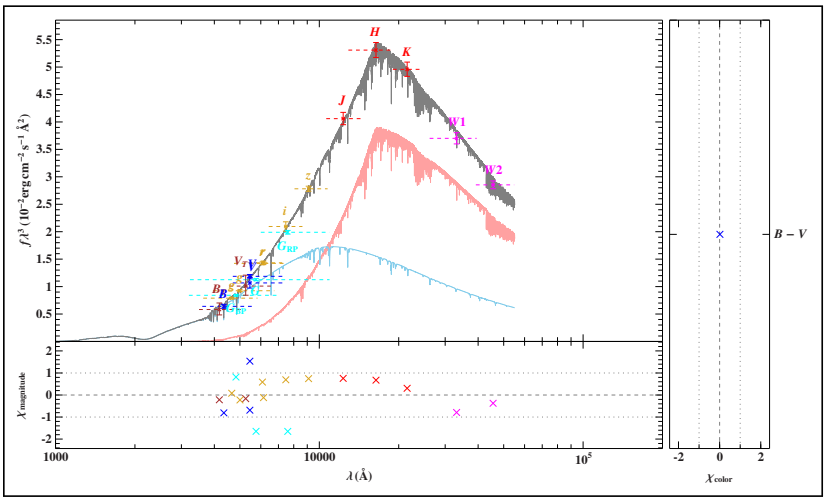

Figure 62: GALEX J203850.22-265747.16; Top: Spectral Energy Distribution grey: combined, light-blue: subdwarf B, red: Cool companion. Bottom: Deviation of the photometric data from the actual SED in $[mag]$. The x-axis is the wavelength given in $[\AA]$.

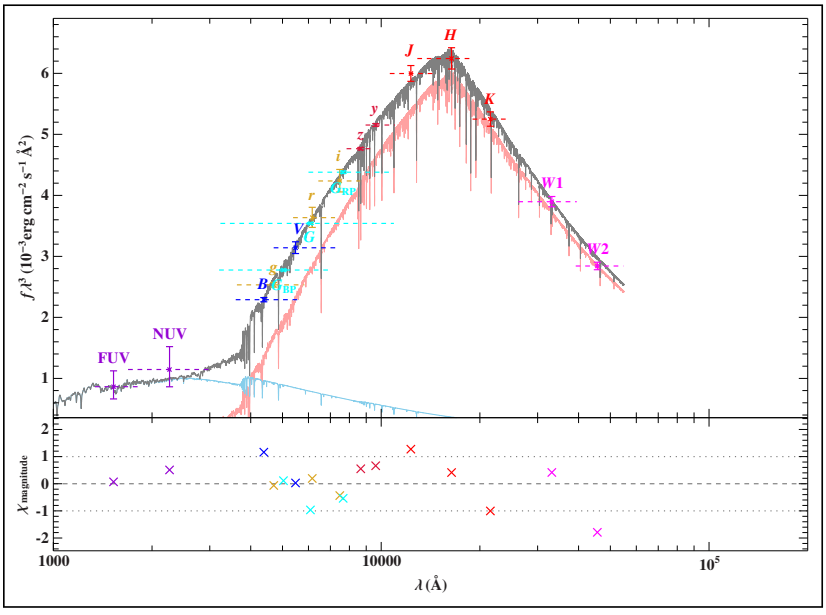

Figure 63: GALEX J21005+1452; Top: Spectral Energy Distribution grey: combined, light-blue: subdwarf B, red: Cool companion. Bottom: Deviation of the photometric data from the actual SED in $[mag]$. The x-axis is the wavelength given in $[\AA]$.

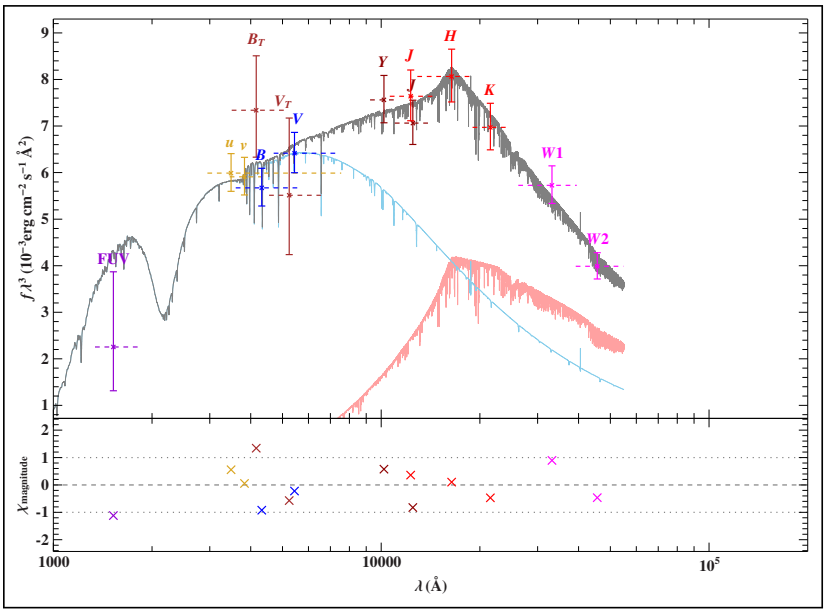

Figure 64: GALEX J211230.92-152410.37; Top: Spectral Energy Distribution grey: combined, light-blue: subdwarf B, red: Cool companion. Bottom: Deviation of the photometric data from the actual SED in $[mag]$. The x-axis is the wavelength given in $[\mathring{A}]$.

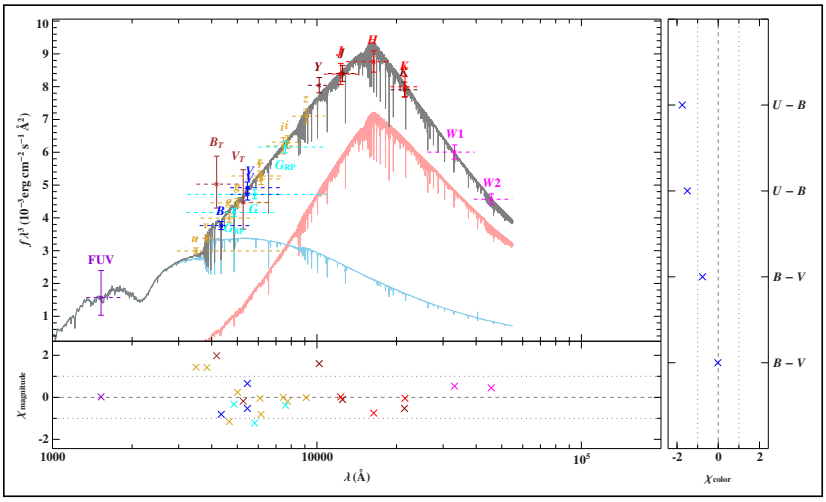

Figure 65: GALEX J214022.87-371414.05; Top: Spectral Energy Distribution grey: combined, light-blue: subdwarf B, red: Cool companion. Bottom: Deviation of the photometric data from the actual SED in $[mag]$. The x-axis is the wavelength given in $[\mathring{A}]$.

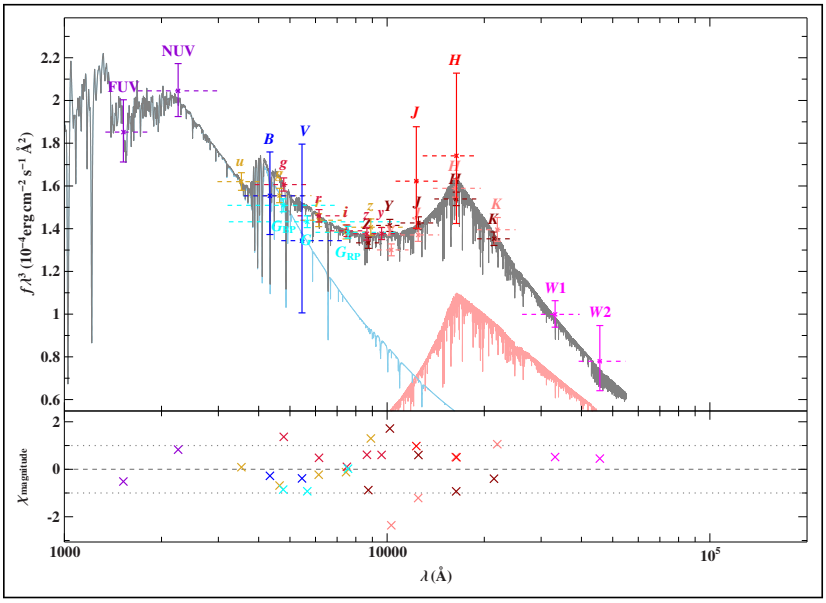

Figure 66: PG1258+012; Top: Spectral Energy Distribution grey: combined, light-blue: subdwarf B, red: Cool companion. Bottom: Deviation of the photometric data from the actual SED in $[mag]$. The x-axis is the wavelength given in $[\AA]$.

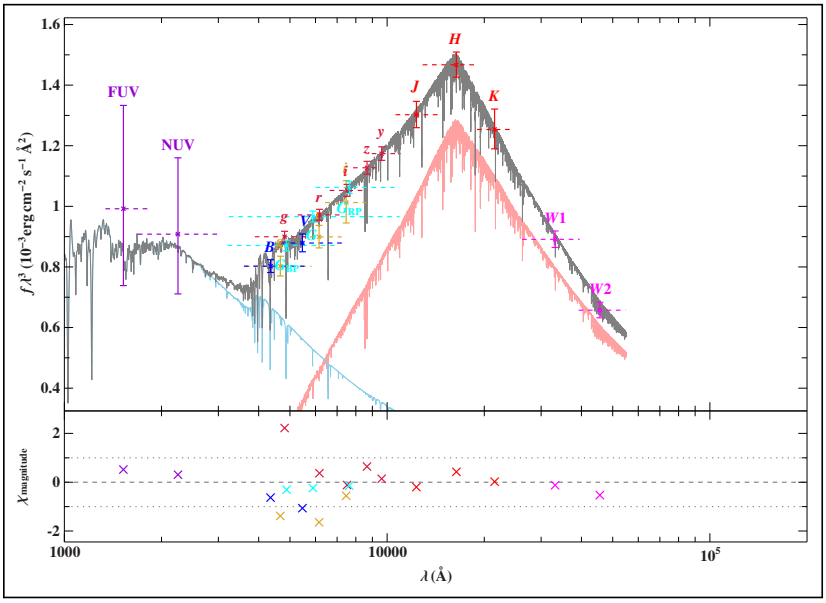

Figure 67: PG1559+076; Top: Spectral Energy Distribution grey: combined, light-blue: subdwarf B, red: Cool companion. Bottom: Deviation of the photometric data from the actual SED in $[mag]$. The x-axis is the wavelength given in $[\AA]$.

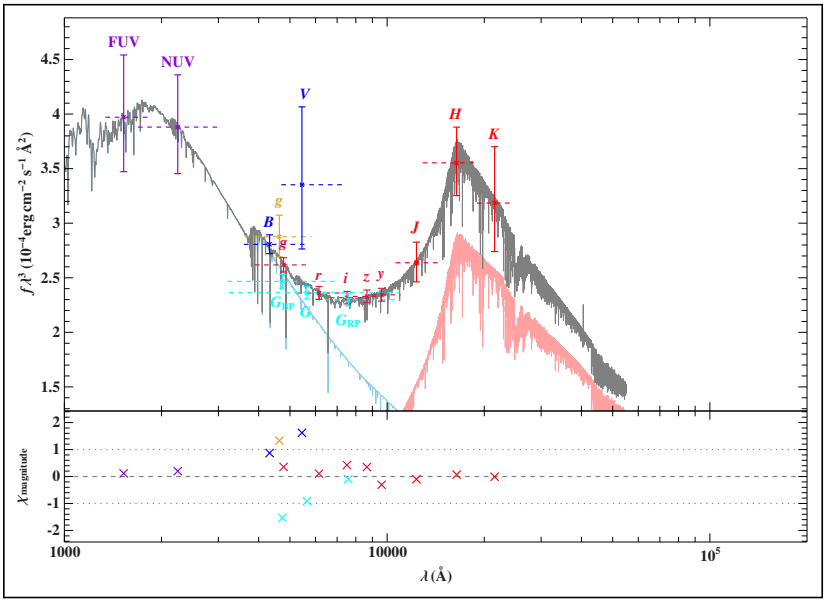

Figure 68: PG1623+386; Top: Spectral Energy Distribution grey: combined, light-blue: subdwarf B, red: Cool companion. Bottom: Deviation of the photometric data from the actual SED in $[mag]$. The x-axis is the wavelength given in $[\AA]$.

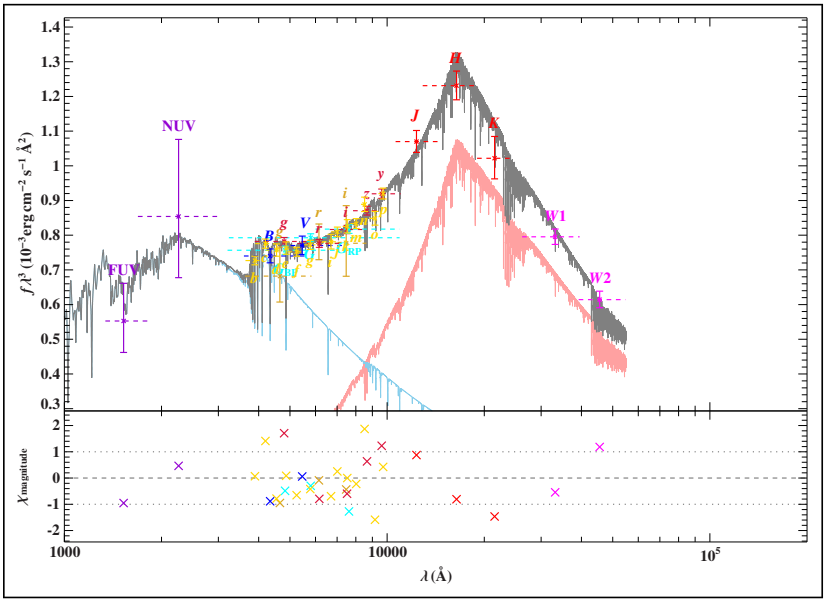

Figure 69: PG2223+171; Top: Spectral Energy Distribution grey: combined, light-blue: subdwarf B, red: Cool companion. Bottom: Deviation of the photometric data from the actual SED in $[mag]$. The x-axis is the wavelength given in $[\AA]$.

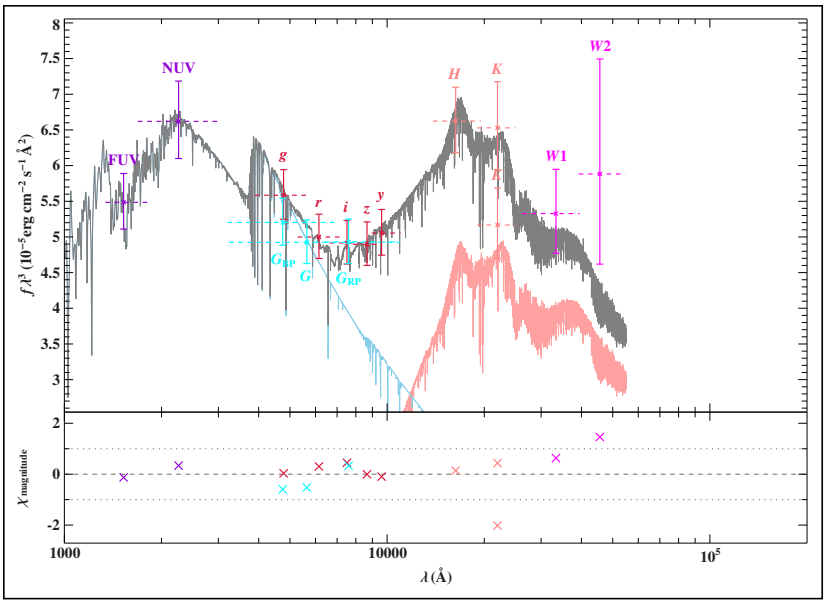

Figure 70: SDSSJ121514.66+284522.55; Top: Spectral Energy Distribution grey: combined, light-blue: subdwarf B, red: Cool companion. Bottom: Deviation of the photometric data from the actual SED in $[mag]$. The x-axis is the wavelength given in $[\mathring{A}]$.

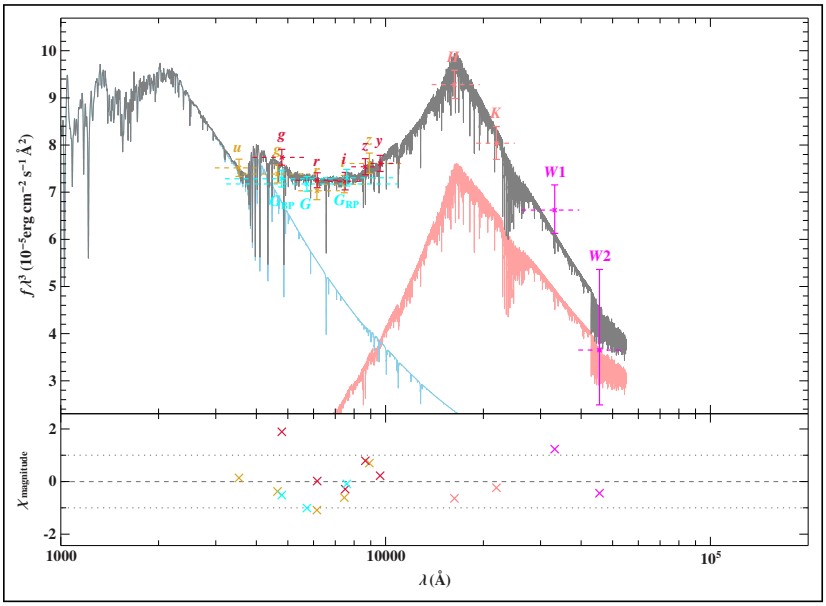

Figure 71: SDSSJ152705.03+110843.9; Top: Spectral Energy Distribution grey: combined, light-blue: subdwarf B, red: Cool companion. Bottom: Deviation of the photometric data from the actual SED in $[mag]$. The x-axis is the wavelength given in $[\mathring{A}]$.

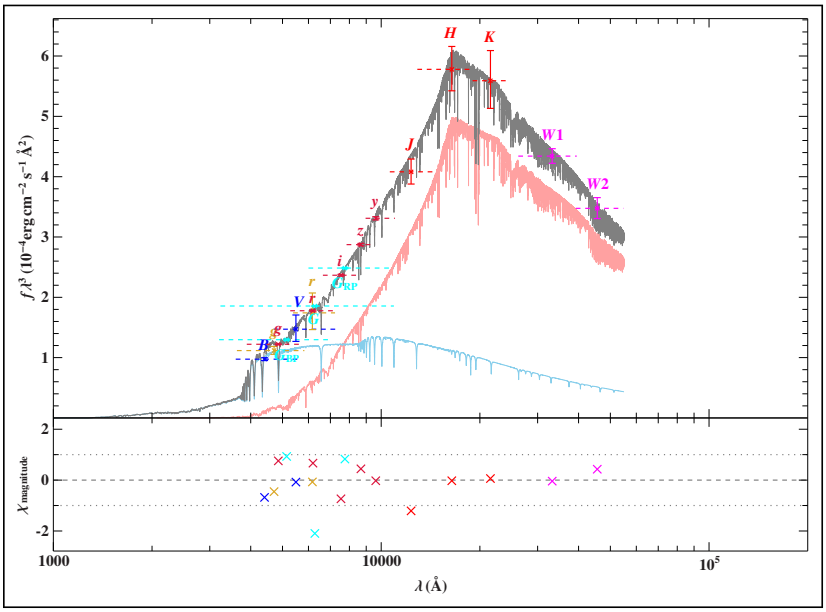

Figure 72: SDSSJ154923.48+163023.80; Top: Spectral Energy Distribution grey: combined, light-blue: subdwarf B, red: Cool companion. Bottom: Deviation of the photometric data from the actual SED in $[mag]$. The x-axis is the wavelength given in $[Å]$.

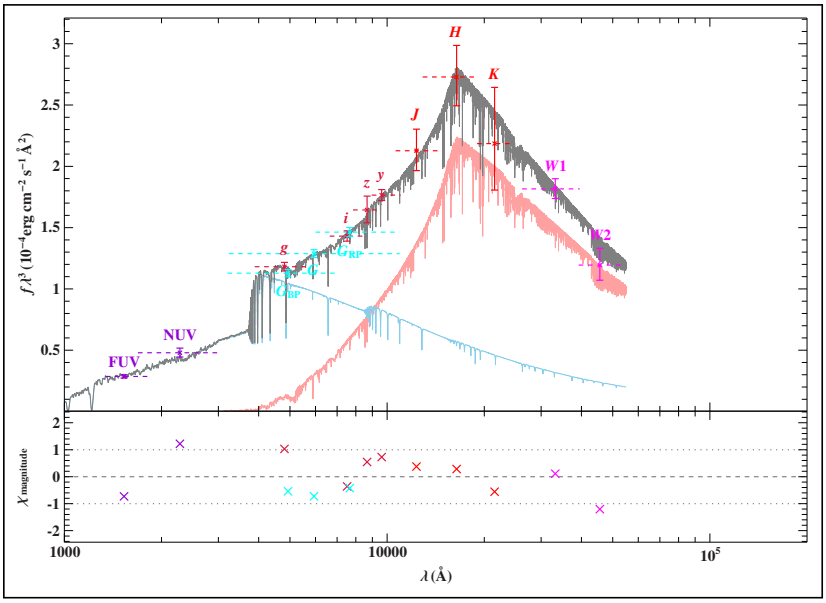

Figure 73: SDSSJ170716.53+275410.4; Top: Spectral Energy Distribution grey: combined, light-blue: subdwarf B, red: Cool companion. Bottom: Deviation of the photometric data from the actual SED in $[mag]$. The x-axis is the wavelength given in $[Å]$.

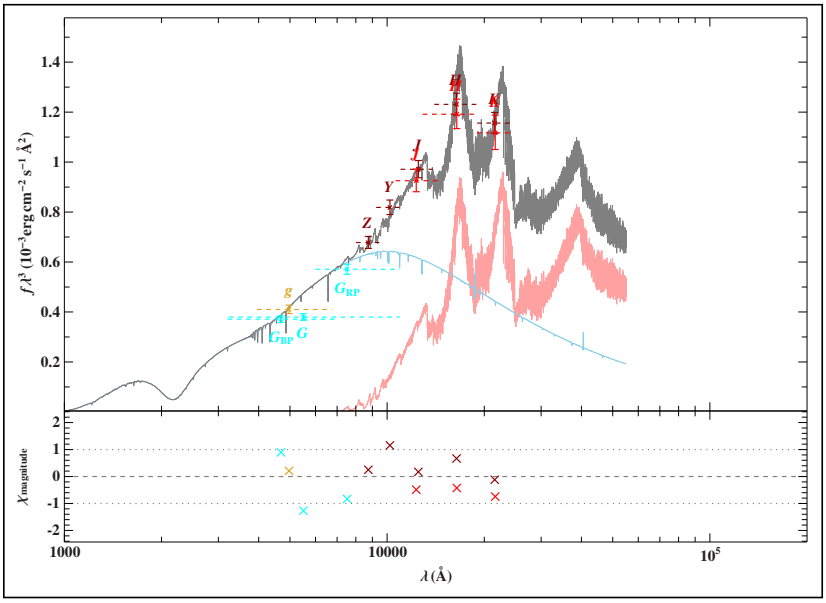

Figure 74: Gaia DR2 4040547181688100736; Top: Spectral Energy Distribution grey: combined, light-blue: subdwarf B, red: Cool companion. Bottom: Deviation of the photometric data from the actual SED in $[mag]$. The x-axis is the wavelength given in $[\AA]$.

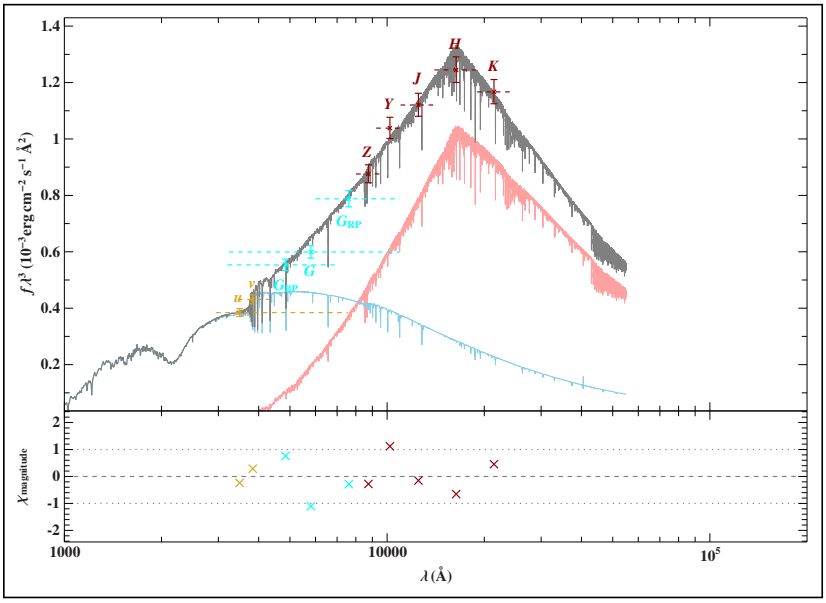

Figure 75: Gaia DR2 4045227974442377472; Top: Spectral Energy Distribution grey: combined, light-blue: subdwarf B, red: Cool companion. Bottom: Deviation of the photometric data from the actual SED in $[mag]$. The x-axis is the wavelength given in $[\AA]$.

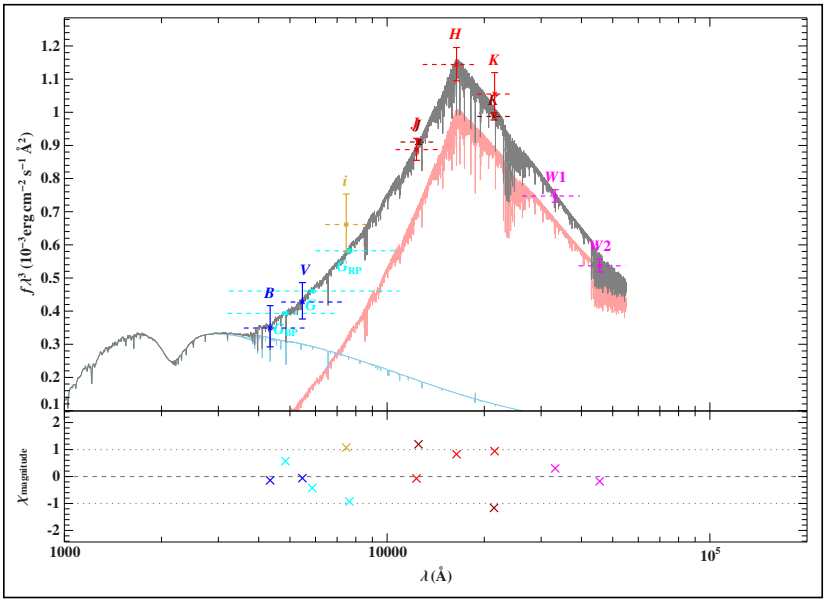

Figure 76: Gaia DR2 5792639748086292736; Top: Spectral Energy Distribution grey: combined, light-blue: subdwarf B, red: Cool companion. Bottom: Deviation of the photometric data from the actual SED in $[mag]$. The x-axis is the wavelength given in $[\AA]$.

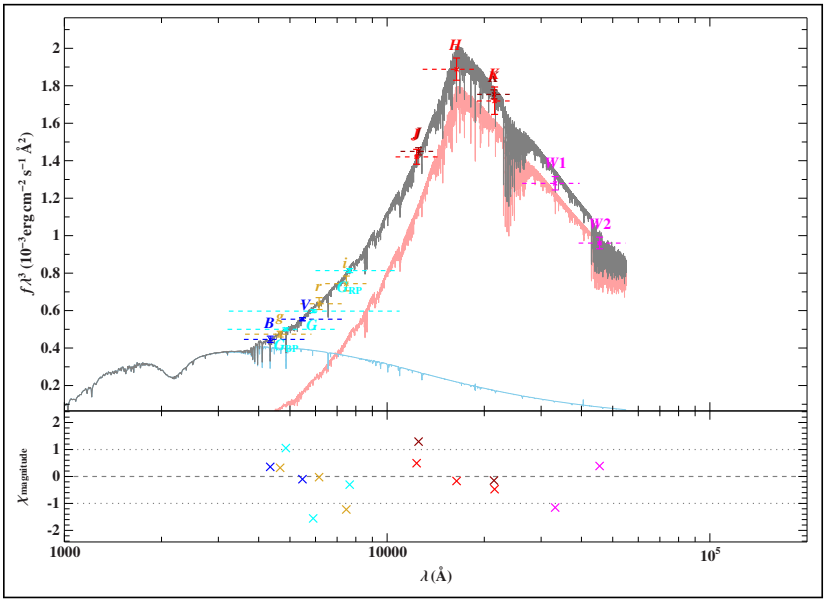

Figure 77: Gaia DR2 5906348045176103424; Top: Spectral Energy Distribution grey: combined, light-blue: subdwarf B, red: Cool companion. Bottom: Deviation of the photometric data from the actual SED in $[mag]$. The x-axis is the wavelength given in $[\AA]$.

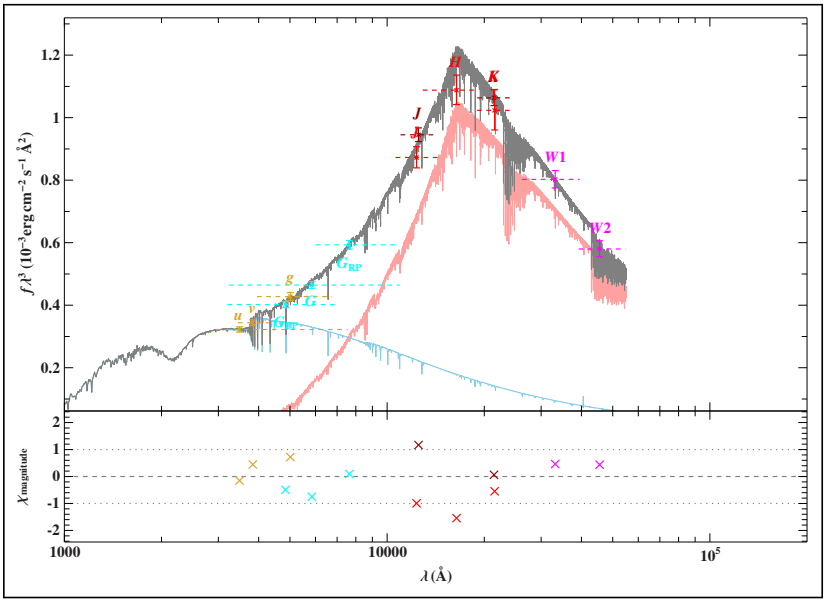

Figure 78: Gaia DR2 5946601372041301504; Top: Spectral Energy Distribution grey: combined, light-blue: subdwarf B, red: Cool companion. Bottom: Deviation of the photometric data from the actual SED in $[mag]$. The x-axis is the wavelength given in $[\AA]$.

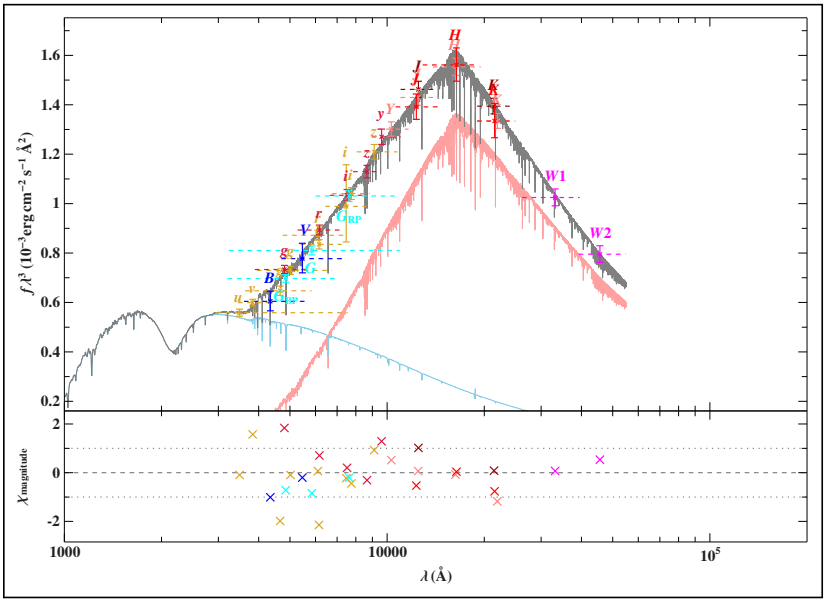

Figure 79: Gaia DR2 6040945070328432768; Top: Spectral Energy Distribution grey: combined, light-blue: subdwarf B, red: Cool companion. Bottom: Deviation of the photometric data from the actual SED in $[mag]$. The x-axis is the wavelength given in $[\AA]$.

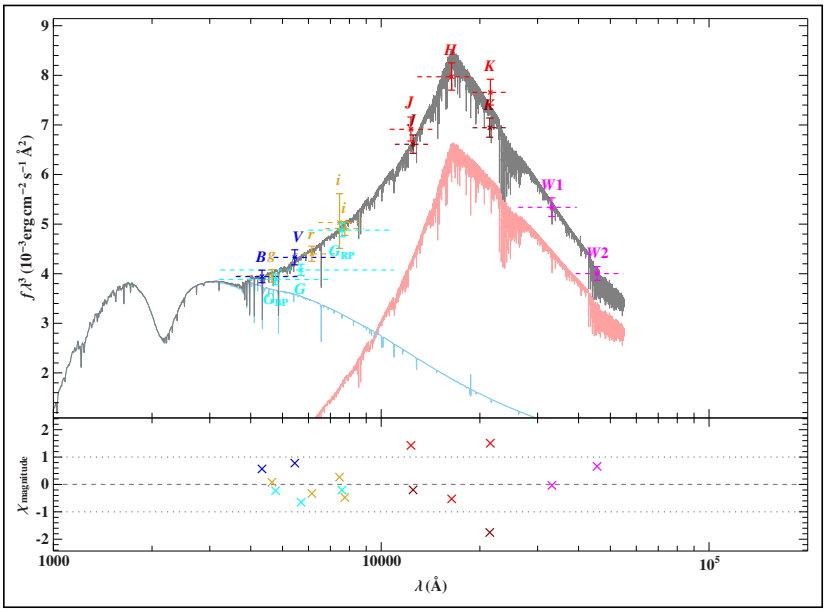

Figure 80: Gaia DR2 6100701942446586368; Top: Spectral Energy Distribution grey: combined, light-blue: subdwarf B, red: Cool companion. Bottom: Deviation of the photometric data from the actual SED in $[mag]$. The x-axis is the wavelength given in $[\AA]$.

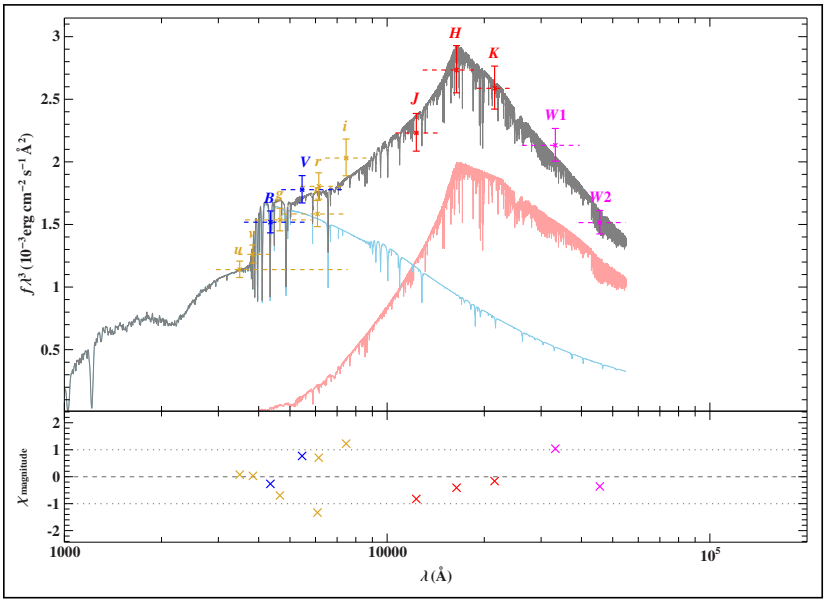

Figure 81: Gaia DR2 6635878236451584000; Top: Spectral Energy Distribution grey: combined, light-blue: subdwarf B, red: Cool companion. Bottom: Deviation of the photometric data from the actual SED in $[mag]$. The x-axis is the wavelength given in $[\AA]$.

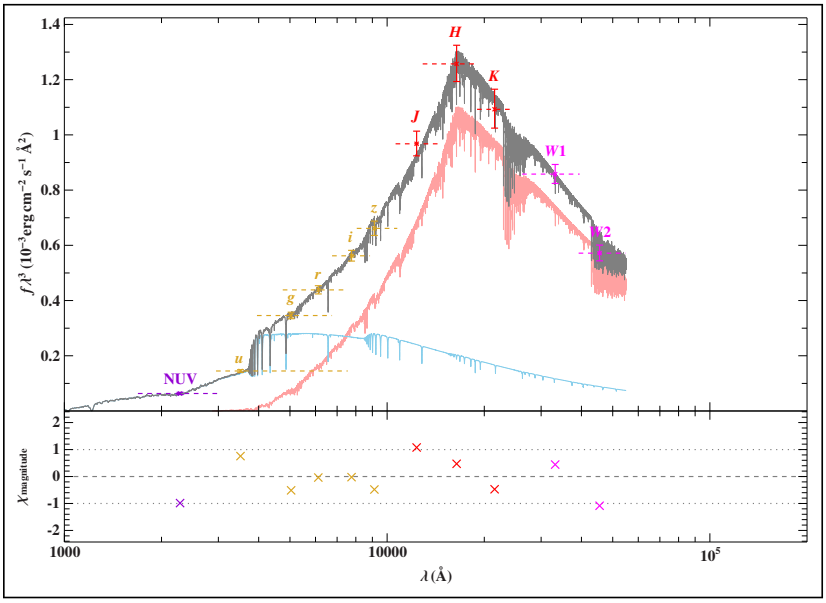

Figure 82: Gaia DR2 6691344062581573504; Top: Spectral Energy Distribution grey: combined, light-blue: subdwarf B, red: Cool companion. Bottom: Deviation of the photometric data from the actual SED in $[mag]$. The x-axis is the wavelength given in $[Å]$.

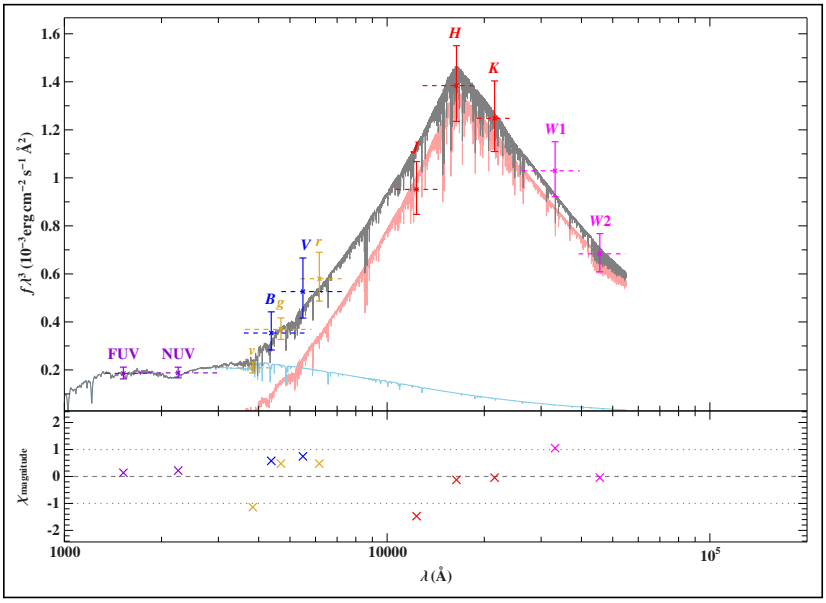

Figure 83: Gaia DR2 6731157309913205504; Top: Spectral Energy Distribution grey: combined, light-blue: subdwarf B, red: Cool companion. Bottom: Deviation of the photometric data from the actual SED in $[mag]$. The x-axis is the wavelength given in $[Å]$.

9 Bibliography

Alam S., et al., 2015, ApJS, 219, 12

Barlow B. N., Wade R. A., Liss S. E., Østensen R. H., Van Winckel H., 2012, ApJ, 758, 58

Barlow B. N., et al., 2013, MNRAS, 430, 22

Berger J., Fringant A. M., 1980, A&A, 85, 367

Bessell M. S., 2005, Annual Review of Astronomy and Astrophysics, 43, 293

Bethe H. A., 1939, Physical Review, 55, 103

Bianchi L., Shiao B., Thilker D., 2017, VizieR Online Data Catalog, p. II/335

Bingham R. G., Cousins A. W. J., 1974, Monthly Notes of the Astronomical Society of South Africa, 33, 15

Burbidge G. R., Hoyle F., Burbidge E. M., Christy R. F., Fowler W. A., 1956, Physical Review, 103, 1145

Carroll B. W., Ostlie D. A., 2007, An Introduction to Modern Astrophysics, pearson international edition, second edition edn. Addison Wesley, San Francisco, California

Chambers K. C., et al., 2016, arXiv e-prints, p. arXiv:1612.05560

Collaboration G., Brown A. G. A., Vallenari A., Prusti T., de Bruijne J. H. J., Babusiaux C., Bailer-Jones C. A. L., 2018, Astronomy & Astrophysics

Cousins A. W. J., 1978, Monthly Notes of the Astronomical Society of South Africa, 37, 8

Cutri R. M., et al. 2014, VizieR Online Data Catalog, p. II/328

Cutri R. M., et al., 2003, VizieR Online Data Catalog, p. II/246

Drilling J. S., Jeffery C. S., Heber U., Moehler S., Napiwotzki R., 2013, A&A, 551, A31

Ducati J. R., 2002, VizieR Online Data Catalog,

Edelmann H., Heber U., Hagen H. J., Lemke M., Dreizler S., Napiwotzki R., Engels D., 2003, A&A, 400, 939

Evans D. W., et al., 2018, A&A, 616, A4

Fitzpatrick E. L., 1998, Publications of the Astronomical Society of the Pacific

Fukugita M., Ichikawa T., Gunn J. E., Doi M., Shimasaku K., Schneider D. P., 1996, AJ, 111, 1748

Geier S., et al., 2011, A&A, 530, A28

Geier S., Østensen R. H., Nemeth P., Fusillo N. P. G., Gänsicke B. T., Telting J. H., Green E. M., Schaffenroth J., 2017, Astronomy & Astrophysics, 600, A50

Geier S., Raddi R., Fusillo N. P. G., Marsh T. R., 2019, Astronomy & Astrophysics, 621, A38

Girven J., et al., 2012, Monthly Notices of the Royal Astronomical Society, 425, 1013

Green G., 2019, 3D dust map from Green et al. (2019), doi:10.7910/DVN/2EJ9TX, `https://dataverse.harvard.edu/citation?persistentId=doi:10.7910/DVN/2EJ9TX`

Green R. F., Schmidt M., Liebert J., 1986, ApJS, 61, 305

Han Z., Podsiadlowski P., Maxted P. F. L., Marsh T. R., Ivanova N., 2002, MNRAS, 336, 449

Hauck B., Mermilliod M., 1997, VizieR Online Data Catalog, p. II/215

Hauschildt P. H., Baron E., 1999, Journal of Computational and Applied Mathematics, 109, 41

Heber U., 2009, ARA&A, 47, 211

Heber U., Irrgang A., Schaffenroth J., 2017, Spectral energy distributions and colours of hot subluminous stars (arXiv:1712.06546)

Henden A. A., Levine S., Terrell D., Welch D. L., 2015, in American Astronomical Society Meeting Abstracts #225. p. 336.16

Hog E., et al., 2000, VizieR Online Data Catalog, p. I/259

Johnson H. L., 1962, ApJ, 135, 69

Johnson H. L., Morgan W. W., 1953, ApJ, 117, 313

Keller S. C., et al., 2007, Publications of the Astronomical Society of Australia

Kepler S. O., et al., 2015, MNRAS, 446, 4078

Kepler S. O., et al., 2016, MNRAS, 455, 3413

Kilkenny D., O'Donoghue D., Koen C., Stobie R. S., Chen A., 1997, MNRAS, 287, 867

Kilkenny D., O'Donoghue D., Worters H. L., Koen C., Hambly N., MacGillivray H., 2015, MNRAS, 453, 1879

Kilkenny D., Worters H. L., O'Donoghue D., Koen C., Koen T., Hambly N., MacGillivray H., Stobie R. S., 2016, MNRAS, 459, 4343

Kurucz R. L., 1970, SAO Special Report, 309

Lamontagne R., Demers S., Wesemael F., Fontaine G., Irwin M. J., 2000, AJ, 119, 241

Landolt A. U., 2007, AJ, 133, 2502

Lawrence A., et al., 2007, Monthly Notices of the Royal Astronomical Society, 379, 1599

Lawrence A., et al., 2013, VizieR Online Data Catalog, p. II/319

Lisker T., Heber U., Napiwotzki R., Christlieb N., Han Z., Homeier D., Reimers D., 2005, A&A, 430, 223

Lucas P. W., et al., 2008, MNRAS, 391, 136

Luo Y.-P., Németh P., Liu C., Deng L.-C., Han Z.-W., 2016, ApJ, 818, 202

Luo Y., Németh P., Deng L., Han Z., 2019, ApJ, 881, 7

Martin C., GALEX Team 2005, in Colless M., Staveley-Smith L., Stathakis R. A., eds, IAU Symposium Vol. 216, Maps of the Cosmos. p. 221, doi:10.1017/S0074180900196664

Milone E. F., Sterken C., eds, 2011, Astronomical Photometry. Springer New York, doi:10.1007/978-1-4419-8050-2, https://doi.org/10.1007/978-1-4419-8050-2

Morel M., Magnenat P., 1978, A&AS, 34, 477

Németh P., Kawka A., Vennes S., 2012, MNRAS, 427, 2180

Norris J. E., Ryan S. G., Beers T. C., 1999, ApJS, 123, 639

O'Donoghue D., Kilkenny D., Koen C., Hambly N., MacGillivray H., Stobie R. S., 2013, MNRAS, 431, 240

Østensen R. H., 2006, Baltic Astronomy, 15, 85

Paunzen E., 2015, VizieR Online Data Catalog, pp J/A+A/580/A23

Rufener F., 1999, VizieR Online Data Catalog, p. II/169/

Schlafly E. F., Finkbeiner D. P., 2011, ApJ, 737, 103

Schlegel D. J., Finkbeiner D. P., Davis M., 1998, ApJ, 500, 525

Shanks T., et al., 2015, MNRAS, 451, 4238

Skrutskie M. F., et al., 2006, AJ, 131, 1163

Soker N., Catelan M., Rood R. T., Harpaz A., 2002, The Astrophysical Journal, 563, L69

Stroeer A., Heber U., Lisker T., Napiwotzki R., Dreizler S., Christlieb N., Reimers D., 2007, A&A, 462, 269

Strömgren B., 1956, Vistas in Astronomy, 2, 1336

Szymański M., Udalski A., Kubiak M., Pietrzyński G., Soszyński I., Woźniak P., Zebruń K., 2000, in Schielicke R. E., ed., Astronomische Gesellschaft Meeting Abstracts.

Thejll P., Ulla A., MacDonald J., 1995, A&A, 303, 773

Vennes S., Kawka A., Németh P., 2011, MNRAS, 410, 2095

Wegner G., Dupuis J., 1993, AJ, 106, 390

Wright E. L., et al., 2010, The Astronomical Journal, 140, 1868

de Jong J. T. A., et al., 2017, A&A, 604, A134

van Leeuwen F., 2007, A&A, 474, 653

Erklärung

Hiermit versichere ich, dass ich die vorliegende Arbeit selbstständig verfasst und keine anderen als die angegebenen Quellen und Hilfsmittel benutzt habe.

Erlangen, den 31.03.2020 (Jan Friedmann)